JGR Planets

RESEARCH ARTICLE
10.1029/2018JE005841

Special Section:
Science and Exploration of the Moon, Near-Earth Asteroids, and the Moons of Mars

Geological Characterization of the Ina Shield Volcano Summit Pit Crater on the Moon: Evidence for Extrusion of Waning-Stage Lava Lake Magmatic Foams and Anomalously Young Crater Retention Ages

Le Qiao[1,2], James W. Head[2], Zongcheng Ling[1], Lionel Wilson[3], Long Xiao[4], Josef D. Dufek[5], and Jianguo Yan[6]

[1]Shandong Provincial Key Laboratory of Optical Astronomy and Solar-Terrestrial Environment, Institute of Space Sciences, Shandong University, Weihai, China, [2]Department of Earth, Environmental and Planetary Sciences, Brown University, Providence, RI, USA, [3]Lancaster Environment Centre, Lancaster University, Lancaster, UK, [4]Planetary Science Institute, School of Earth Sciences, China University of Geosciences, Wuhan, China, [5]School of Earth and Atmospheric Sciences, Georgia Institute of Technology, Atlanta, GA, USA, [6]State Key Laboratory of Information Engineering in Surveying, Mapping and Remote Sensing, Wuhan University, Wuhan, China

Key Points:
- Ina feature occurs as a summit pit crater/vent atop a broad ~22-km-diameter, ~3.5-Ga-old shield volcano
- The range of geologic characteristics of Ina is most consistent with an ancient origin of *waning-stage lava lake magmatic foam extrusion*
- Highly vesicular nature of the magmatic foam mounds and lava lake crust floor substrate results in anomalously young crater retention ages

Supporting Information:
- Supporting Information S1

Correspondence to:
L. Qiao and Z. Ling,
leqiao.geo@gmail.com;
zcling@sdu.edu.cn

Citation:
Qiao, L., Head, J. W., Ling, Z., Wilson, L., Xiao, L., Dufek, J. D., & Yan, J. (2019). Geological characterization of the Ina shield volcano summit pit crater on the Moon: Evidence for extrusion of waning-stage lava lake magmatic foams and anomalously young crater retention ages. *Journal of Geophysical Research: Planets*, *124*, 1100–1140. https://doi.org/10.1029/2018JE005841

Received 4 MAR 2018
Accepted 25 MAR 2019
Accepted article online 29 MAR 2019
Published online 29 APR 2019

Abstract Ina, a distinctive ~2 × 3 km D-shaped depression, is composed of unusual bulbous-shaped mounds surrounded by optically immature hummocky/blocky floor units. The crisp appearance, optical immaturity, and low number of superposed impact craters combine to strongly suggest a geologically recent formation for Ina, but the specific formation mechanism remains controversial. We reconfirm that Ina is a summit pit crater/vent on a small shield volcano ~3.5 billion years old. Following detailed characterization, we interpret the range of Ina characteristics to be consistent with a two-component model of origin during the waning stages of summit pit eruption activities. The Ina pit crater floor is interpreted to be dominated by the products of late-stage, low-rise rate magmatic dike emplacement. Magma in the dike underwent significant shallow degassing and vesicle formation, followed by continued degassing below the solidified and highly microvesicular and macrovesicular lava lake crust, resulting in cracking of the crust and extrusion of gas-rich magmatic foams onto the lava lake crust to form the mounds. These unique substrate characteristics (highly porous aerogel-like foam mounds and floor terrains with large vesicles and void space) exert important effects on subsequent impact crater characteristics and populations, influencing (1) optical maturation processes, (2) regolith development, and (3) landscape evolution by modifying the nature and evolution of superposed impact craters and thus producing anomalously young crater retention ages. Accounting for these effects results in a shift of crater size-frequency distribution model ages from <100 million years to ~3.5 billion years, contemporaneous with the underlying ancient shield volcano.

Plain Language Summary Among the most outstanding questions in lunar evolution is the end of extrusive volcanic activity, commonly thought to be at least a billion years old. A recent study found evidence for volcanic activity within the last 100 million years, in the form of *irregular mare patches* dated by size-frequency distributions of superposed craters. The most prominent irregular mare patch is Ina, an ~2 × 3-km depression composed of bulbous-shaped mounds surrounded by fresh, hummocky and blocky floor units, both supporting the geologically very recent age. We undertook a detailed characterization of the setting of Ina and its interior and found that its location on the summit of a 3.5 billion years old small shield volcano, together with Hawaiian field analogs and theoretical analyses of the ascent and eruption of magma, provided new clues to its origin and age. Late-stage magma extrusion in the summit pit characterized by gas-rich Strombolian activity produced a very vesicular crust and concentration of underlying magmatic foams; cracking of the crust caused magmatic foam extrusions to produce the mounds. The very porous nature of Ina deposits decreases the superposed crater diameters and shifts the crater size-frequency distribution to ~3.5 billion years, coincident with the ancient age of the volcano.

©2019. American Geophysical Union.
All Rights Reserved.

1. Introduction

Ina is an unusual lunar feature in Lacus Felicitatis on the central nearside of the Moon (18.65°N, 5.30°E), first discovered in Apollo 15 orbital photographs (El-Baz, 1973; Whitaker, 1972). Located in the midst of mare deposits interpreted to be ancient basalts, the ~2 × 3-km letter D-shaped shallow depression consists of unusually bright and blocky floor materials and dozens of bleb-like mounds with cross sections resembling liquid droplets with a high surface tension and a convex meniscus (El-Baz, 1973; Strain & El-Baz, 1980). Lunar Reconnaissance Orbiter (LRO) high-resolution image and topography data have permitted the characterization of the units within and associated with this feature (Garry et al., 2012), and the identification of dozens of small mare features resembling Ina on the central nearside of the Moon (Braden et al., 2014; Stooke, 2012) described as irregular mare patches (IMPs). Other major lunar IMPs (e.g., Sosigenes, Maskelyne, and Cauchy 5) also have interior structures similar to those of Ina, that is, being composed of bulbous-shaped mounds with surrounding lower hummocky and blocky terrains, while some relatively smaller IMPs may only develop topographically lower floor terrains (Braden et al., 2014). On high-resolution optical images, the floor terrains show much more complicated surface textures than the adjacent higher mounds. The optical maturity of the mounds lies between that of the mature surrounding ancient mare and the optically least mature floor units (Bennett et al., 2015).

Notable for their morphological crispness, apparent optical immaturity and unusually low superposed impact crater density, Ina and other IMPs are commonly interpreted to be related to geologically very recent processes. Earlier morphological analyses had found the Ina mounds to be some of the youngest lava extrusions on the Moon (Strain & El-Baz, 1980). Crater population studies yielded <100 Ma (million years) or even younger model ages for Ina and several other IMPs, specifically for Ina, ~33 Ma (Braden et al., 2014) or even <10 Ma for the Ina interior (Schultz et al., 2006). Diffusional landscape evolution models reported 5–40 Ma maximum ages for some marginal scarps within Ina and suggested that some small topographic troughs probably developed within the last 1–2 Ma or are still forming currently (Fassett & Thomson, 2014, 2015).

The wide range of geological peculiarities of the Ina feature, particularly the anomalously young crater retention ages, has led to various interpretations in terms of its formation mechanism (see summaries of parts of previous investigations in Elder et al., 2017 and Qiao et al., 2018). Preliminary characterization of Ina attributed the high reflectance of the floor materials to deposition of sublimates (Whitaker, 1972). Earlier photogeologic analyses based on Apollo orbital photographs interpreted the Ina floor as a collapse summit caldera atop an extrusive volcanic dome and the mounds as subsequent small lava extrusions (El-Baz, 1972, 1973; Strain & El-Baz, 1980). Schultz et al. (2006) examined the topographic relief, superposed impact crater populations and optical maturity of Ina, and suggested that Ina floor units originated from the removal of fine-grained surface materials by episodic outgassing within the past 10 Ma, and that they are perhaps still active today. Garry et al. (2012) called on terrestrial analogs (specifically, the McCarty's inflated lava flow field in New Mexico) and found that the Ina interior terrains have comparable dimensions and topographic relief to some terrestrial inflated lava flows and interpreted Ina as being formed through inflated lava flows (the mounds) followed by lava breakouts from the mound margins that built the hummocky units.

Braden et al. (2014) employed high-resolution LRO narrow angle cameras (LROC NAC) images to demonstrate many similarities between the morphology, topography, and spectroscopy of Ina and dozens of small topographic anomalies (termed *IMPs*) on the central nearside mare; they interpreted the floor units as disrupted lava pond crust caused by the collapse or drainage of the eruptive vent, and the mounds as small magma extrusions. Braden et al. (2014) also dated the mounds to be <100 Ma old, based on impact crater size-frequency distributions (SFDs), crater equilibrium populations, and topographic slope analyses. The <100-Ma-old estimate is significantly younger than the previous estimated age of the cessation of lunar mare volcanism ~1 billion years ago (Hiesinger et al., 2011; Morota et al., 2011; Schultz & Spudis, 1983). If true, this new age would require a major reevaluation of the conventional theory of lunar heat sources and lunar thermal evolution models. Carter et al. (2013) examined the radar scattering from Ina and two other IMPs and found that lunar IMPs exhibited a range of radar backscatter properties. The edges of the Ina depression and the interior blocky units are characterized by enhanced circular polarization ratio values, while the Ina mounds have circular polarization ratio values similar to those of the surrounding

mare deposits, indicating relatively homogeneous near-surface physical properties. Another lunar IMP feature studied (i.e., Cauchy 5) exhibits radar signals consistent with fine-grained, block-free materials, suggesting a potential origin of being mantled by pyroclastic deposits or other very fine grained deposits (Carter et al., 2013).

Bennett et al. (2015) used Moon Mineralogy Mapper (M^3) spectroscopic data to analyze the mineralogy and optical maturity of Ina and found that the multiple terrains within Ina and surrounding mare all exhibited similar, high-Ca pyroxene-dominated mineralogy, while optical maturity varied: the maturity of the mounds lies between those of the surrounding mature background mare and the least mature floor materials. Bennett et al. (2015) interpreted the multiple interior morphologic units of Ina to be emplaced contemporaneously with the surrounding ancient mare basalts and interpreted the apparent optical immaturity of the floor units as being due to their elevated blockiness; however, neither the precise formation mechanism nor other observed characteristics, particularly the apparently low number of superposed impact craters, were explained by Bennett et al. (2015). Elder et al. (2016, 2017) analyzed the thermophysical measurements collected by the LRO Diviner thermal radiometer and found that (1) the Ina interior is only slightly rockier than the surrounding mature mare regolith, while much less rocky than the ejecta of some ~100-Ma-old craters; (2) the surface regolith of the Ina interior is interpreted to be thicker than 10–15 cm; and (3) the Ina interior has slightly lower thermal inertia than the surrounding mare, indicating that the Ina materials are less consolidated or contain fewer small rock fragments than typical regolith. These surface physical properties suggest either that Ina is older than its calculated crater retention ages or that Ina is indeed <100 Ma old, but its surface accumulates regolith more rapidly than blocky ejecta deposits. Elder et al. (2017) proposed that some form of explosive activity, either pyroclast deposition (Carter et al., 2013) or another style of outgassing (Schultz et al., 2006) was likely to have been involved in the formation of Ina, though the possibility of lava flow inflation (Garry et al., 2012) or regolith drainage into subsurface void space (Qiao et al., 2016) could not be precluded; however, the specific formation mechanism and emplacement sequences of the various morphologic units within Ina were not detailed by Elder et al. (2017).

Neish et al. (2017) compared the surface physical properties of Ina mounds and lunar impact melt flows at Korolev X via LROC NAC digital terrain model (DTM) topography and Mini-RF S-Band radar images and found that Ina mounds have similar physical properties (e.g., Hurst exponent and root mean square slope) to lunar impact melt flows at the meter scale (both appear *smooth*). However, Ina mounds appear much *smoother* than lunar impact melt flows at decimeter scale. Integrating analyses with other physical property investigations (Neish et al., 2014) of lunar Copernican impact melts (Ravi et al., 2016) indicate either that Ina mounds are not formed by Copernican lava flow emplacement or that young lava flows have different physical properties from those of similarly aged impact melt flows on the Moon. Valantinas et al. (2018) presented new impact crater SFD measurements of the Sosigenes and Nibum IMPs and obtained model ages of 22 ± 1 and 46 ± 5 Ma, respectively. They also observed production-like cumulative log-log SFD slopes of -3 for these superposed craters, suggesting these crater populations are probably still in production. Valantinas et al. (2018) concluded that the Nubium and Sosigenes IMPs might have been affected by a unique endogenic process, though the specific modification mechanism is not detailed.

Recent theoretical treatments of final-stage shield-building magmatic activity and volatile exsolution physics (Head & Wilson, 2017; Wilson & Head, 2017a) provided a framework to interpret Ina as a drained summit pit crater lava lake atop an ancient shield volcano ~3.5 billion years (Ga) old, contemporaneous with the major phase of lunar mare volcanism (Qiao et al., 2017; Wilson & Head, 2017b). In this hypothesis, the floor hummocky and blocky units are the solidified lava lake crust, which is several meters thick and very vesicular, both at the microvesicular and macroporosity scales due to the presence of large void spaces generated by crust deformation, bubble coalescence, and disruption during the very late stage volatile-release-driven Strombolian eruptions. The lava lake crust is underlain by the hypothesized magmatic foams accumulated in the top tens to hundreds of meters of the dike and in the lake interior, produced through the exsolution of H_2O and the gradual decrease of magma ascent rates. The mounds are interpreted as solidified magmatic foams extruded through fractures in the chilled lava lake crust, characterized by abundant small vesicles, with an extremely high vesicularity, up to ~95%. The unique physical properties of the floor units (abundant small vesicles and large void space) and the mounds (magmatic foams) significantly change the behavior of the subsequent impact cratering and regolith development processes, topographic degradation, and surface weathering, maintaining the observed apparent optical immaturity and crisp

appearance, and resulting in an anomalously young crater retention age for the Ina interior units (Qiao et al., 2017).

In the present contribution, building on these previous analyses and hypotheses of origin for the Ina feature above (Braden et al., 2014; Garry et al., 2012; Qiao et al., 2017; Schultz et al., 2006; Strain & El-Baz, 1980; Wilson & Head, 2017b), we undertake a detailed and comprehensive analysis of the data available for Ina (see detailed analysis data and methods in Text S1 in the supporting information) and characterize (1) the regional geologic context; (2) the quantitative topography, morphology, and morphometry of the Ina interior terrains (including the mounds, ledge, scarps, floor hummocky and blocky units, pit formations, depressions, and topographic moats); (3) impact craters (including identification, morphology, size-frequency distributions and the discrepancy between different interior units and the surrounding ancient mare); (4) regolith thickness and its variations among different regions; and (5) optical reflectivity and maturity. We focus on the following specific questions to assess the multiple theories of origin: (1) what is the nature of the specific morphological units in Ina and the nature, distribution, and relationships of the *mound* and the *hummocky floor* materials? (2) what is the nature of the detailed topography within Ina and how does it relate to the distribution of the mound and the hummocky floor material? (3) the Ina structure shows an anomalously immature interior, thus supporting a young age: what is the detailed nature and distribution of the immaturity within Ina, how does it relate to the detailed geologic units, and how does this inform the discussion of Ina origin? (4) the Ina structure shows a paucity of superposed impact craters, thus supporting a young age: what is the detailed nature and distribution of the existing impact craters within Ina and how does this inform the discussion of the origin of Ina? (5) if Ina represents a shield volcano summit pit crater, how does its geology and morphology support or challenge models of (a) geologically recent or (b) final-stage summit pit crater evolution during a phase of ancient shield-building volcanism? (6) what are the detailed pros and cons for volcanism occurring in the last 100 Ma? (7) what are the outstanding questions that can be addressed to resolve the origin of Ina (and other IMPs)? Then, on the basis of terrestrial analog observations of terrestrial small shield volcanoes in Hawai'i, and lunar mare basalt ascent and eruption theory and observations (Head & Wilson, 2017; Wilson & Head, 2017a), we address alternative formation mechanisms of the ranges of characteristics associated with Ina and their postemplacement geologic modification, especially the observed anomalously young crater retention ages. We also discuss the implications for the origin of other lunar IMPs, the duration of mare volcanism, and the potential of Ina as a target for future surface exploration missions.

2. Regional Setting of the Ina Pit Crater

2.1. Regional Morphology and Topography

The enigmatic Ina feature occurs in the middle of Lacus Felicitatis, a relatively small mare basaltic plain (diameter ~90 km, area ~2.24 × 10^3 km^2) among three extensive maria: Mare Vaporum in the south, Mare Imbrium in the northwest, and Mare Serenitatis in the northeast (Figure 1a). Lacus Felicitatis is surrounded by voluminous ejecta deposits from the Imbrium and Serenitatis basins, and the Ina feature is only ~3 km from the adjacent basin ejecta (Figure 1a). These ejecta deposits are overprinted by distinctive linear ridged and grooved patterns, dominantly in a northwest-southeast trend and radial to the Imbrium basin center (Strain & El-Baz, 1980, Figure 1a). The formation of these lineaments is generally thought to be related to the catastrophic Imbrium impact event ~3.85 Ga ago (e.g., Stöffler & Ryder, 2001) or subsequent ejecta sedimentation process, while the specific origin is largely unknown (e.g., Head, 1976; Spudis, 1993). Northeast-southwest trending lineaments radial to the Serenitatis basin have also been observed, which have been heavily covered and degraded by subsequent Imbrium ejecta (Strain & El-Baz, 1980, Figure 1a).

The basalts of Lacus Felicitatis, along with several other small patches of mare, for example, Lacus Odii and Lacus Doloris (Figure 1a), are superposed on these highland materials ejected from the two giant basins. The Lacus Felicitatis mare deposits are ~100–220 km from the southeastern main rim of the Imbrium basin, and ~80–150 km from the intermediate ring of the Serenitatis basin (Figure 1a). The Imbrium ejecta deposits feature a continuous and rapid elevation decrease from the Imbrium main rim (Montes Apenninus) to the Lacus Felicitatis mare region, with a total topographic relief of ~2.5 km across a distance of 150 km (Figures 1b and 1c). From the intermediate rim (Montes Haemus) of the Serenitatis

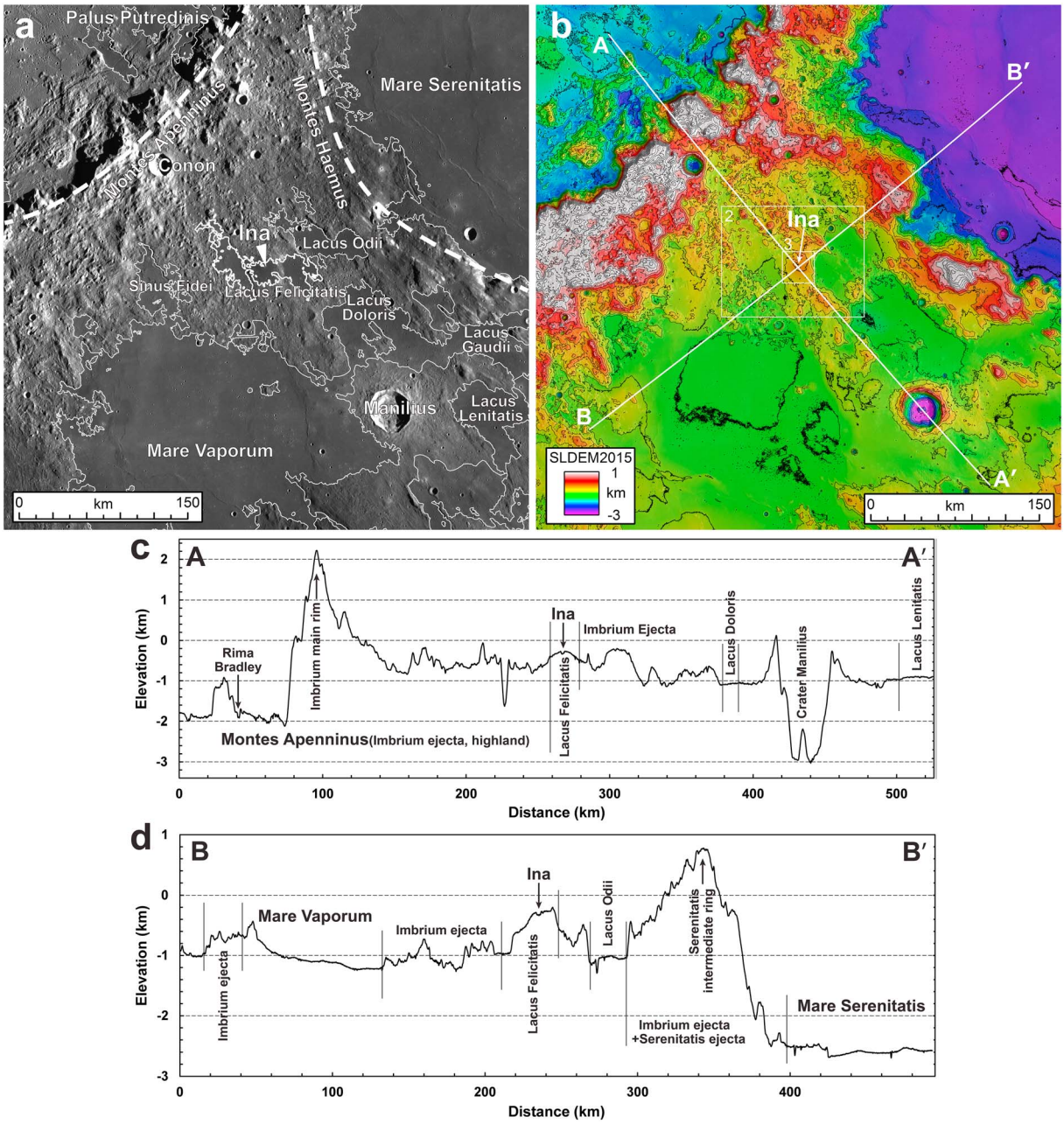


Figure 1. (a) Major physiographic features within the regional context of Ina. The Ina feature is marked by the white arrow (center); the approximate locations of parts of the Imbrium basin main ring (D = 1,160 km; Pike & Spudis, 1987) and Serenitatis basin intermediate ring (D = 613 km; Head, 1979) are marked by the bold dashed white curves; the multiple mare regions are labeled by their nomenclature, with their boundaries marked by the thin solid white outlines. The extent of Lacus Felicitatis, in which Ina occurs, is highlighted by a thicker white outline. The background image is a portion of the LROC-WAC nearside low-Sun mosaic, pixel size is 100 m. (b) Topographic map of the regional context of the Ina feature. Ina is indicated by the white arrow. The white lines mark the locations of the two topographic profiles shown in Figures 1c and 1d, and the white boxes mark the locations of Figures 2 and 3. Contour interval is 300 m. Topography data are derived from the SELENE-TC+LRO-LOLA merged DEM (SLDEM2015, Barker et al., 2016). (c) NW-SE and (d) SW-NE topographic profile derived from SLDEM2015 topography, showing the major topographic features (labeled by their nomenclature) of the regional context of the Ina feature, in a direction radial to the center of the Imbrium basin and Serenitatis basin, respectively. See Figure 1b for its location. All the maps for the Ina region in this paper are projected into a sinusoidal projection with a central meridian of 5.3473°E, and north is up.

basin to Lacus Felicitatis, the regional surface elevation decreases by ~1.4 km across a distance of ~90 km (Figures 1b and 1d).

The mare basalts within Lacus Felicitatis show evidence of multiple phases of lava infilling activity and complex geological modification processes. The surface elevations of the Lacus Felicitatis mare deposits are

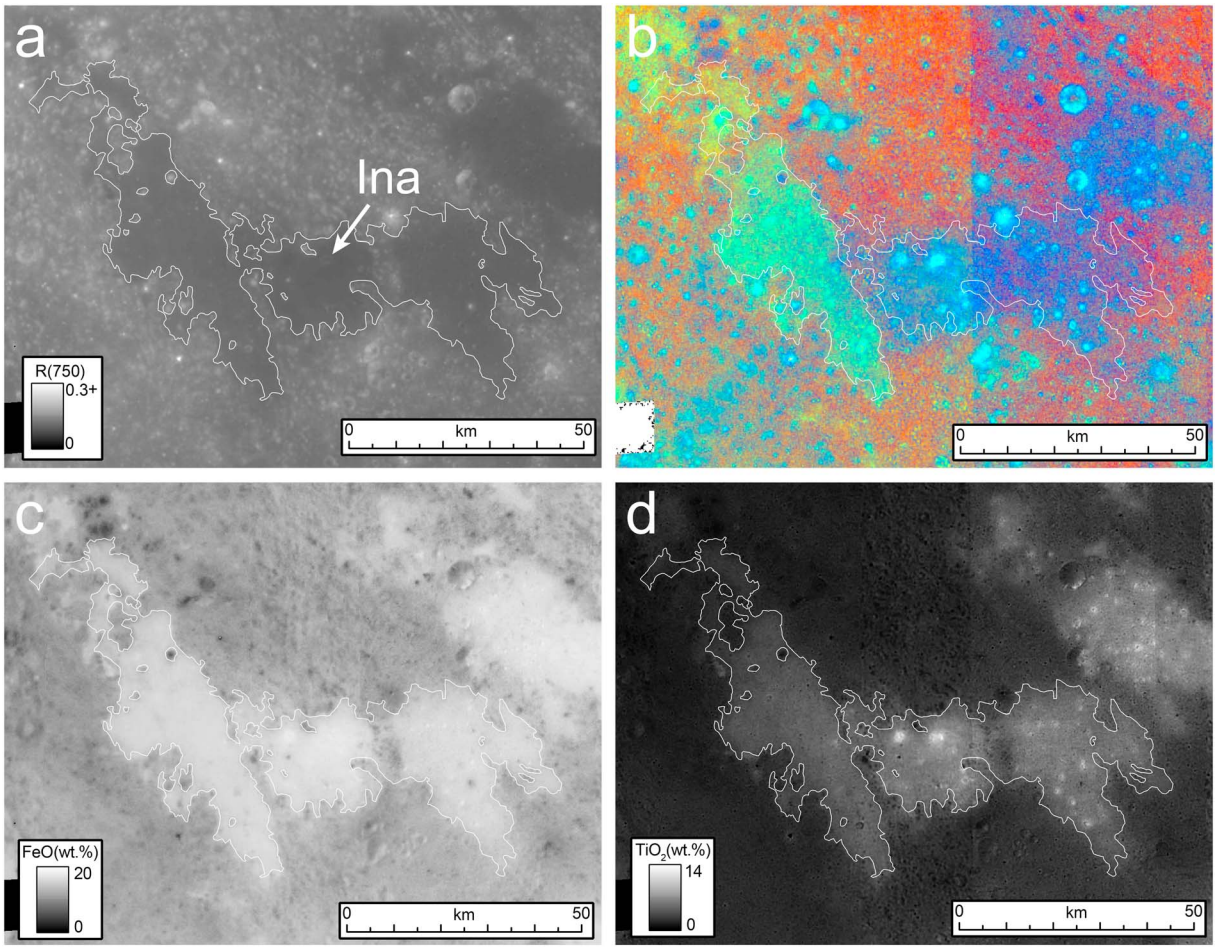


Figure 2. Clementine UVVIS maps of Lacus Felicitatis: (a) 750 nm reflectance, (b) color ratio composite (red channel = 750/415 nm, green channel = 750/950 nm, and blue channel = 415/750 nm), (c) FeO, and (d) TiO_2 abundance calculated from the Lucey, Blewett, and Jolliff (2000) algorithm. The boundary of Lacus Felicitatis is shown by the white outline, and Ina is marked by the white arrow in Figure 2a.

generally higher than those of the adjacent mare deposits, for example, Lacus Odii, Lacus Doloris, and Mare Vaporum (Figure 1b). Compared with the neighboring Lacus Odii, the Lacus Felicitatis deposits are characterized by at least ~80-m higher elevation. The basalts of Lacus Felicitatis have a relatively uniform iron abundance (Figure 2c, FeO = 15.8 ± 1.2 wt %) but show a titanium enrichment toward the east (Figures 2b and 2d, calculated from Clementine ultraviolet/visible (UVVIS) data using the Lucey, Blewett, & Jolliff, 2000 algorithm). The central Lacus Felicitatis is characterized by a raised plateau, which is ~800 m higher than the eastern Lacus Felicitatis basalts, and ~650 m higher than the western Lacus Felicitatis basalts (Figures 1b, 3b, and 3d). This plateau dips toward the west: the west margin scarp has a steeper kilometer-scale slope (~9°, 305 m/1,900 m) than the eastern scarp (~6°, 740 m/6,600 m). The west scarp extends both north and south, into the highlands, in a direction radial to the Imbrium rim and appears to merge with wrinkle ridges crossing eastern Mare Vaporum (Figure 1a). The central Lacus Felicitatis basalts have an intermediate titanium abundance (TiO_2 = 4.4 ± 1.0 wt %), and, in particular, the materials in the Ina interior and a nearby fresh crater show apparently elevated titanium contents, suggesting the exposure of underlying high-titanium mare basalts (see section 3.14 for more details).

2.2. The Ina Shield Volcano

New high-resolution altimetry and image data from the LRO and Kaguya spacecraft clearly show that Ina is not only located within the Lacus Felicitatis mare deposits but also occurs as an ~2 × 3-km depression atop a shield volcano (Figure 3), consistent with the previous interpretation of Strain and El-Baz (1980).

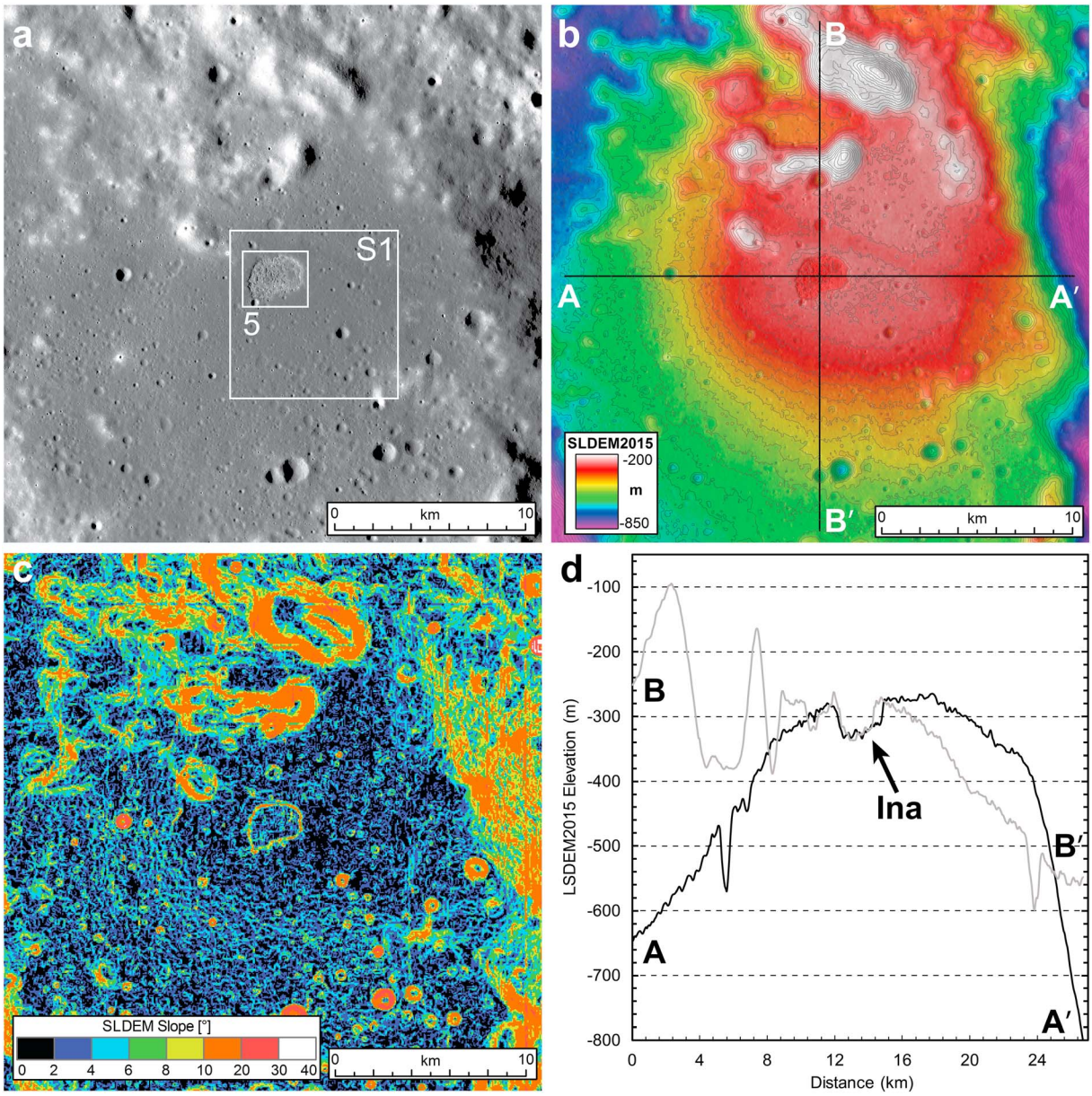


Figure 3. Image and topography of the small shield volcano on which the Ina feature sits. (a) Portion of Kaguya TC evening image mosaic TCO_MAPe04_N21E003N18E006SC, 10 m/pixel. White boxes mark the locations of Figures 5 (also Figures 6, 13 upper panel, 16a, S2, S10, S11, S14, S15, and S19) and S1. (b) SLDEM2015 topography overlain on Kaguya TC evening mosaic. The black lines mark the locations of the two elevation profiles shown in Figure 3d. (c) SLDEM2015-derived topographic slope map, with a baseline of ~180 m. (d) West-east (A-A′) and north-south (B-B′) topographic profiles across the small shield, with Ina location marked by the black arrow.

This shield is ~22-km wide at its base and ~320-m high (Qiao et al., 2017), and at the upper end of the base diameter and height range for over 300 mare domes that are interpreted as small shield volcanoes (Head & Gifford, 1980; Tye & Head, 2013, Figure 4a). The diameter of the Ina pit crater also lies on the summit crater diameter/base diameter trend line of lunar small shields (Figure 4b). Lunar small shield volcanoes are generally interpreted to develop when dikes propagate to the surface and shields build up through multiple phases of flows erupted from a common pit crater source, dominated by accumulating low-effusion rate, cooling-limited flows (Head & Wilson, 1992, 2017). The Ina shield volcano is well developed in the southern portion, while the growth of the northern part is affected by the preexisting ejecta deposits. The topographic slope of this shield is typical ~2–6° (Figure 3c). A linear rille is observed crossing the Ina shield volcano, extending west-northwest to the proximal highlands and east-

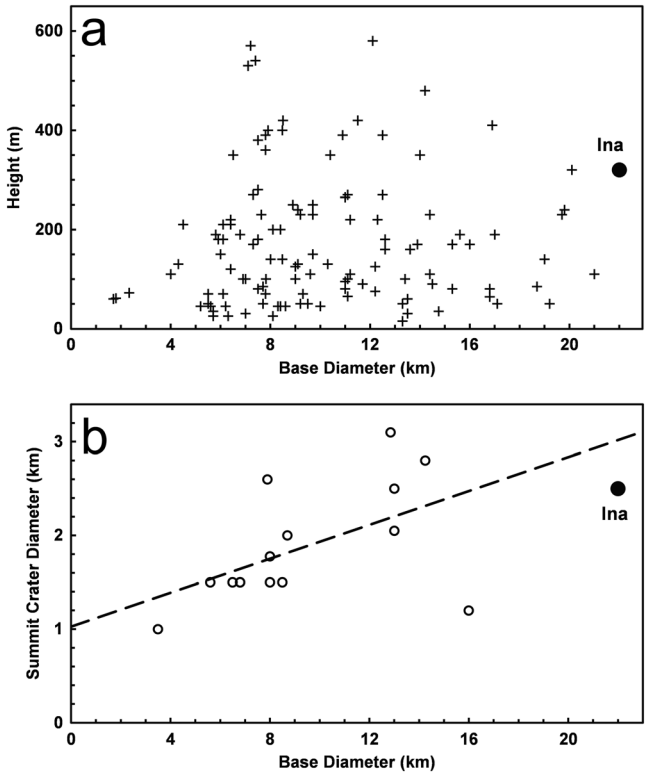


Figure 4. (a) Base diameter-height plot for lunar small shield volcanoes catalog by Consolidated Lunar Dome Catalogue (crosses; http://digilander.libero.it/glrgroup/cldc.htm) and the Ina shield (black dot) and (b) base diameter-summit pit crater diameter plot for small lunar shield volcanoes catalog in Head and Gifford (1980, circles) and Ina shield (black dot).

southeast to the lower eastern Lacus Felicitatis mare deposits (Figure 3). The trend of this rille is nonradial to the Imbrium center, distinguishing it from a set of low-relief radial lineations in the surrounding ejecta deposits; the latter lineations are generally interpreted to originate from the giant Imbrium impact (e.g., Head, 1976; Schultz & Crawford, 2016). Cross-cutting relationships indicate that this linear rille developed after the building of the Ina shield.

We dated the Ina shield volcano using impact crater SFD measurements and LROC NAC images on the south flank and obtained an absolute model age of 3.5 (+0.06/−0.1) Ga (Qiao et al., 2017; Figure S1), which is consistent with previous >3.5-Ga estimation by Schultz et al. (2006) and shows unequivocally that this shield is ancient and contemporaneous with the major phase of lunar mare volcanism (Hiesinger et al., 2011; Papike et al., 1976). Any interpretation that calls on Ina floor features to be formed geologically very recently (e.g., <100 Ma) must also explain why these features are located in an ancient volcano summit pit crater.

3. Interior of Ina

High-resolution LROC NAC image (up to ~0.48-m pixel size) and altimetry (2 m/pixel) data have permitted the detailed characterization of the interior units of Ina pit crater (Braden et al., 2014; Garry et al., 2012; Qiao et al., 2017). Here we utilize previous studies, new data, and mapping to report some updated and more comprehensive observations of the quantitative topography, morphology, morphometry, crater population, regolith thickness, and optical properties of Ina interior terrains. These quantitative characterizations will provide important information for constraining the emplacement process of each interior units, and the comparison with those of other IMPs will contribute fundamental observation to future investigations of IMP characteristics and origin.

3.1. General Characterization

The Ina crater interior is delimited by an inward facing wall (typical up to ~100-m wide, ~10-m high, and 5–10° slope) and a relatively flat basal terrace/ledge (typical ~50-m wide, up to ~5-m high, and <5° slope) with a steep (10–30° slope) inward facing scarp up to ~12-m high (Figures 5–8). The entire interior is broadly letter D shaped (El-Baz, 1973, Figure 5), with a dimension of ~2.9 × 2.1 km and a surface area of 4.55 km^2. Bounding the rim is a raised topographic *collar*, about 0.5- to 1-km wide and up to ~30-m high relative to the surrounding mare shield (Figure 3 in Garry et al., 2012). The interior floor is generally flat, slopes gently (<2°) toward the center (Figure 6), and mainly lies about 20–50 m below the rim (Figures 6 and 7). The interior of Ina pit crater is dominated by three morphological units typical for other major lunar IMPs (Figure 5b): (1) the unusual meniscus-like mounds, rising up to ~20 m above the proximal floor units (Figure 7), occupying ~50% of the total interior area, (2) topographically lower hummocky units (~44% by area) with ridged and pitted textures, and (3) topographically lower blocky materials consisting of 1- to 5-m size boulders (Braden et al., 2014; Garry et al., 2012; Qiao et al., 2017; Qiao, Head, Xiao, Wilson, & Dufek, 2018; Schultz et al., 2006; Strain & El-Baz, 1980). The mounds are generally convex upward (Figures 6 and 7), very flat at the tops, and reach steep slopes (~10–30°) at the edges (Figure 6c). Among the multiple terrains within the Ina interior, only the major mound at the eastern margin has an International Astronomical Union confirmed name, termed *Mons Agnes* (Figure 5a). In the following subsections, we will characterize each morphologic terrain with specific details.

3.2. Mounds

A key question in determining the origin of the range of features in Ina is their morphology, morphometry, and relationship to one another. We identify 88 mounds within the Ina interior (Figures 5b and S2 with mounds numbered), compared with more than 50 mounds reported by Garry et al. (2012). The mounds

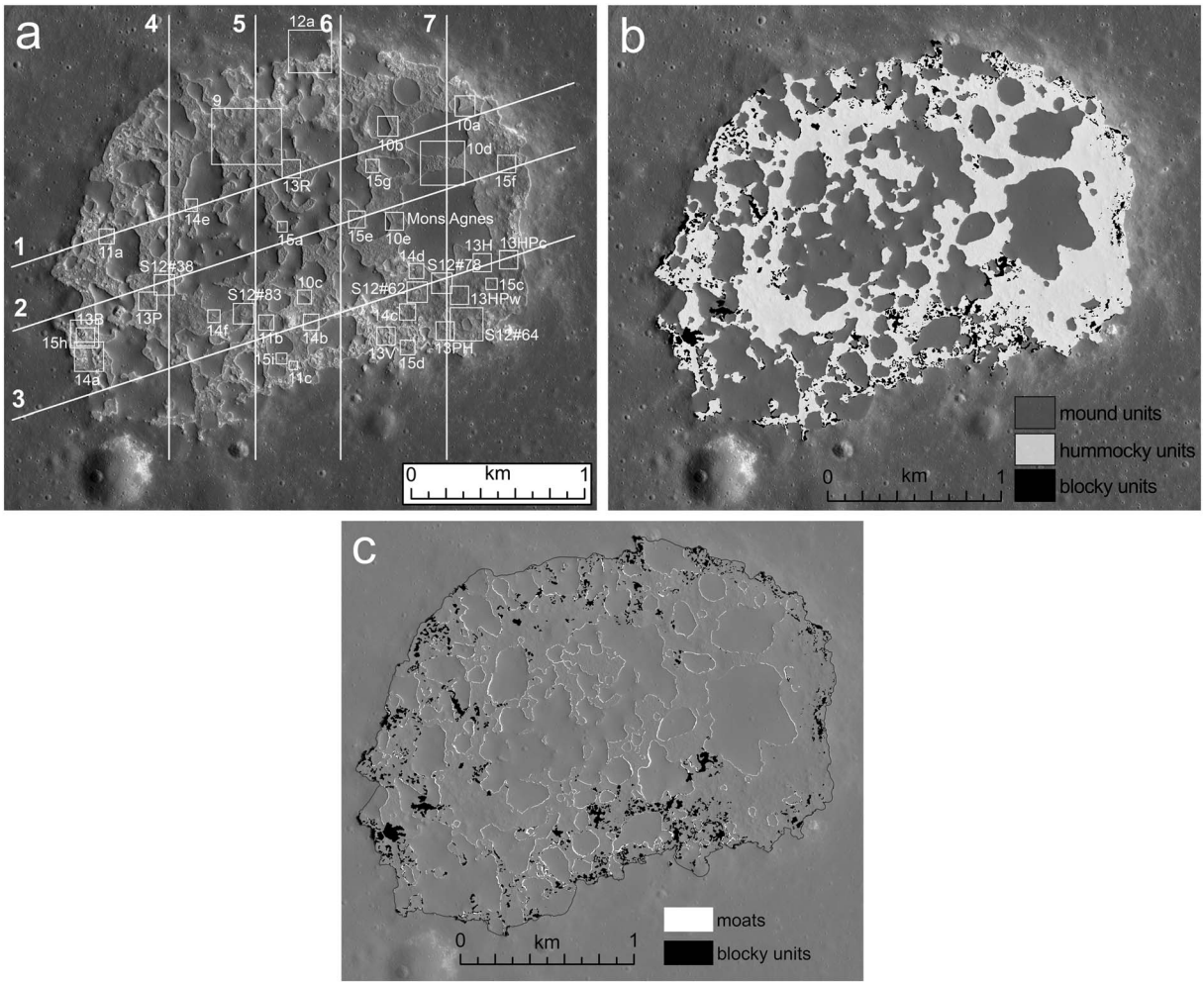


Figure 5. (a) Ina pit crater interior imaged by LROC NAC frame M119815703, pixel size = 0.48 m, incidence angle = ~56°. The white lines mark the locations of topographic profiles shown in Figure 7, with their starting points labeled by the profile numbers, and the white boxes mark the locations of Figures 9–15 and S12. (b) Geologic sketch map shows the spatial distribution of the multiple morphologic units of Ina interior; background is a portion of LROC NAC M119815703. (c) Spatial distribution of moats (white lines, surrounding mounds) and blocky units (black patches) within Ina.

have a total surface area of 2.27 km^2 and occupy ~50% of the Ina interior area. The surface area of individual mounds ranges from 340 m^2 to 0.72 km^2, with an average value of 0.025 ± 0.087 km^2; the mounds display a log-linear area distribution (Figure S3, Vaughan & Head, 2012). The maximum length of all the Ina mounds ranges from 0.03 to 2 km, with a bimodal frequency distribution pattern, peaking at 0.04–0.06 and ~0.2 km (Figure S4).

For all the Ina mounds, their distances from the depression geometric center (18.6544°N, 5.30262°E) are approximately normally distributed, peaking between 800 and 1,000 m (Figure S5). Of the 88 identified mounds, 15 of them are spatially continuous with the depression walls, and relatively flat ledge terrains are often observed between the walls and most of these wall-connected mounds (Figure 5). For the other mounds, which are not connected with the depression wall (n = 73), the distribution of the distance from mound margins to the Ina interior floor edge is shown in Figure S6. The majority of the Ina mounds are within ~300 m of the floor edge, while some very small mounds (typically less than ~0.01 km^2) occur in the interior portion of the depression floor (Figure 5b).

The summits of the mounds are always below the rim of Ina (with an average elevation of ~ − 274 m, Figure 6a); the average elevation of Ina mound summits (~312 m) is ~38 m below the rim, with a range of ~33 m (Figure S7); the mound summit elevations decrease (relative to the rim crest) toward the center of

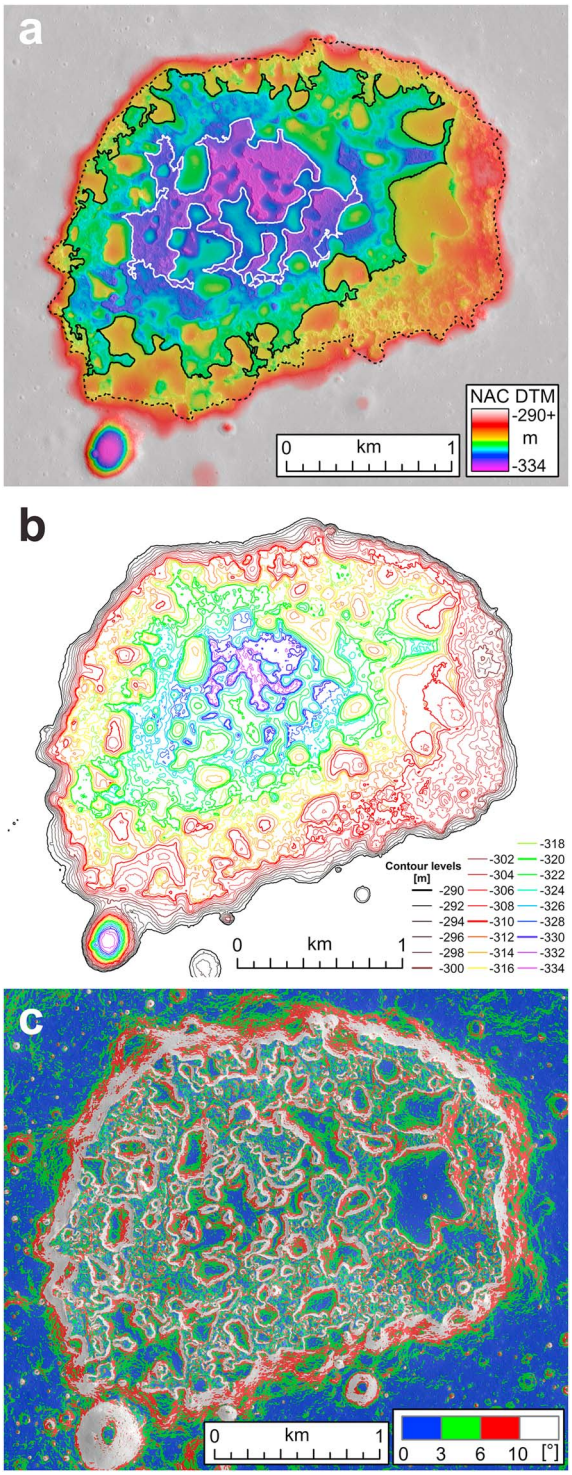


Figure 6. (a) Topographic variations of the Ina pit crater floor: colorized NAC DTM topography overlain on LROC NAC M119815703. The black dashed outline marks the boundary of the Ina interior floor, and the black and white solid lines are the contours -314 m and -324 m, respectively, to define the three annular terraces of the floor topography (see the details in section 3.4 and Figure S14). (b) LROC NAC DTM-derived contour map of the Ina interior, contour interval is 2 m (modified from Figure DR1 of Qiao et al., 2017). (c) NAC DTM slope map for the Ina pit crater, overlain on LROC NAC M119815703.

Ina (Figures 6 and 7, Garry et al., 2012; Qiao et al., 2017). We measure the proximal terrain topography around the Ina mounds, with a distance of 5–30 m from the mound edges to avoid the topographically lowest moats, usually present at the mound margins. The difference between the summit elevation of each mound and the average elevation of the proximal floor region is calculated as the height of each mound. Examination of the height-frequency distribution of the Ina mounds and their average areas (Figure S8) shows an obvious size-height grouping: smaller mounds are generally shorter than their larger counterparts. For the 60 smaller mounds (surface area < ~0.01 km^2), their heights are generally within ~8 m. While relatively larger mounds generally have much greater heights, for 22 mounds higher than 8 m, 14 of them have surface areas greater than ~0.03 km^2. The calculated volumes (assuming a plane base model) of 85 identified mounds (excluding those mounds with negative calculated heights) on the Ina floor total 0.0258 km^3 and show a wide range for individual mound volumes between 41 and 9.2 × 10^6 m^3 (Figure S9), with mean and median values of 3.0 × 10^5 and 1.6 × 10^4 m^3, respectively. Individual Ina mounds mainly exhibit roughly elliptical map-view shapes (Figure 5b), while much more extensive mounds generally exhibit complex, coalescing bleb-like shape patterns (e.g., the largest mound in the center, Figure 5b), and appear to *"be composed of multiple mounds that are interconnected"* (Garry et al., 2012). The mounds are generally characterized by convex cross-sectional profiles, with surface topography becoming steeper toward the margins (Figures 6 and 7 in Garry et al., 2012). The cross-section profiles are often asymmetric, the surface elevation typically tilts toward the pit crater floor interior, with a maximum relief between one side of a mound and the other side of up to ~12 m (Figure 7 in Garry et al., 2012). In addition, relatively larger mounds (>100-m wide) commonly develop nearly flat tops (mainly <2° in surface slope) (Figure S10) where the total topographic relief is only 1–2 m over hundreds of meters (Garry et al., 2012).

We calculated the surface area-averaged topographic slope and orientation of each mound (Figure S11) based on LROC NAC DTM raster topography, using the following algorithms:

$$\text{slope} = \text{atan2}\left(\frac{1}{N}\sum_{i=1}^{N}\frac{dz}{dx}, -\frac{1}{N}\sum_{i=1}^{N}\frac{dz}{dy}\right) \quad (1)$$

$$\text{orientation} = \text{atan}\sqrt{\left(\frac{1}{N}\sum_{i=1}^{N}\frac{dz}{dx}\right)^2 + \left(\frac{1}{N}\sum_{i=1}^{N}\frac{dz}{dy}\right)^2} \quad (2)$$

where *slope* and *orientation* are in radians, N is the number of pixels in each mound, and dz/dx and dz/dy are the rates of the topographic change in west-east and north-south directions, respectively. The averaged topographic slope and orientation distribution map of the Ina mounds shows that the majority of these mounds have area-averaged slopes toward the pit crater center (Figure S11), supported by observations from contour maps (Figure 6) and cross-sectional profiles of individual mounds (Figure 7 in Garry et al., 2012 and Figure 7). This orientation distribution pattern implies that there was a potential tendency for the materials forming the mounds to flow inward toward the inner lower floor.

Six mounds are located in depressions (termed *low mounds*), that is, terrain units with smooth textures analogous to those of typical convex

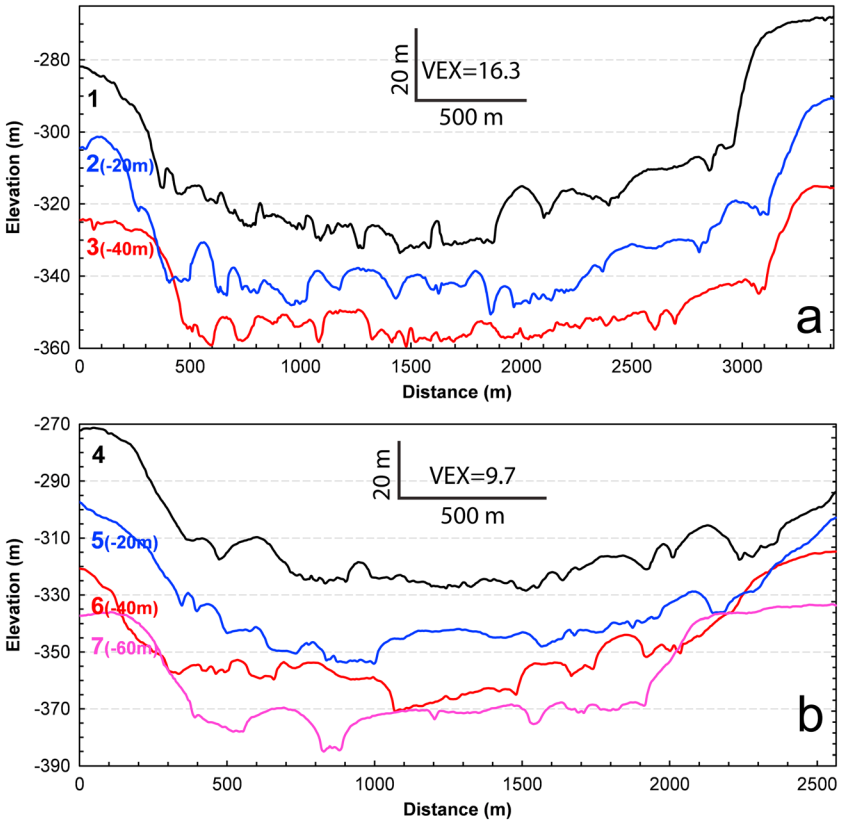


Figure 7. (a) West-east and (b) north-south topographic profiles crossing the Ina interior, derived from NAC DTM topography, with vertical exaggeration (VEX) labeled. The locations of these profiles are shown in Figure 5a, and the profile numbers correspond to those shown there. For clarity, profiles in each panel are offset by −20 m in succession.

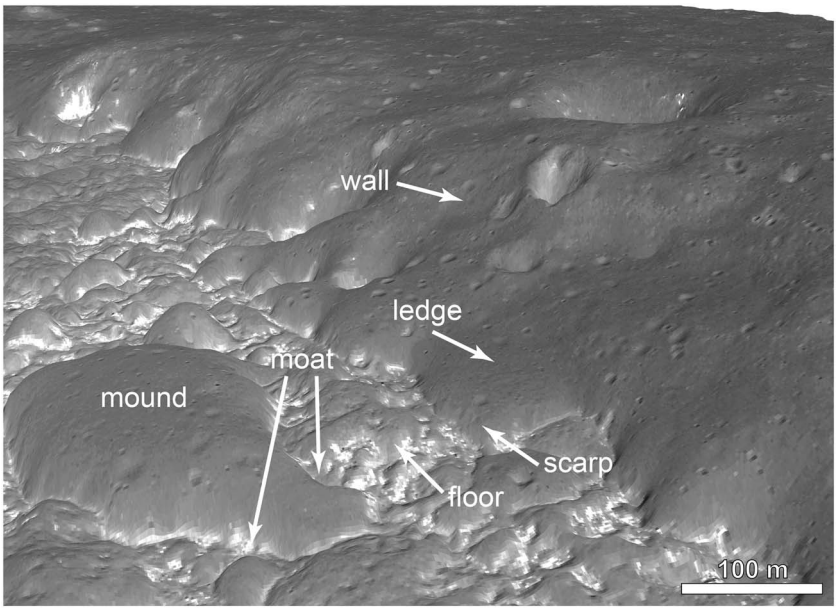


Figure 8. Perspective view of southern middle edge of the Ina interior, showing the morphological transition from the shield volcano (including wall, ledge, and scarp) to Ina floor (including floor terrains and mounds with surrounding moats). LROC NAC frame M119815703 overlain on LROC NAC DTM topography. View is looking southeast and vertical exaggeration is ~5.0.

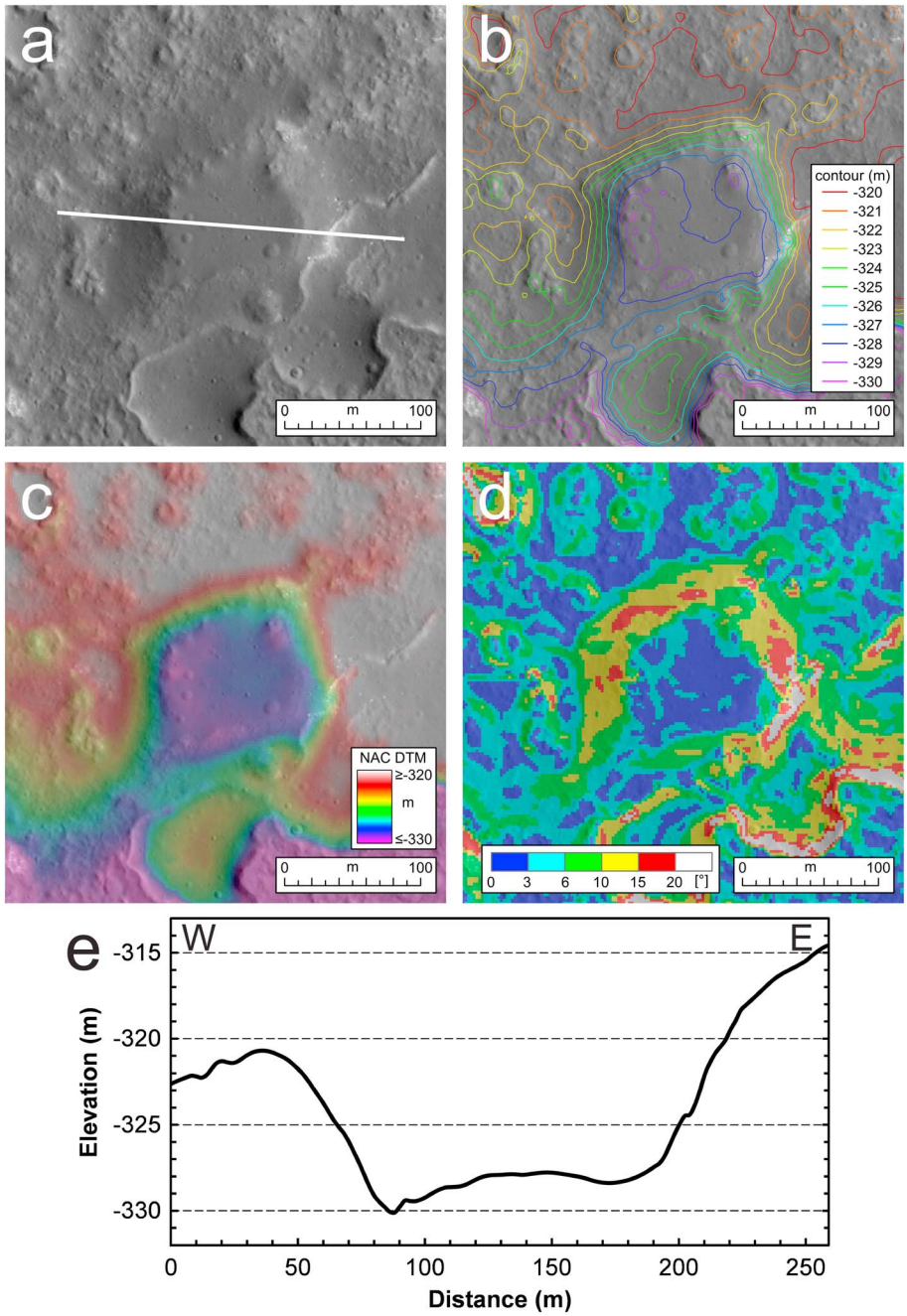


Figure 9. The largest *low mound* (topographically lower, while smoothly textured terrain) of the Ina interior, with a diameter of ~200 m. (a) Portion of LROC NAC M119815703; the location of the topographic profiles shown in Figure 9e is marked by the white line, (b) NAC DTM-derived contour overlain on LROC NAC M119815703; contour interval is 1 m, (c) colorized NAC DTM topography overlain on LROC NAC M119815703, (d) NAC DTM-derived topographic slope, and (e) west-east topographic profile across this depression feature.

mounds on LROC NAC images, and elevation decreasing toward the margins (similar to the other typical mounds), while abnormally lower than the surrounding floor terrain. With one exception (#81 in Figure S2) that is relatively extensive with a maximum length of ~200 m (Figure 9), the other five low mounds are rather small, generally shorter than ~50 m (Figure S12), and also lie within much shallower (0.1- to 2.5-m deep) depressions (Table S1).

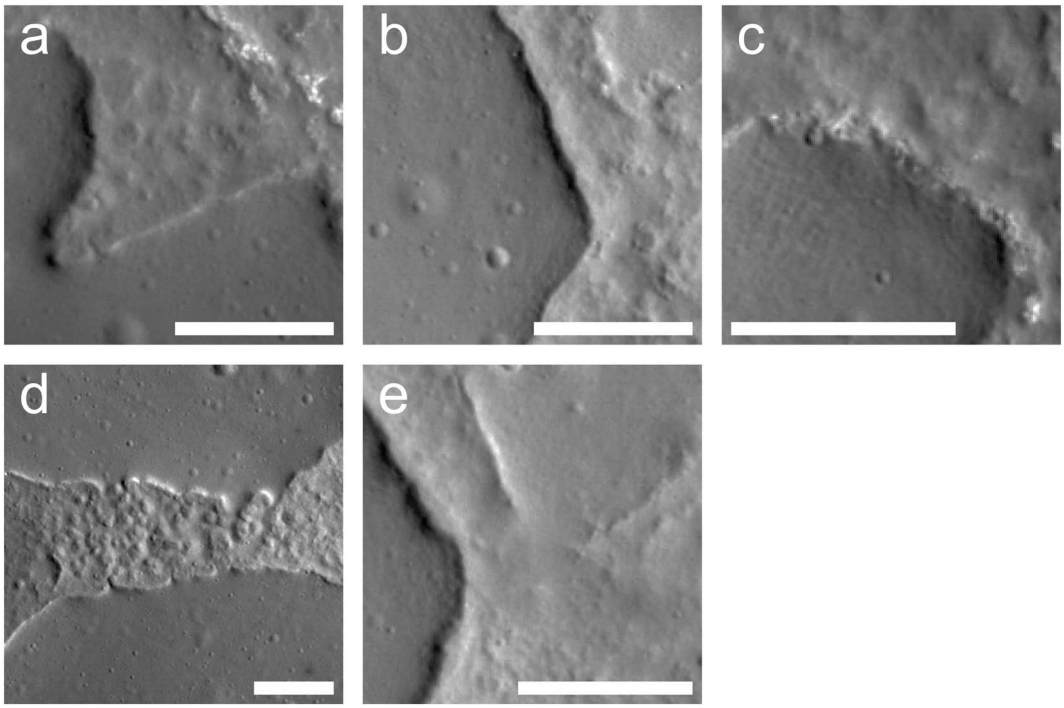


Figure 10. Morphologies of the mound-floor transition area: (a) clearly defined boundary, (b) topographically lower moat occurring at the transition, (c) blocky materials exposed in the moats, (d) gradual finger-like morphologic transitions, and (e) continuous morphologic transitions. All panels are portions of LROC NAC frame M119815703, and each scale is 50 m.

The largest low mound is present within an ~200 × 150 m, roughly trapezoid-shaped depression (Figure 9a). The bottom (*mound*) is ~100 × 80 m in size. Relative to the proximal terrains, this mound is typically ~7-m deep and has a maximum depth of ~10 m at the western margin (Figures 9b–9e). The slope along the depression wall ranges from 5 to 15° and increases to 15–30° in limited areas (Figure 9d). This low mound is also characterized by convex cross-sectional profiles (Figure 9e), similar to normal uplifted Ina mounds (Figure 7). Locally, the mound surface largely slopes toward the west, with the eastern portion generally 2–3 m higher than the west, and it reaches the highest elevation at the northeast margin, with a maximum relief of nearly 6 m. Topographic moats, several meters wide and up to ~1-m deep, are observed to surround the smooth terrains (Figure 9e). The NAC DTM-derived slope of this mound surface is generally flatter than 3°, while the northwest marginal areas show slightly elevated slope (3–6°).

The transition area between Ina mounds and the crater floor shows a wide range of morphology and topography (Garry et al., 2012). Parts of the mound margins have clearly defined boundaries with the floor units (Figure 10a), occasionally with topographically lower moats present at the transition region (Figure 10b). Some intervening moats are filled with blocky materials and/or rubble piles (Figure 10c). However, the majority of the mound-floor boundaries are not clearly defined, being instead characterized by gradual morphologic transitions from mounds to finger-like features and pitted units, with complex, multibranched morphologic patterns (Figure 10d). These small finger-like features extending from the mound margins appear to have similar surface textures to those of the mound terrains and commonly connect with the lower pitted terrains (Garry et al., 2012). The pitted terrains are composed of ridged or vermicular hillocks up to ~1-m high and decameter-scale irregular depressions (Figure 10d). In some rare cases, the mounds are spatially continuous with the lower hummocky units, and neither morphologic boundaries nor small finger-like features are observed (Figure 10e). The transitions between the Ina depression wall and floor generally have similar morphologic patterns to the mound-floor transitions, though dominated by clearly defined geomorphologic boundaries.

There are also dozens of unusual depressions (designated as Category 3 depressions in section 3.6) observed on the floor terrains (Figure 11; see discussion of their differences from other depressions within Ina in section 3.6). These depressions are roughly circular to elliptical in shape and develop a relatively extensive

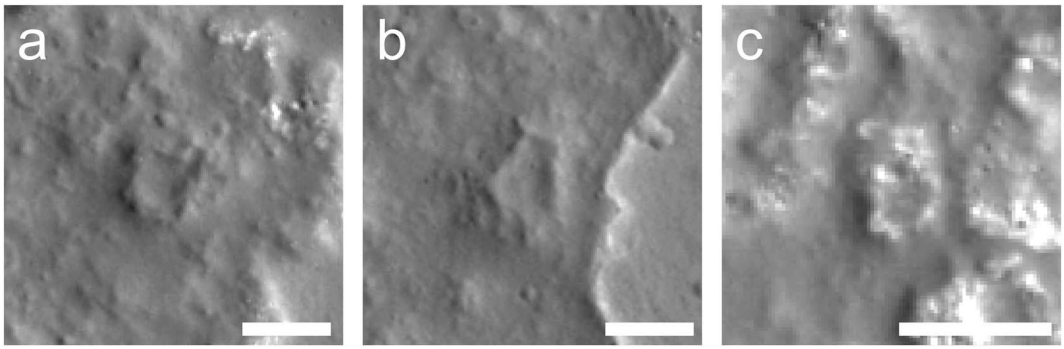


Figure 11. Unusual depressions with a relatively extensive central uplifted structure, on the floor units: (a) circular, (b) elliptical, and (b) rocky materials within the marginal ring of low-lying areas. All panels are portions of LROC NAC frame M119815703, and each scale is 20 m.

central uplifted structure (Figures 11a and 11b). Alternatively, they can be described as small domes/mounds surrounded by a ring of topographic moats. The central domes/mounds are clearly different from the internal mound structure of the relatively common *central-mounded* impact craters on the lunar surface (e.g., Bart, 2014). The central structures appear to have similar surface textures to the Ina mounds, while having comparable elevations to the surrounding floor units. In addition, bright boulders are usually present within the marginal ring of topographic lows (Figure 11c). These moat-mound structures share many morphological similarities with the so-called *ring-moat dome structures* (Zhang et al., 2017). We interpret these unusual central uplifted structures as possible miniature analogs of Ina mound units, and the marginal ring of lows analogous to the moats frequently occurring along the edges of Ina mounds, where fresh boulders are also often observed (Figure 5c).

3.3. Ledge and Scarp

There are also about a dozen mound structures present at the edge of the Ina interior, which connect the surrounding depression wall and the lower floor terrain (Figure 5). Unlike the typical convex upward mounds on the central floor, these marginal mounds usually exhibit multiple slope breaks (Figures 8 and 12), permitting us to define the transition region into an inward facing wall (5–10° slope), a relatively flat (<~5°) ledge, a steep (10–30°) inward facing scarp, and the topographically lowest floor, in an inward sequence. The ledges are typically ~50-m wide (~30- to 120-m range), though they are not always well developed in some marginal areas. The inner scarps are typically ~50 m wide and ~12-m high, with topographic slopes increasing inward and downward and reaching maximum slopes over 30° (Figure 12b). The marginal ledges and scarps delimit the Ina floor terrains; they appear to be the edge of an outer boundary layer and have comparable topographic slopes to those of the Ina floor units. Among the 15 mounds that are connected with the depression walls, 13 of them develop the relatively flat ledge formations, while the other two mounds have very narrow connecting bridges with the surrounding mare shield (Figures 5 and 6).

3.4. Floor Elevation

The Ina floor terrains (including both hummocky and blocky units) are approximately confined between the LROC NAC DTM contours −304 and −300 m (Figures 5 and 6), indicating that the floor terrain was probably once a hydrostatic surface, for example, a lava-flooded pond surface (Qiao et al., 2017). The floor terrain has a total surface area of ~2.28 km^2, making up ~50% of the entire Ina interior. Almost all of the floor terrains are spatially connected, except several very small marginal or intermound floor units, which are generally smaller than ~150 m in dimension (Figure 5b). The elevation of the entire floor terrain ranges from −334 to −296 m, with a mean value of −316 m (1σ = 7.6 m; Figures 6 and S13), which is typically up to ~10–20 m lower than the proximal mounds (with an average summit elevation of 312 m, 1σ = 7.8 m; Figure S7).

The elevation of the floor terrains shows an apparent decreasing trend toward the center of Ina (Figures 6 and 7) and can be broadly categorized as three annular terraces, with ~10-m elevation decrements (Figures 6a and S14). The first terrace (Annulus 1, red patches in Figure S14) extends inward to contour −314 m (Figures 6 and S13), the second terrace (Annulus 2, green patches in Figure S14) can be defined

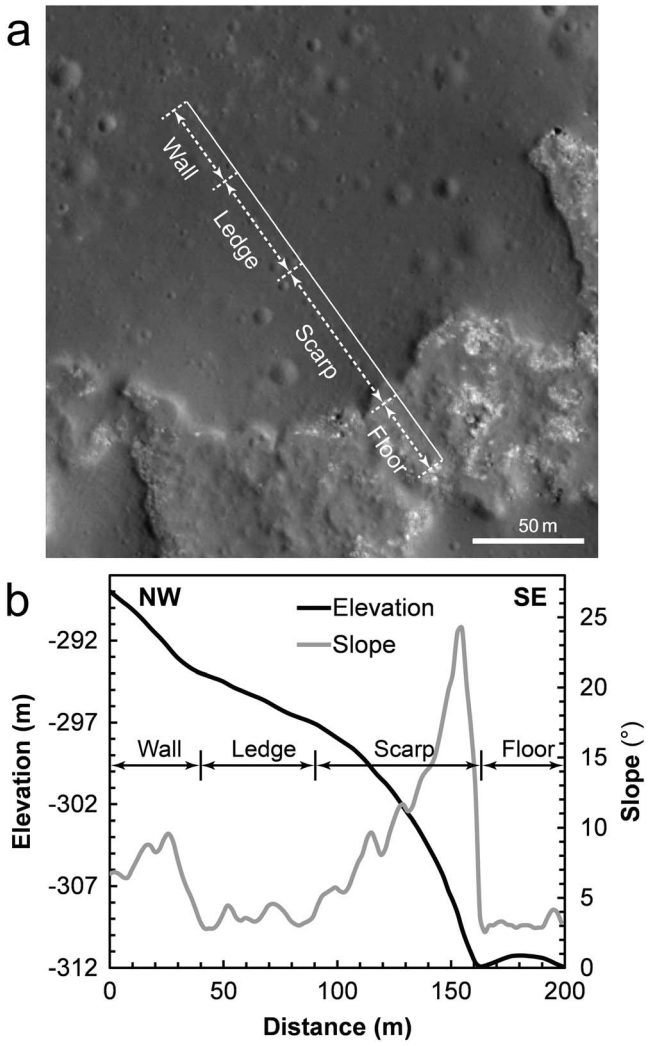


Figure 12. A sample of ledges and scarps observed at the north margin of Ina: (a) LROC NAC images (portion of LROC NAC M119815703) and (b) NAC DTM elevation (black curve) and slope (gray curve). The approximate extents of each morphologic unit (wall, ledge, scarp, and floor) are marked.

between contours −314 and −324 m (Figures 6 and S13), while the interior-most and lowest areas can be regarded as the third terrace (Annulus 3, blue patches in Figure S14). A part of the boundaries between these terraces seems to be related to surface morphologic features. For instance, the Annuli 1 and 2 boundary near the northeastern edge of Mons Agnes (Figure 5a) is characterized by a stripe-shaped area with apparently elevated slopes (>10°, Figure 6c) and a morphologic transition from hummocky terrains (unit H) to highly pitted and ridged terrains (units HPw and R, Figure 13). The existence of multiple annular units within the Ina floor suggests potential multiple stages of surface emplacement/modification processes, for example, lava lake inflation and deflation cycles (Qiao et al., 2017). In addition, the interior mounds appear to occur preferentially at the contacts between the annular terraces (Figure S14), plausibly supporting the formation scenario of Ina mounds by the hypothesized magmatic foam extrusions through the fractures (e.g., caused by the subsidence of the lava lake crust) within the floor terrains proposed by Wilson and Head (2017b) and Qiao et al. (2017).

3.5. Hummocky Unit

Initial examination based on Apollo photographs had already noted the geomorphological variations within the Ina floor terrains, for instance, the rough-textured units with interlocking polygonal hummocks and dark hilly units (Strain & El-Baz, 1980). Newly identified properties of the floor units include hummocky, pitted, ridged, polygonal, and vermicular textures. In addition, differently textured surface portions of the Ina floor commonly group with variable spatial patterns, further complicating the surface geomorphology of the floor terrain. The intricate combination of various surface textures indicates highly complex geological activities and emplacement mechanism, and probably intertwinement of products from different surface processes. We here make a detailed subdivision of the floor terrain into eight geomorphologic subunits (Figure 13):

1. *Fine-textured and hummocky units (H)*. These units are composed of relatively smooth, fine-textured terrains, interspersed with very small (typically <5 m) circular to polygonal hummocks. These units appear to have the smoothest surface texture (comparable to that of the mound units) among all the floor terrains, with the least occurrence of topographic pits and ridges.
2. *Hummocky and moderately pitted units, with closely spaced pits and ridges (HPc)*. HPc units are characterized by a hummock-dominated surface texture, while interspersed with abundant tiny and closely spaced pits and ridges.
3. *Hummocky and moderately pitted units, with wide-spaced pits and ridges (HPw)*. HPw units have a similar surface texture to HPc units, but they appear relatively smoother on an optical image than the HPc units, and the pits and ridges within them are more widely spaced (sparse).
4. *Hummocky and highly pitted units (PH)*. PH units are composed of circular or irregular hummocks, with interspersed abundant tiny pits, thus showing an elevated surface roughness relative to the above units.
5. *Ridged and pitted units (R)*. These terrains are composed of ridged or vermicular to polygonal hillocks up to ~1-m high and some decameter-scale irregular depressions and exhibit relatively coarser surface textures at longer baselines than hummocky units.
6. *Vermicular units (V)*. Vermicular units are composed of vermicular ridges and inter-ridge floor materials. These vermicular structures are generally much larger than the more common ridges within the above (HPc, HPw, PH and R) units. Bright blocky materials are commonly present within the inter-ridge floors.

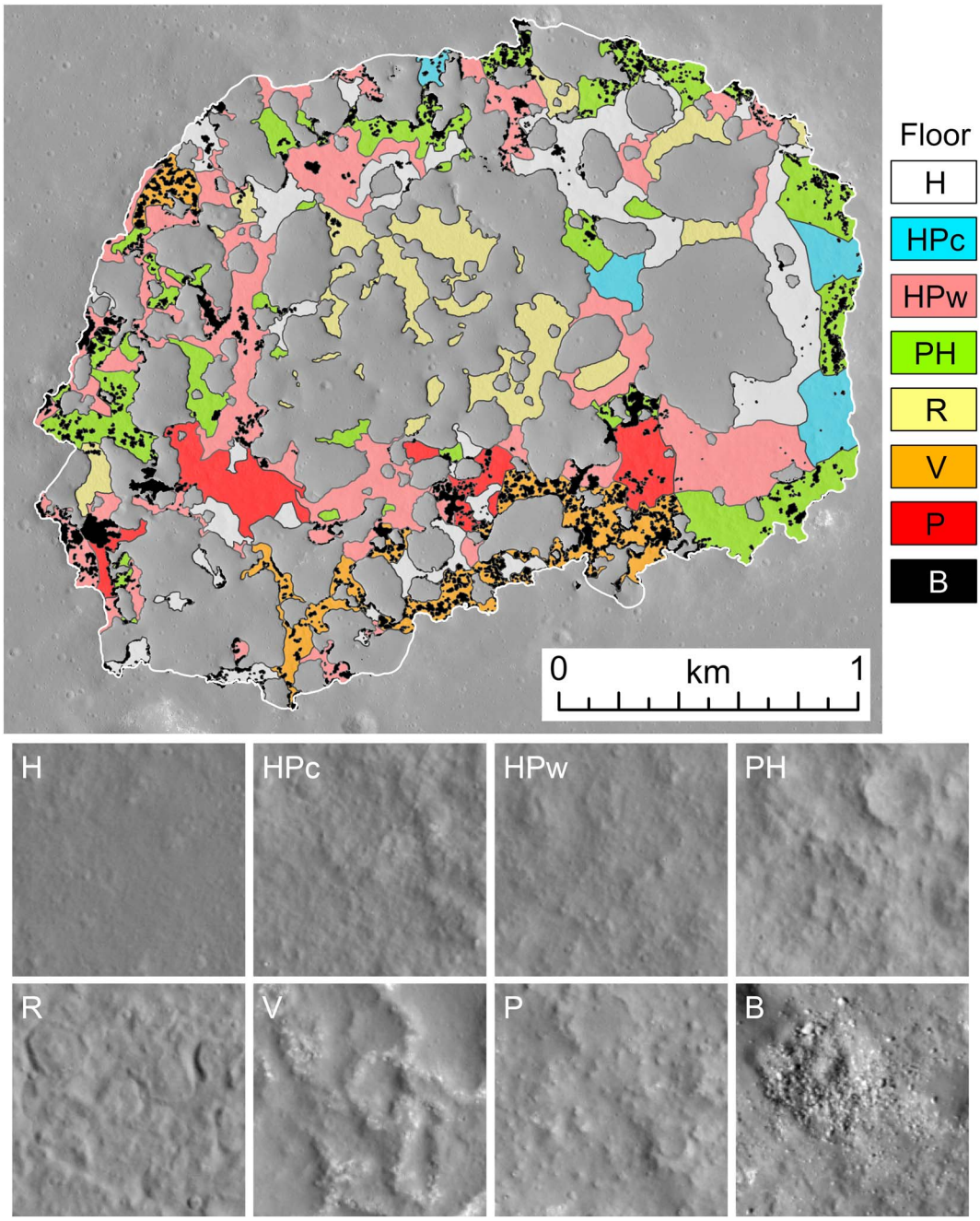


Figure 13. Geomorphological division of the Ina floor terrains (above): H: fine-textured and hummocky units, HPc: hummocky and moderately pitted units, with closely spaced pits and ridges, HPw: hummocky and moderately pitted units, with wide-spaced pits and ridges, PH: hummocky and highly pitted units, R: ridged and pitted units, V: vermicular units, P: pitted units, B: blocky units (see texts in section 3.5 for the detailed description of each unit). The LROC NAC images (below) show the examples of each unit; each panel is 106 × 106 m.

7. *Pitted units (P)*. Pitted units are characterized by a hummocky surface texture with abundant tiny (<5-m long) circular pits. These unusual pits are characterized by preferentially conical shapes, steep inner walls, and no observed associated floors, elevated rims, and surrounding ejecta, suggesting that they may represent locations where surface materials have drained into the subsurface (see more detailed characterization in section 3.7).
8. *Blocky units (B)*. Blocky units are composed of freshly exposed boulder fields, characterized by apparently elevated surface reflectance.

3.6. Depressions Inside Ina

There are various kinds of topographic depressions within Ina. We categorize these depressions/structures into three major classes according to their morphology, topography, surface texture, and spatial association with other terrains:

Category 1: *Craters*. This category includes both typical bowl-shaped craters interpreted to be of impact origin (similar to the most common craters on the lunar mare regolith surface) and unusual, (approximately) circular or subcircular depressions with observed wall and floor structures sometimes bounded by a raised rim (for relatively fresh impact craters); these are interpreted to be poorly developed and/or highly modified impact craters (see detailed characterization in section 3.10).

Category 2: *Regolith pits*. These pits are generally very small (<5 m), rimless, without surrounding ejecta, blocky interior or a detectable floor, and have very steep inner walls (see detailed characterization in section 3.7). They are interpreted to be regolith drainage pits.

Category 3: *Annular-moat mounds*. These depressions are characterized by central dome/mound structures surrounded by annular moats. The central mounds in the depression interior seem to have surface textures similar to those of the Ina mounds, while having comparable elevations to those of the surrounding (preemplacement) floor terrain (see section 3.2 and Figure 11). While the central structures are generally much larger than those in the more common central-mounded craters (e.g., Bart, 2014). These are interpreted to be mound extrusion-induced surface subsidence depressions.

3.7. Pits

We have observed abundant pit structures in the Ina interior terrains (Figure 14). These pits (designated as Category 2 depressions in section 3.6) are generally <5 m in diameter and have various map-view shapes, including circular, elliptical, narrow, and irregular. There is a host of unusual morphologic characteristics that distinguishes these pits from impact craters (including both typical impact craters on the lunar mare and regolith surface, and depressions within Ina interpreted to be atypical impact craters, see sections 3.6 and 3.10): preferentially conical shapes, absence of elevated rims and ejecta deposits, steep inner walls, no observed floors (i.e., like a *hole*), and much greater depth/diameter ratios than for typical lunar impact craters (e.g., Daubar et al., 2014; Pike, 1974).

Most of these pits are observed on the floor units (Figures 14a–14d), and very few are located at the margin of the mounds (Figures 14e and 14f). Many pits are spatially aligned (Figures 14a–14c) or clustered (Figure 14d). Some aligned pits are nearly spatially connected and coalesce into linear troughs (Figures 14a, 14c, and 14f). High-albedo blocky materials are commonly present within these aligned pits (Figures 14b and 14d), implying that the surface regolith may have mostly drained into the voids below or blown out (Schultz et al., 2006), and shallow subsurface bedrock has been exposed.

3.8. Moats

Topographically lower moats along the steep perimeter of Ina mounds are another major mystery concerning the origin of Ina and other large IMPs (Garry et al., 2012; Qiao et al., 2017, Figures 8 and 10b). Geomorphological mapping on high-resolution LROC NAC images (~0.5-m pixel size) shows that moat structures occur at the margins of almost all Ina mounds (Figure 5c), though some moats might not be well resolved on the relatively lower resolution NAC DTM topography (2 m/pixel). The width of these topographic moats can range from a few meters to ~13 m, with a typical value of ~5 m. Most of these moat features are generally <1 m deep, while some can reach a maximum depth of ~2 m. The moats occurring along the marginal annulus of the Ina interior commonly occur together with blocky units (Figure 10c), while blocky materials are seldom observed within the central moats (Figure 5c). In addition, we observe no obvious spatial continuity of moats with regolith drainage pits on the floor terrains (see section 3.7).

3.9. Blocky Unit

The apparently optically immature blocky materials within Ina are another major characteristic that has perplexed lunar scientists for decades. In earlier analyses based on relatively coarser resolution Apollo orbital photographs, the blocky units are often described as *bright* or *white* units (El-Baz, 1972; Strain &

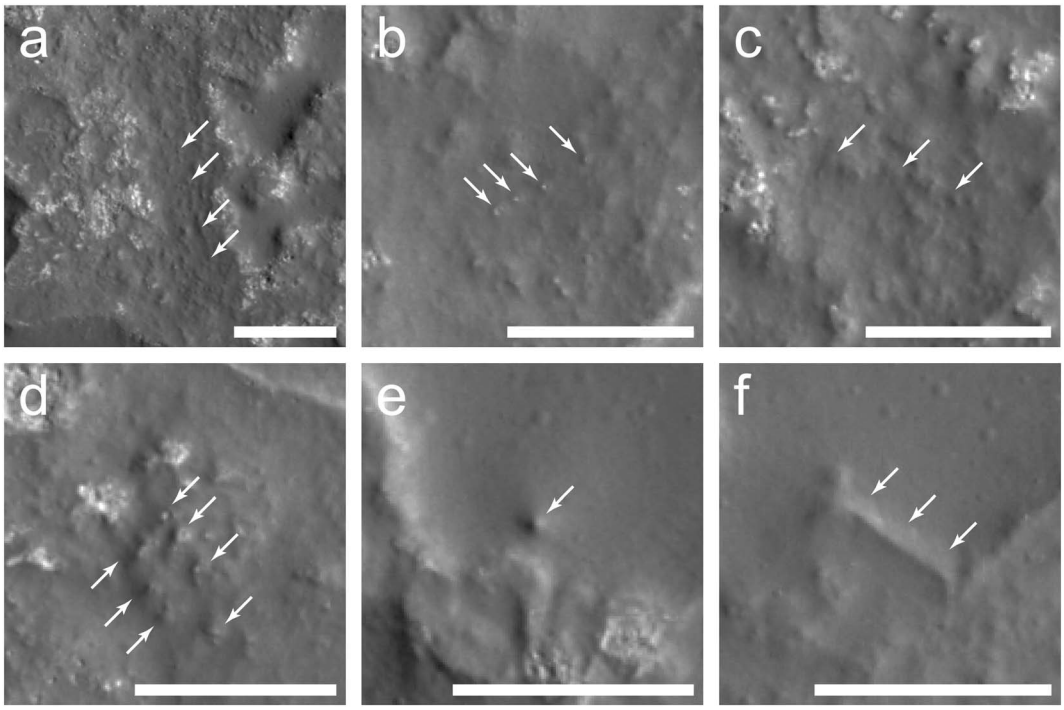


Figure 14. Pits (marked by white arrows) observed at Ina interior terrains; each scale is 50 m. All panels are portions of LROC NAC frame M119815703.

El-Baz, 1980); submeter LROC NAC images show unequivocally that blocky units are basically freshly exposed boulder fields (Garry et al., 2012), with individual boulders reaching ~5 m in dimension; these are, however, much smaller than the largest boulders at Sosigenes, another major IMP occurrence (up to ~12 m, Qiao et al., 2016, Qiao, Head, Xiao, Wilson, & Dufek, 2018).

LROC NAC image-based geological mapping shows that the Ina blocky materials occur dominantly at the marginal annulus of the Ina floor (Figure 5b): within Annulus 1 and close to the contact between Annulus 1 and 2 (Figure S14 and section 3.4), with a small portion of such blocky materials scattered in the topographical moats surrounding the mounds (Figures 5c and 10c). In addition, impact cratering on the floor terrains may also expose blocks within craters or eject them to the adjacent floor and mound terrains (see detailed characterization in section 3.10 and Figures 15g and 15h). There are also some individual boulders present within the hummocky units (Figure S12 upper right panel), probably ejected from some distant craters, or exposed in situ. The spatial distribution of the blocky units also corresponds to the areas of least optical maturity (Garry et al., 2013, Figure 19b) and steepest slopes (Figure 6c), suggesting that they are the most recently exposed surface materials among the entire Ina interior components.

The blocky units in the central portion of the interior of Ina typically have relatively small spatial extents (<~30 m), and relatively smaller sizes of the exposed boulders (Figure 5b), and in some areas, boulders are not well resolved on the half-meter resolution NAC images (in these cases, the identification of blocky units is based on their unusually high albedo and rough surface texture). The blocky units occurring at the marginal annulus of the Ina interior exhibit a much larger spatial extent of fresh boulder fields (up to ~100 m) and relatively higher spatial density and larger sizes of exposed boulders (Figure 8), as evidenced by the unusually great brightness of the marginal portions of the Ina interior (Figure 5a).

3.10. Impact Craters: Geomorphology

Based on our careful geomorphologic analyses and comparison with other topographic depressions inside Ina (section 3.6), we interpret these (approximately) circular or subcircular depressions with observed wall, floor structures, and possible raised rim formations (though sometimes relatively less apparent for mature craters), as meteoritic impact craters (designated as Category 1 depressions in section 3.6). These include both typical bowl-shaped craters (Figure 15a) and unusual craters (Figures 15c–15i) on Ina interior terrains.

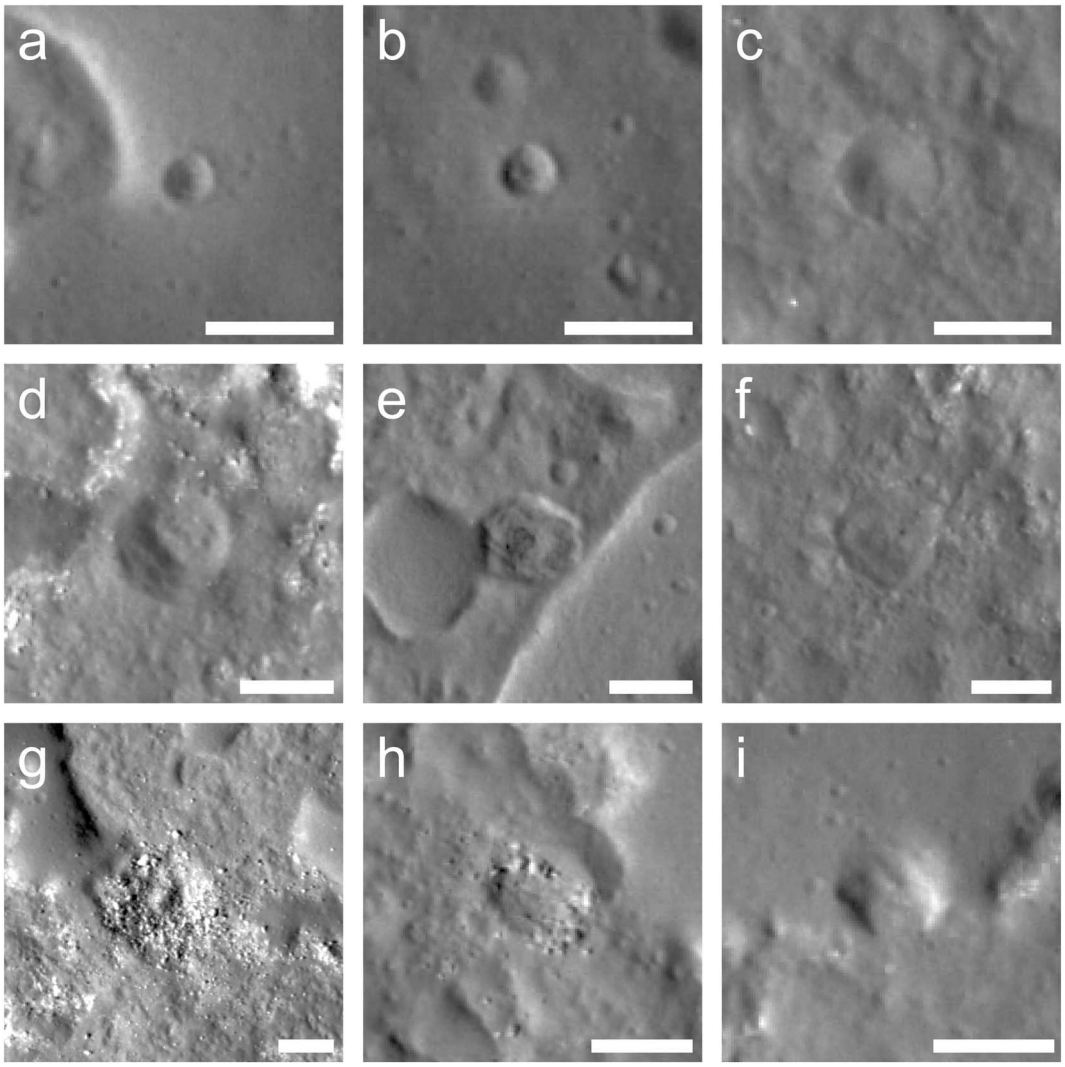


Figure 15. Impact craters on the Ina interior terrains: (a) a crater with relatively sharp rim crests on the mounds, (b) a crater on the surrounding mare (for comparison; centered at 18.453°N, 5.311°E), with comparable rim morphology crispness of the crater in Figure 15a, surrounding halo formation is observed, (c–e) representative craters on the floor terrains, (f) a very shallow impact crater on the floor, (g–h) blocky craters on the floor, and (i) a crater at the mound-floor boundary. All panels are portions of LROC NAC frame M119815703, and each scale is 20 m.

Most impact craters superposed on the mounds have common bowl-shaped cross-section profiles, similar to the most frequently observed craters elsewhere on the lunar surface. Nearly all the mound craters, even the fresh-appearance ones (as evidenced by their sharp rims, Figure 15a), do not exhibit a blocky interior or associated surrounding ejecta fields, halos, and ray patterns. These craters seem to be different from their counterparts on typical mare regions (Figure 15b), suggesting that the mound craters probably degraded very quickly, or that they may represent impacts into unconsolidated materials, for example, solidified magmatic foams (Qiao et al., 2017; Wilson & Head, 2017b).

However, impact craters identified on the floor terrains show a wide range of morphologies, often very complex, and are significantly different from those on both the mound units and surrounding mare regions. Almost none of the floor craters have typical bowl-shaped profiles; in contrast, they are generally characterized by relatively shallow floors and irregular interior structures (compared with their counterparts on Ina mounds and the surrounding mare; Figures 15c–15f), suggesting that these craters are poorly formed, highly modified and/or may represent impact into unusual targets other than typical lava flows or regolith materials, for example, impact cratering into highly porous targets (Figure 2 of Housen et al., 1999; Figure 8 of Housen & Holsapple, 2003). In addition, exterior ejecta materials, blocky interior structures, and ray or

halo patterns are generally not observed to be associated with these craters, even for those with relatively sharp rims (Figure 15d). Some of the floor craters display concentric and central-mounded interior structures (Figures 15e and 15f), which are very different from those of fresh craters formed on layered targets (typically with an unconsolidated layer overlain on a more cohesive layer, Bart, 2014). However, several craters on the floor terrains have developed a variable extent of boulder fields in both the crater interior and exterior (Figures 15g and 15h), indicating that these impacts have penetrated the unconsolidated surface materials (commonly lunar regolith) and excavated the underlying blocky materials. Based on the measured diameters (as small as ~20 m) and the scaling law between crater diameter and excavation depth (Melosh, 1989), the thickness of the surface regolith accumulated on the floor units can be roughly constrained to be <~1.7 m (consistent with the 10- to 15-cm regolith thickness lower limit value reported by Elder et al. (2016, 2017)).

There are also some impact craters occurring at the boundaries between the mounds and floor terrains (Figure 15i). The morphology of a crater of this kind shows significant differences between the part on the mound and the other part on the floor: the mound part is relatively well developed, resembling the bowl-shaped craters entirely formed on the mounds (Figure 15a), while the typical crater morphologies (including wall, floor, rim, etc.) on the floor part are hardly visible. This morphological discrepancy strongly indicates the fundamental differences in target properties between the mounds and floor terrains and the effects they exert on crater formation and subsequent degradation: the craters on the floor either are poorly developed or degrade rapidly compared with their counterparts on the mounds.

3.11. Impact Craters: Size-Frequency Distributions

In addition to their morphological peculiarities (section 3.10), the impact craters within the interior of Ina are also distinctive and unusual in their remarkably low areal density, suggesting a 33.2-Ma model age for the mounds through a crater population study on LROC NAC imagery data (Braden et al., 2014). To investigate the detailed nature of and potential causes responsible for the extreme paucity of superposed impact craters on the Ina mounds, we performed a careful crater counting analysis (for craters ≥10 m in diameter) using LROC NAC images with a range of illumination geometries (solar incidence angle up to 87°; Figure 16). Moreover, due to the highly complicated surface textures and unusual crater morphologies of the floor terrain, the impact crater SFDs of the floor units and how they compare with those of other adjacent terrains are both poorly understood and remain controversial (cf. Braden, 2013; Braden et al., 2014; Robinson, Thomas, et al., 2010). Based on our analyses of the morphological characteristics and recognition criteria of the atypical impact craters superposed on the floor terrain (section 3.10), we here also identify and measure all impact craters ≥10 m in diameter on the Ina floor units using LROC NAC images (Figure 16a). For comparison, we also transfer the map of the Ina interior units to the upper flank of the shield volcano and count the superposed impact craters there (Figure 16b). During the crater counting investigations, special care has been taken to eliminate contamination by secondary impact craters and endogenous pits according to their morphologic characteristics (e.g., Head & Wilson, 2017; Oberbeck & Morrison, 1974; Shoemaker, 1962). The crater counting results are mapped in Figures 16a and 16b and reported in the standard cumulative SFD plots (Figure 16c) and tabular form (Table 1).

We identify 542 impact craters ≥10 m in diameter on the Ina mounds, which is more than twice the number (i.e., 232) reported by Braden et al. (2014). The cumulative SFD of these mound impact craters (Figure 16c) does not show clear evidence of a crater population in the equilibrium state (e.g., Xiao & Werner, 2015). Fitting of these mound impact craters using the Neukum lunar CF and PF produces an absolute model age of 59 ± 3 Ma, compared with 33.2 ± 2 Ma of Braden et al. (2014). For the floor units, 378 impact craters ≥10 m in diameter are counted, ~30% less than on the mounds with an identical surface area. The cumulative SFD demonstrates that the floor craters are almost indistinguishable from the mound craters, while subtle discrepancies are also observed: (1) for craters ≤~14 m, the cumulative crater density on the mounds is slightly higher than that on the floor; (2) for craters ~14 to ~30 m in diameter, the reverse trend is observed; (3) for the ~30- to ~50-m diameter range, the cumulative crater density on the two interior units closely overlaps; and (4) for craters ≥~50 m in diameter, the floor units exceed the mounds in cumulative crater density again, though in this diameter range a very limited number of craters are counted (Table 1). Fitting of the floor craters ≥10 m in diameter yields a model age of 48 ± 2 Ma, slightly younger than that of the Ina mounds.

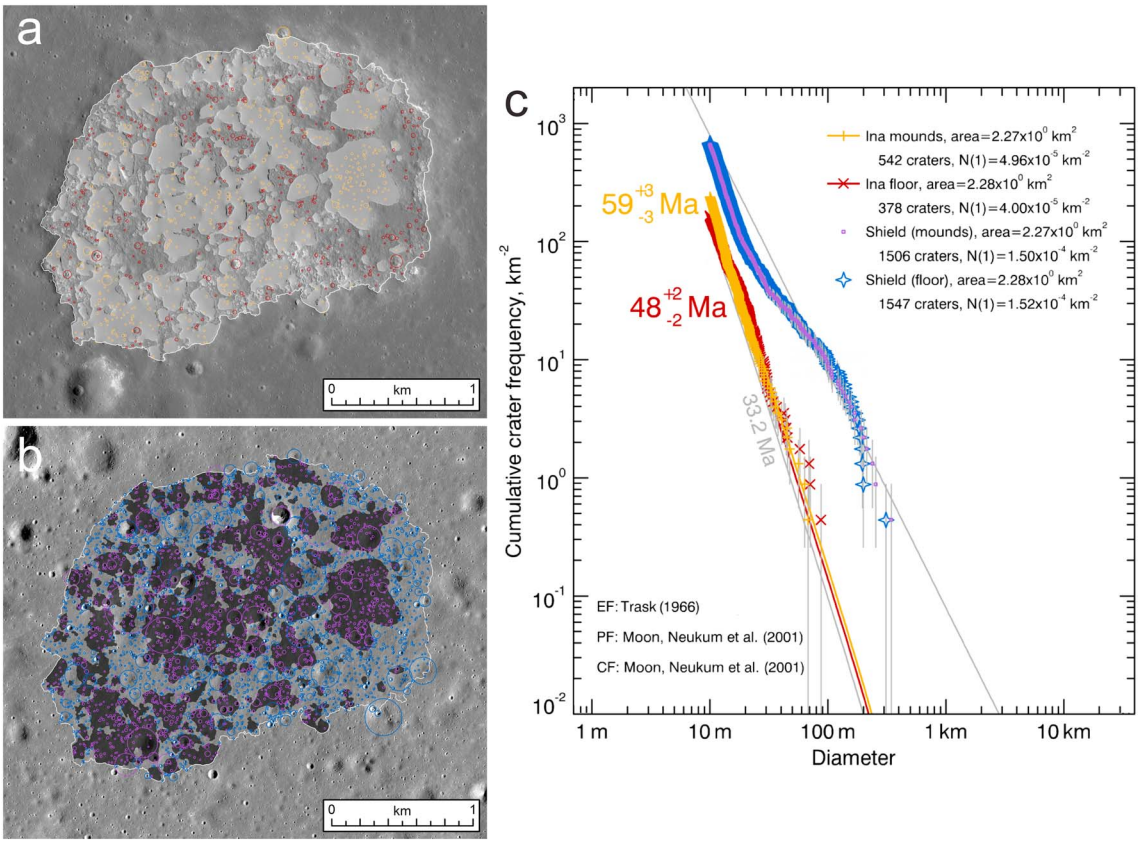


Figure 16. (a) Superposed impact craters (with rim positions marked by circles) identified on the Ina interior mounds (yellow circles) and floor terrains (red circles). The mounds are lightly masked out by gray patches, and Ina interior floor is outlined by the white polygon. The background image is a portion of LROC NAC frame M119815703. (b) Spatial distribution of the counted impact craters on the surface region (delineated by white line) on the shield flank surrounding Ina, with the same area and shape as the Ina interior (see its location in Figure S1a). The patches with the same areas and shapes with Ina interior mounds are marked by darker color. Craters superposed on the areas with same shapes with Ina mounds and floor units are marked by violet and blues circles, respectively. Background image is a portion of LROC NAC frame M1138873574. (c) Cumulative size-frequency distribution of impact craters superposed on the Ina interior mounds (yellow crosses) and floor units (red multiplication signs), and surrounding shield mare regions with same areas and shapes of the interior units (mounds: violet dots, floor: blue stars, Figure 16b). The fitting of the model age is based on the Neukum lunar PF and CF, using the CraterStats software package (Michael et al., 2016; Michael & Neukum, 2010). The gray line on the right is the lunar equilibrium function (EF) curve from Trask (1966), and the left one is the 33.2-Ma isochron reported by Braden et al. (2014).

Compared with the surrounding ancient shield volcano flank (Table 1 and Figure 16c), the Ina interior records much fewer superposed impact craters, especially for craters in the greater diameter ranges: for craters ≤20 m, the crater density in the Ina interior is generally about one fourth to one third of that of the surrounding shield, while for craters ≥20 m, the Ina interior crater density is less than one fifth of the outside mare shield surface density. We also note that the crater population of the surrounding shield is in equilibrium for diameters ≤~220 m (section 2.2), which indicates that the observable impact crater record is incomplete rather than representing what actually accumulated.

The Ina mounds are characterized by a wide range of surface slopes (Figure 6c). We also investigate the potential effect of topographic slopes on the observed surface impact crater density at variable diameter ranges. Several patchy areas with representative topographic slopes (<3°, 3–6° and >6°, derived from NAC DTM; Figure S15) were selected from the relatively areally extensive Ina mounds, and their superposed impact crater SFDs are plotted as standard *R* values at three diameter bins (Figure 17 and Table S2; calculated using the technique recommended by the Crater Analysis Techniques Working Group (1979)) and compared with the surrounding shield flank (patches with same areas and shapes as the Ina mounds shown in Figure 16b). The results clearly show a correlation between crater densities and topographic slopes: (1) the crater density generally decreases with increasing slopes, implying smaller craters on steeper sloped surface are relatively poorly preserved, probably due to being destroyed by surface

Table 1
Statistics of Numbers (#) of Impact Crater Counts With Several Diameter (D) Ranges on the Ina Interior Mounds (Figure 16a) and Floor Units (Figure 16a), and Surrounding Shield Volcano Surface Regions With the Same Areas and Shapes as Ina Interior Units (Figure 16b)

Count area	Size of counting area (km^2)	# of craters $D \geq 10$ m	# of craters $D \geq 25$ m	# of craters $D \geq 50$ m
Ina mounds	2.27	542	25	3
Ina floor	2.28	378	32	4
Surrounding *mounds*	2.27	1506	135	50
Surrounding *floor*	2.28	1547	139	55

degradation processes, for instance, regolith creep process (Xiao et al., 2013); (2) relatively larger craters show relatively less reduction of crater densities, or even slightly increased crater density on steeper slopes, suggesting larger craters are probably more resistant to slope erasure effect; (3) the surrounding ancient shield region (3.1 ± 2.7° slope) exhibits a significantly higher crater density than Ina interior mound portions with comparable slopes.

The multiple annular terrace pattern of the Ina interior floor, with decreasing elevations toward the central portion (Figures 6a and S14), suggests potential multiphase emplacement/modification processes (section 3.4), which may have an effect on the preserved impact crater populations. To explore this issue, we compare the SFD of impact craters superposed on the three floor annuli (Figure S16). It shows (1) the innermost annulus (Annulus 3) has a relatively higher cumulative crater density than the outer two annuli for craters ≤~18 m in diameter; (2) the outermost annulus (Annulus 1) has a comparable cumulative crater density to the middle annulus (Annulus 2) for craters ≤~13.5 m in diameter and shows a slightly elevated cumulative crater density at greater diameters and reaches a comparable level with the innermost annulus; (3) at the ≥~25-m diameter range, the cumulative crater SFD of the three annuli closely overlaps. Our formation model suggests that the multiple annuli of the Ina floor were formed contemporaneously (section 4.1), and the floor generally has a very flat slope (so no obvious slope effect), and the superposed impact crater SFD are predicted to be comparable, as observed here.

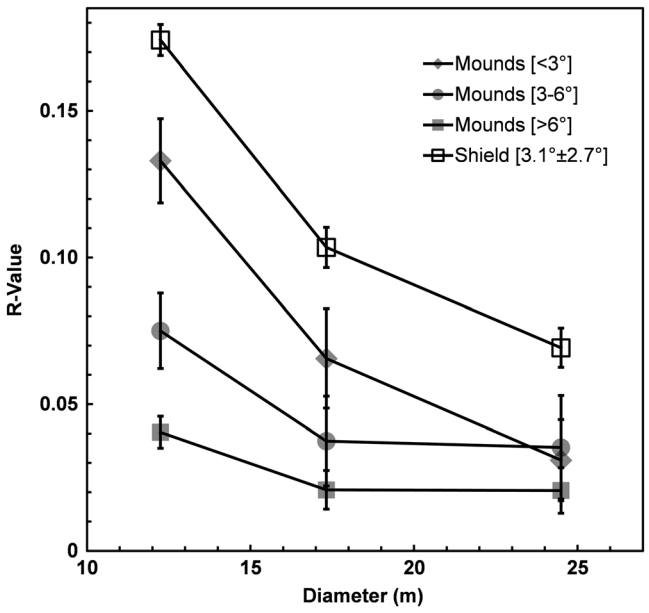


Figure 17. Plot of crater size-frequency distribution (*R* values calculated based on Crater Analysis Techniques Working Group, 1979) with several diameter ranges (10–15, 15–20, and 20–30 m) for representatively sloped areas on Ina mounds outlined in Figure S15 and surrounding shield volcano surface marked by dark patches in Figure 16b. See Table S2 for the specific values.

3.12. Floor Topography and Slopes

We use the NAC DTM-derived slope map (Figure 6c, 2 m pixel size, with a baseline of 6 m) to characterize the topographic slopes of the interior of Ina and associated geomorphologic units (details can be found in Text S2 and Figures S17–19 in the supporting information). Slope-frequency distribution investigations show the mounds and hummocky units have similar most-frequent slopes (2–5°) to the entire Ina interior; the mounds, however, have many more (areal percentage) areas with slopes over>7° than the hummocky units. We suggest that this can be explained by the slope baseline effect: most of the surface reliefs of the hummocky units are shorter than the slope baseline (6 m), while the convex upward profile, relatively extensive (commonly wider than ~10 m), steep marginal scarps of the mounds can significantly elevate their average slope. The blocky units and the moats have relatively clustered most-frequent slopes (3–4°), while the moats have more areas with slopes steeper than 8°; this can be again caused by the slope baseline effect.

3.13. Regolith Thickness

Small fresh impact craters on the lunar surface have been observed to develop variable interior structures ranging from normal bowl-shaped craters to abnormal craters with special interior structures (e.g., concentric ring, flat bottom, and central mound). These crater interior morphology variations are interpreted to represent meteoritic

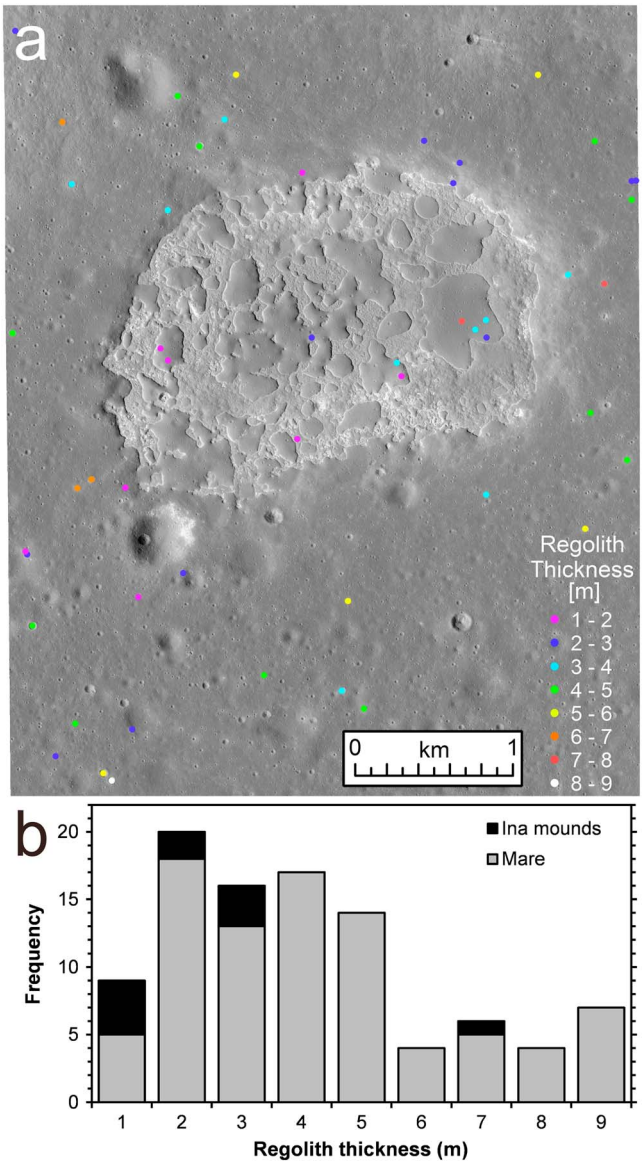


Figure 18. (a) Regolith thickness of the Ina interior mounds and the surrounding shield area determined from crater interior morphology and diameters on LROC NAC frame M119815703 and (b) their histogram.

impacts into layered targets with an unconsolidated surface layer (commonly lunar regolith) underlain by a more cohesive substrate (e.g., basaltic bedrock). The morphology and size of the craters are correlated with the contrast between crater diameter and the thickness of the surface unconsolidated materials (e.g., Oberbeck & Quaide, 1967). Measurements of the rim-to-rim diameter and size of the interior structure of these abnormal craters provide a quantitative method to estimate the surface regolith thickness for typical lunar mare regolith surfaces (see the methodology in Bart, 2014). For the shield volcano flank surrounding the Ina pit crater, 87 abnormal craters are identified and measured, which give a median regolith thickness of 4.8 m (ranging from 1.3 to 11.0 m with $1\sigma = 2.3$ m, Figure 18). For the Ina mounds, we identify 10 such abnormal craters and obtain an estimated median regolith thickness of 2.1 m (ranging from 1.0 to 7.6 m with $1\sigma = 2.0$ m). Within one of the largest Ina mounds (Mons Agnes), the estimated regolith thickness shows a trend of becoming thin toward the margins (four abnormal crater measurements), accompanied by increased topographic slopes. We note that this regolith thickness estimation method is based on the assumption of impacts into a typical mare regolith target; impacts into highly porous targets, as suggested by Wilson and Head (2017b) and Qiao et al. (2017) for the Ina mounds, may introduce a different cratering manifestation. For example, these abnormal craters may represent impacts into a different set of layered targets other than typical basalt-mare targets, for instance, the hypothesized magmatic foam extrusions superposed on a solidified lava lake crust (Qiao et al., 2017, section 4.1); in these cases, these crater may have penetrated about the depth of the mound height and sampled the underlying bedrock, and the calculated thickness may be related to the magmatic foam thickness.

Blocky craters, that is, craters with exposed blocky materials within the crater interior and/or in the surrounding exterior, provide another method to constrain the surface regolith thickness: the excavation depth of these blocky craters should exceed the surface regolith thickness. Several blocky craters as small as ~20 m are observed on the Ina floor terrains; thus, the floor surface regolith materials can be constrained to be thinner than the excavation depth of these craters, that is, ~1.7 m (see section 3.10 and Figures 15g and 15h). Moreover, no confirmed blocky craters have been observed on the Ina mounds (see section 3.10). Our estimation of the surface regolith thickness of Ina interior is consistent with the 10–15 cm lower limit value reported by LRO Diviner thermophysical measurements (Elder et al., 2016, 2017).

3.14. Optical Reflectivity and Maturity

One of the most enigmatic characteristics of Ina pit crater is its anomalously high reflectivity and optical immaturity, especially for the interior floor rubble materials (Bennett et al., 2015; Garry et al., 2013; Schultz et al., 2006; Staid et al., 2011; Strain & El-Baz, 1980). To explore the nature and potential origin of these uncommon optical properties, we here present an updated characterization of the reflectance of Ina and its adjacent area at 750 nm, and their optical maturity (OMAT) using the high-resolution imaging spectrometer data obtained by the Kaguya Multiband Imager (Figures 19 and 20 and Table S3; details can be found in Text S3 in the supporting information). Reflectance mapping shows that (1) the Ina mounds have comparable (or slightly elevated) visible reflectance to the surrounding mare, (2) the floor blocky materials are much more reflective (Figure 19a and Table S3), and (3) the Ina floor hummocky units show apparent reflectance variations: areally extensive hummocky terrains at the eastern marginal floor with abnormally low 750-nm reflectance and other smaller hummocky units with relatively elevated reflectance (Garry et al., 2013; Figure 19 and Table S3); these brightness variations are probably due to occurrence of

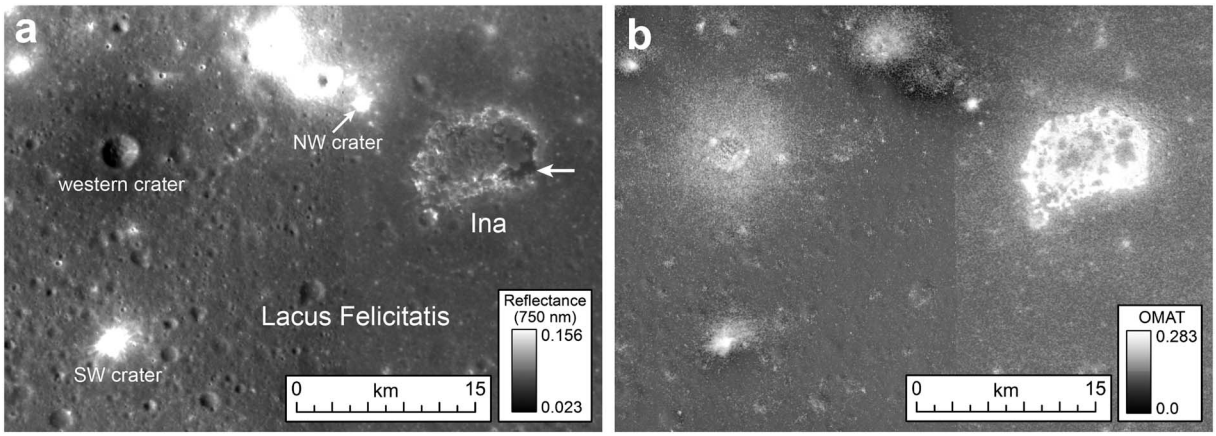


Figure 19. Kaguya MI (a) 750-nm reflectance and (b) optical maturity maps of Ina and the surrounding region. The thicker arrow at the right edge in Figure 19a indicates the darker portion of the Ina floor hummocky units.

(subresolution) blocky materials. OMAT investigations (Figure 19b and Table S3) reveal that the entire Ina interior is generally optically more immature than the surrounding mare, while displaying noticeable differences in various interior terrains: (1) the mounds are slightly more immature than the surrounding mare shield; (2) the blocky units are the most immature materials in the local regions within and surrounding Ina; (3) hummocky units have OMAT measurements between those of the Ina mounds and the blocky units; and (4) the two different subtypes of hummocky units (*dark* and *bright*) exhibit indistinguishable OMAT values, suggesting they may have been emplaced contemporaneously. Spectroscopic analysis (Figure 20) shows (1) the Ina interior is mainly composed of high-titanium basalt; (2) the brighter portion of the Ina hummocky units shares similar optical alteration path with Ina mounds while may have been subject to different optical maturation processes from the blocky units and the darker hummocky units.

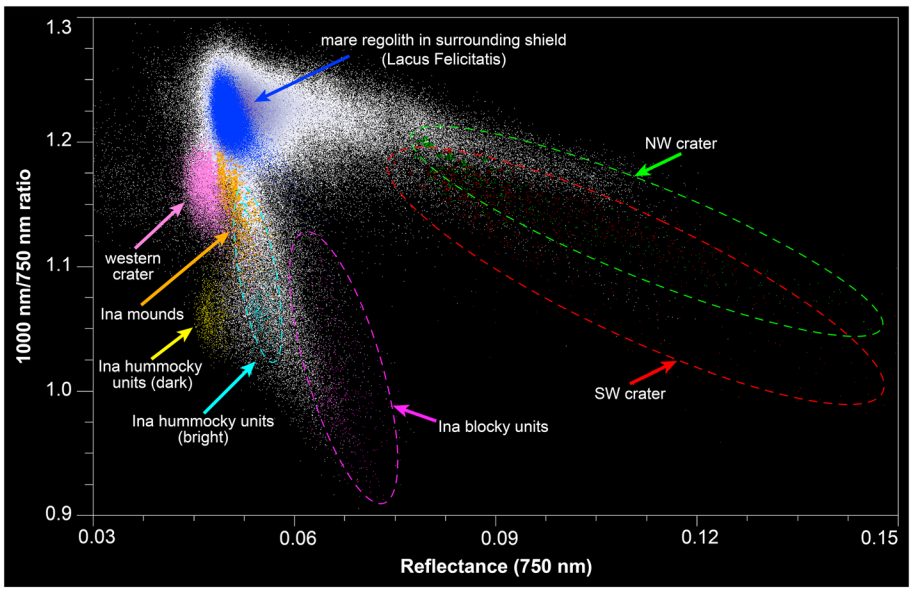


Figure 20. The 2D scatterplot of Kaguya MI 1000/750-nm reflectance ratio, as an indicator of the 1-μm mafic absorption band strength, against 750-nm reflectance. Multiple surface features within and surrounding Ina are plotted with differently colored data points, and their values are cataloged in Table S3.

4. Discussion

4.1. Interpreted Formation Mechanism of Ina Shield Volcano Summit Pit Crater

On the basis of (1) our latest physical volcanology analysis of lunar dike evolution processes and final-stage shield-building eruptions (Head & Wilson, 2017; Wilson & Head, 2017a); (2) analog studies of the morphology, topography, and magmatic-volcanic processes of terrestrial small shield volcanoes in Hawai'i (Qiao et al., 2017, Figure 21); and (3) following our comprehensive geological characterization of the context and interior of Ina pit crater presented above (sections 2 and 3) and prior investigations (e.g., Braden et al., 2014; Garry et al., 2012; Qiao et al., 2017; Strain & El-Baz, 1980), we examine the Ina feature in the context of lunar shield-building eruptions. We begin with the crucial observation and interpretation that the Ina feature is a summit pit crater/vent atop an ~22-km-diameter, ~3.5-Ga-old shield volcano (Qiao et al., 2017; Strain & El-Baz, 1980) and then examine the successive phases of a lunar shield-building eruptions (Wilson & Head, 2017b), with a special focus on final-stage summit pit crater activities. We interpret the wide range of characteristics associated with the Ina feature as being consistent with a two-component model of origin as a partially drained summit pit crater lava lake atop an ancient shield volcano (*hummocky floor model*), accompanied by the waning-stage extrusion of highly gas rich magmatic foam materials (*mound foam model*, Qiao et al., 2017; Wilson & Head, 2017b).

New theoretical and observational treatments of lunar magmatic-volcanic and gas production processes (Rutherford et al., 2017; Wilson & Head, 2018) provide important evidence that lunar small shield volcanoes, like the one containing the Ina pit crater, are formed through eruptions fed by a single dike sourced deep in the upper mantle. Wilson and Head (2018) synthesized recent developments in understanding the origins and volatile contents of lunar magmas, the mechanisms that transferred magma to the surface, and the factors that controlled the eruption style of the resulting volcanism, with emphasis on the effects of volatile formation and release. Assessment of mare basalt gas release patterns during individual eruptions (Rutherford et al., 2017) provides the basis for predicting the effect of vesiculation processes on the structure and morphology of associated features. Using these data, Wilson and Head (2018) subdivided typical lunar eruptions into four phases: *Phase 1*, dike penetrates to the surface, transient gas release phase; *Phase 2*, dike base still rising, high flux Hawaiian eruptive phase; *Phase 3*, dike equilibration, lower flux Hawaiian to Strombolian transition phase; and *Phase 4*, dike closing, Strombolian vesicular flow phase. They showed how these four phases of mare basalt volatile release, together with total dike volumes, initial magma volatile content, vent configuration and magma discharge rate, can help relate the wide range of apparently disparate lunar volcanic features to a common set of eruption processes and help place small shield volcanoes and their summit pit craters into this context. Specifically, Wilson and Head (2018) showed that small shield volcanoes can consist of Phase 2 lavas erupted from dikes that have a relatively small volume, so that neither the erupted volume nor the volume flux is large. Overflows from the lava lake around the vent are fed at a low eruption volume flux; the resulting lava flows travel ~5–15 km before stopping due to cooling, successively forming the shield. Subsequent Phase 3/4 activity builds additional features at the summit of the volcano, including summit pit craters. Summit pit craters and lava lakes may also be the result of Phase 4a activity in the latter stages of typical eruptions; as the rise rate wanes and volatile exsolution is optimized, very vesicular magma from the dike is emplaced under a cooling crust on the lava lake above the vent.

In summary, shield-building eruptions are predicted to occur when the magma volume flux in the upwelling dike is sufficient to penetrate to the surface, while still too low to cause typical mare basin-filling eruptions (Wilson & Head, 2017a), or at the end, in the waning stages of the fourth phase of the typical eruption sequence (Wilson & Head, 2018). In the course of the dike approaching the surface, volatile phases within the magma would continuously exsolve due to pressure release, generating abundant gas bubbles (mainly CO and H_2O; Figure S20a). Expansion of the bubble-rich magma into the lunar hard vacuum would ensure that the Ina shield-building eruptions began with vigorous fountain activities, ejecting abundant pyroclastics beyond the vent (Figure S20b); some of them would deposit on a growing crater rim surrounding the vent, in a similar style with many terrestrial eruptions, for instance, the 1961 effusive eruptions at the Halema'uma'u crater (Dzurisin et al., 1984; Richter et al., 1964).

The building of the small Ina shield volcano is dominated by the accumulation of low-effusion rate, cooling-limited flows (Figure S20c). The measured size, height, and estimated ~0.6 km^3 volume of the Ina shield volcano are at the upper end of values for more than 300 small mare shields identified on the Moon

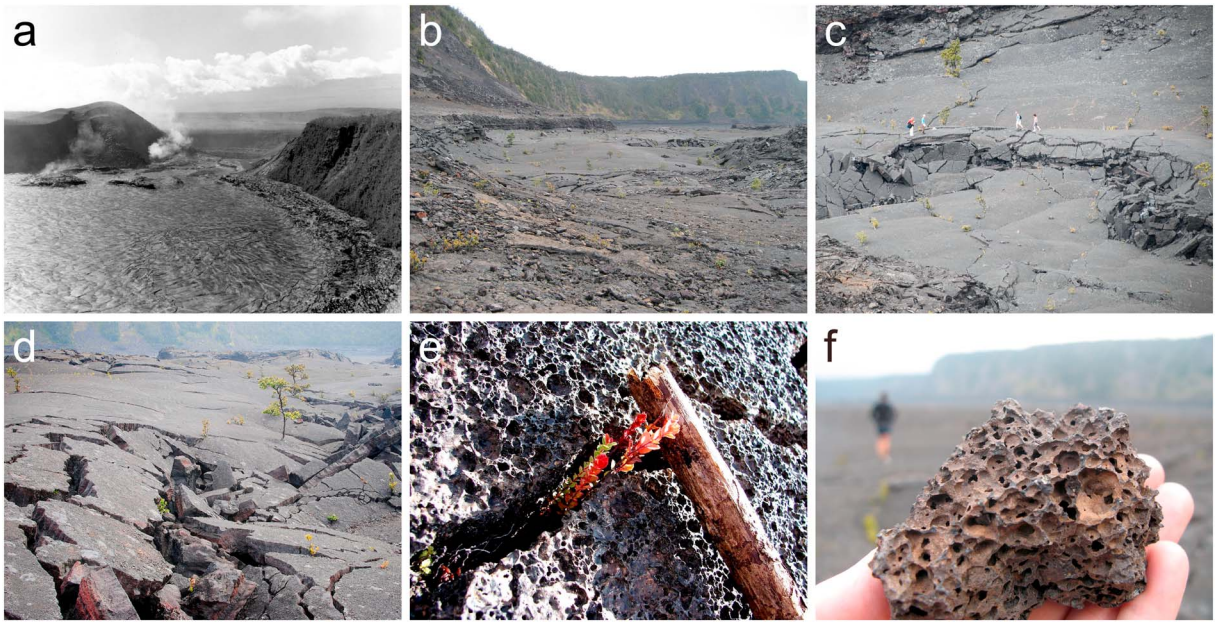


Figure 21. Kīlauea Iki summit pit crater/vent on the Kīlauea shield volcano, Hawai'i. (a) The third phase of activity in Kīlauea Iki crater during the 1959 Kīlauea eruption. Note that the chilled ledge (right), ~15- to 60-m wide and approximately 15-m high, surrounds the entire lava lake. The vent at the base of Pu'u Pua'i cone and the largest island (upper left) continues to emit fumes. View is from Byron Ledge overlook after activity ceased. U.S. Geological Survey photo rdh00079 taken on 2 December 1959. (b) Northwest edge of the Kīlauea Iki crater floor. Note the elevated marginal ledge formation and the highly fractured crater floor crust. Photo by Scott Carpenter on 10 February 2009 (www.flickr.com/photos/scarpenter/3300718818/). (c) West floor of Kīlauea Iki crater, near the Pu'u Pua'i cone. Note the draped plate at the edge of preeruption topography (top), the chilled marginal terrace, and the pressure ridge (center with hikers on top) formed by deformation of the subsiding rigid crustal layer on top of the lava lake. Note the evidence for abundant void space associated with these deformed plates. U.S. National Park Service photo taken on 11 November 2010. (d) The deformed, fractured, and macrovesicular nature of the lava lake crust present at the west Kīlauea Iki crater floor. Photo by Harry Chen on 26 November 2011 (www.flickr.com/photos/harrychen/6434789769/). (e) A close look at the Kīlauea Iki lava lake crust floor. Note the abundant small vesicles and the several centimeters-long plants for scale. Photo by Jenny Levine on 8 November 2007 (www.flickr.com/photos/shifted/2044399797/). (f) A sample of the crater floor plate, showing the highly microvesicularity property. Photo by Chris McGillicuddy on 27 November 2011 (www.flickr.com/photos/mcg/6412143341/).

(Head & Gifford, 1980; Tye & Head, 2013), indicating that it is formed by relatively longer flows (up to ~12 km) through lengthy eruptions. On the basis of the topographic slopes of the Ina shield flanks (averagely ~1.7°) and observations of southwestern Imbrium flows (Schaber et al., 1976), the thickness of individual flows can be estimated as ~1 m. Assuming an ~1–2 km width of individual flows, calculations based on the parameter relation for channelized flows (Wilson & Head, 2017a) yields an estimated magma extrusion volume flux of ~225–450 m^3/s. Thus, the building of the Ina small shield is predicted to have operated over a period of ~3–6 months (assuming an uninterrupted emplacement activity). Spectroscopic examination of shield deposits excavated by fresh small craters indicates that the erupted magma shows inhomogeneities in titanium abundance (section 2.1 and Figure 2d): flows emplaced earlier are more titanium rich than the last flows deposited on the surface.

The final stages of a small shield-building eruption are characterized by a series of important summit pit activities, significantly different from normal mare basalt flow eruptions (Head & Wilson, 2017; Wilson & Head, 2017b). As observed in the late stages of terrestrial shield-building eruptions, fountain activities at the Ina shield volcano diminished gradually; decrease in magma rise rate would allow gas bubble production and rise, bubble coalescence, and the onset of a Strombolian phase of activity in the pit crater lava pond. Cycles of lava drainage and refilling, along with gas-piston activities, caused the lava lake surface to fluctuate frequently. During the waning part of this period, the lava lake surface began to cool and solidify, developing a platy, meters-thick solidified crust forming the thermal boundary layer (TBL) of the summit pit crater lava lake. Cooling of the lava lake is predicted to be more efficient in the shallower marginal parts of the lake in contact with the relatively chilled surroundings and less efficient over the deeper part above the source vent. During lava lake inflation and deflation cycles, the magma continuously degassed, Strombolian ejecta was emplaced on the cooling lava lake crust, and bubbles and foams accumulated below the lava pond crust;

during the deflation episodes, the lava lake crust foundered and tilted toward the interior multiple times, generating multiple terrace patterns within the lava crust. The relatively chilled marginal portion of the crust, welded to the crater wall, became very brittle. During crust subsidence, the tensile stress operating on the marginal crust would cause it to fracture and separate from the central part of the lava crust, leaving steep-sided ledge structures at the base of pit crater wall. Also during the lava lake deflation, the surface crust was locally cracked and deformed into small polygonal plates and pressure ridges. Lava and magmatic foams oozed from these surface cracks, flowed sluggishly on the crust surface and covered previous pressure ridges and cones, leaving them as isolated islands/hummocks (kipukas). In the waning eruption stage, the lava lake became increasingly stagnant; the dominant activities were sporadic small Strombolian and related gas release events forming pits and linear fissures.

On the basis of the nature of the lava lake crust development and lava drainage and crust deflation, we would expect significant void space to exist below the pristine surface of the deflated and draped crust. Thermal calculations show that a 1-m-thick boundary layer will develop on a lunar lava lake within the first 4 days, growing to a 2-m-thick crust in less than a month (Wilson & Head, 2017a), periods of time well within the observed duration of lava lake formation and drainage in terrestrial shield pit craters. These thicknesses are more than sufficient to cause local bending and breaking of the crust upon lake drainage to produce pressure ridges of tilted and imbricated plates, as well as roofs and arches over drained subsurface lava tubes (Wilson & Head, 2017b). More importantly, all these complex activities during the lava lake process, including lava drainage, inflation and deflation, squeeze-ups, sporadic gas venting, and volume decrease due to thermal contraction and solidification, would together make the lava lake floor highly porous, containing abundant macrovesicularity and microvesicularity and open void spaces. Indeed, this is seen in surface investigations of and drill cores from the Kīlauea Iki lava lake floor: 10–40% vesicles were observed in the upper 10 m of lava lake crust (Figure 21, Richter & Moore, 1966; Mangan & Helz, 1986), and vesicles were likely to be considerably larger in the lunar environment (Head & Wilson, 2017). For a lava lake of ~30-m thickness, these processes could readily produce at least 10–20% subcrustal void space.

In the latest stage of the shield-building volcanic process, the overpressure in the dike has been finally exhausted and no more magma will ascend; this marks the ending of the shield-building activity and the transition of eruption style toward a Strombolian explosive phase (Wilson & Head, 2017b, Figure S20d) with minor explosions through the lake surface above the widest part of the dike. The final volatile production at shallow depths is dominated by the release of water vapor, with bubbles rising buoyantly and accumulating at the tip of the magma column, just below the TBL (Wilson & Head, 2017b, Figure S20e). The typical water content (several hundred parts per million) for lunar basaltic magma (Hauri et al., 2015, 2011; Saal et al., 2008), combined with the near-zero magma ascent rate and the likely high bubble number density from abundant nucleation sites, would ensure that these gas bubbles are so small (~20-μm radius, Wilson & Head, 2017b) that the surface tension forces allow them to remain stable against the internal gas pressures and so to form a stable magmatic foam layer. This foam layer can extend several hundred meters downward and reach an extreme vesicularity up to ~95% (Qiao et al., 2017; Wilson & Head, 2017b). The final stages of dike stress relaxation and closure would squeeze the magmatic foams upward very slowly (~10 mm/s), causing them to extrude to the surface through cracks in the TBL to produce the bleb-like mounds (Qiao et al., 2017; Wilson & Head, 2017b, Figures S20f and S21).

The availability of high-resolution topographic and imaging data from LROC NAC permits the rheological modeling of the emplacement of magmatic foam lavas, which shows that magmatic foam extrusion proceeds at a very low effusion rate (~0.6 m^3/s), with the majority of the Ina mounds being emplaced over a period of several hours to several days (Wilson & Head, 2017b). The unusually high foam viscosity and low-effusion rate would inhibit the lateral motion of foam lava flows, enhancing their convex shapes and steep edges, in a similar style to the building of highly silicic domes on the Earth and the Moon (e.g., Wilson & Head, 2003). The final-stage of dike closure would involve solidification of magma against the dike walls and consequent shrinkage, resulting in drainage of residual lava from the bottom of the lake, deformation of the lava lake crust, and final floor subsidence. Mass load of magmatic foam extrusions and the large void spaces left underlying the lava lake crust due to magma foam extrusion enhance the deformation and subsidence of the adjacent local lava lake crust (see the detailed crust subsidence mechanism in Wilson & Head, 2017b), further ensuring the steep sides of the mounds and generating topographic moats around the mound margins (Qiao et al., 2017, Figure S21). Occasionally, the vertical displacement of local lake

crust subsidence may exceed the building height of the extruded foamy mounds, which, consequently, generates the observed low mounds (section 3.2). Topographic and morphometric characterizations of all the low mounds ($n = 6$) show that the vertical displacement of local lake crust is generally less than ~1–2 m and can be as deep as ~10 m at the largest *low mound* (Figure 9). Though occurrence of these low mounds is much less frequent than the common raised mounds, it is very likely that local lava lake crust subsidence due to upward extrusion of foamy magma would be an important process, which would in part account for the inward lowering of the Ina floor topography (section 3.4). It is predicted that gas bubbles in the top of the emplaced foam will explode in the hard vacuum, producing a layer of low-density (compared to basaltic lava flows), very fine regolith. The mass loading of these surface regolith and radiative cooling of the foam lava flows will protect the extruded foamy lava from further disruption.

The interpreted magmatic foam substrate of Ina floor mounds is supported by a line of observations: (1) the unusual morphologies of superposed impact craters, including general nonblocky crater interior and no associated radial ray patterns (section 3.10), (2) much lower density of superposed impact craters compared with the surrounding mare (interpreted to be due to the crater diameter decrease effect of impact into a highly porous target, section 3.11), and (3) Diviner thermophysical mapping results, which show that Ina mound materials are less consolidated or contain fewer small rock fragments than typical mare regolith (Elder et al., 2017).

Thus, in this waning-stage two-component, lava lake process and magmatic foam extrusion, scenario (Qiao et al., 2017), the various terrains associated with Ina are interpreted to have formed in the terminal phases of the shield-building activity (Wilson & Head, 2017b, Figure S20), contemporaneous with the adjacent mare basalt lava eruptive phase more than three billion years ago. The narrow collar surrounding Ina (section 3.1 and Figure 3 in Garry et al., 2012) is interpreted to be the remnant of lava lake filling and overflow, together with possible pyroclastics. The basal terrace/ledge and steep inward facing scarp at the base of the interior walls of Ina (section 3.3) are analogous to the chilled margin of a lava lake remaining after lava lake deflation and/or recession, which are embayed and overridden by subsequent magmatic foam extrusions near the floor edge. The topographically low floor terrains (section 3.5 and Figure 13) are analogous to the solidified lava lake crust, and each of their complex topographic and morphologic characteristics corresponds to the various activities operating during the lava lake process: (1) the three-stage annular, inwardly lower topography of the floor (section 3.4) is interpreted to be formed through lava lake crust foundering and tilting toward the interior portion during the final magma retreat, lava lake deflation episodes, and subsequent upward extrusion of foamy magma; (2) the hummocky textures (section 3.5 and Figure 13) are analogous to lava lake inflation, lake crust flexure, bending, fracturing, and ridge formation; (3) the abundant pits (section 3.7) are analogous to degassing pits (enhanced by the lunar vacuum), late-stage sporadic lava fountains, and subsequent regolith drainage through infiltration pits into porous macrovesicular lava lake crust and void space below; (4) the linear depressions/fractures (sections 3.6 and 3.7) are interpreted to be modified cracks in the lava lake surface formed by flexure, cooling, and shrinkage during lava lake deflation and deformation; (5) the polygonal patterns are analogous to highly deformed and cracked lava lake crust; (6) the vermicular patterns (section 3.5 and Figure 13) are analogous to tilted lava lake crust; (7) ridged textures are interpreted to be locally deformed lava lake surface crust; and (8) the floor blocky units (section 3.9) are analogous to exposed blocks of the solidified lava lake crust (either exposed instantaneously or subsequently by subsequent meteoritic impacts and regolith infiltration). In addition, the various morphologies from these complicated lava lake activities often intricately interweaved, producing the highly diversified surface textures of the Ina floor terrains (section 3.5 and Figure 13). The bleb-like mounds (section 3.2) are interpreted to be the solidified magmatic foam extrusions, and the topographically lower moats surrounding the mounds (section 3.8) are formed through the subsidence of local lava lake crust to conserve volume. The several low mounds (section 3.2) are interpreted to be explained by the much greater vertical displacement of the local crust during subsidence, which exceeds the height of the extruded mounds, making it lower than the preemplacement lava lake crust floor. The preferential occurrences of mounds at the contacts between floor annular terraces are interpreted as the extrusion of magmatic foam through the lava lake crust fractures caused by its inward subsidence. These interpretations and predictions can be tested with future observations, measurements, and missions (see section 5).

The final stage of formation of lunar shield volcanoes, summit pit craters, and lava lakes involves cooling and solidification processes. As magma supply wanes and dike closure processes reach equilibrium

(Wilson & Head, 2018), any remaining advective magmatic heat in the dike or lava lake is transferred by conduction to the surrounding country rocks over geologically rapid timescales (~10^2–10^3 years, Hardee, 1980; Wilson & Head, 1981, 2017a, 2018; Richter & Moore, 1966; Wright et al., 1976). Subsequent, separate dike intrusion events from the same very deep diapiric magmatic source region are possible during the source region lifetime (Wilson & Head, 2017a). However, (1) the repose time between eruptions is predicted to be much longer than the cooling time of the initial dike (Wilson & Head, 2017a), and (2) a second dike propagated from the same source at several hundred kilometers depth is very unlikely to reach the surface at exactly the same ~2 × 3-km location as the Ina summit pit crater; in fact the solidification of the dike is predicted to change the local stress field sufficiently that it virtually precludes the reoccupation of the Ina summit pit crater by a later dike (Head & Wilson, 2017). These same considerations place severe constraints on the likelihood of a dike originating from the lunar mantle over three billion years later (<100 Ma ago) and erupting in the exact position of the very small (~2–3 km) Ina summit pit crater on an ancient shield volcano.

Once the lava lake has solidified, how will the unique eruption products, formed during the waning stage of shield-building activity (i.e., subsided macrovesicular and microvesicular lava lake crust superposed by numerous solidified magmatic foam extrusions), respond to the subsequent, billions of years of continuous geologic modification by regolith forming bombardment processes?

4.2. Postemplacement Geologic Modifications

Our two-component model for Ina formation is predicted to have occurred more than 3 Ga ago, contemporaneous with the adjacent mare deposit emplacement. Subsequent to this time, geological modification process, including impact cratering, optical maturation, regolith development and topographic degradation, should have operated on all surfaces equally (mare, shield, and Ina mounds and hummocky/blocky terrains). How can the geomorphological crispness, optical immaturity, and anomalously young crater retention ages of the Ina interior be explained? The unique substrate nature of the Ina interior, solidified magmatic foam mounds with bulk porosity up to ~95% and chilled lava lake crust floor with abundant microvesicularity and large void space, provides an insight.

4.2.1. Impact Cratering

Meteoritic impact is arguably the most important geological modification process on the Moon, continuously operating everywhere on the lunar surface. On typical mare surfaces including the flanks of Ina shield volcano (solid basaltic lava flows), when a meteoritic impactor strikes the lunar surface substrate, its kinetic energy is focused on deforming, fracturing, comminuting, excavating, and ejecting the target materials, leading to the formation of well-developed, bowl-shaped, relatively shallow, blocky craters, with lateral blocky ejecta deposited several radii outward and finer particles ejected further (Wilson & Head, 2017b, Figure S22a). Impacts into the microvesicular and macrovesicular Ina lava lake crust floor, however, are predicted to operate dominantly through the compaction and crushing of the substrate, which is extremely porous at diverse scales, disruption of vesicle walls, and excavation of the blocky portions of the crust substrate (Qiao et al., 2017; Wilson & Head, 2017b, Figure S22b). As the chilled lake crust floor already consists of abundant large (decimeter to meter scales) open void spaces, a large portion of the impact crushed and excavated substrate debris will preferentially sift into the abundant substrate macrovesicularity. This infiltration process is assisted by continual seismic shaking activities caused by the multiple subsequent impacts. In consequence, craters on the Ina hummocky floor are poorly developed, filled with crushed rubble, abnormally shaped, difficult to identify and degrade rapidly, and show a deficit of larger craters; lateral ejecta emplacement is highly inhibited; continuous sifting into the porous substrate enhances the volume loss of surface particles and exposure of subsurface blocks (Figure S22b, Wilson & Head, 2017b).

Impacts into the solid magmatic foam of the Ina mounds are proposed to proceed by a different mechanism (Qiao et al., 2017; Wilson & Head, 2017b; Figure S22c). The Ina mounds are composed of abundant tiny vesicles with an extremely high porosity, up to ~95%. Kinetic energy of the meteoritic impacts will mainly be consumed in permanent compressing, crushing, shattering, and penetrating the foam vesicles (the aerogel effect, Wilson & Head, 2017b; Figure S23), and impact-induced shock waves tend to decay much faster; both factors lead to a significant reduction of cratering efficiency. Under these circumstances, typical cratering processes are largely obstructed, and the resultant craters are nonblocky, poorly preserved and easily degraded (Wilson & Head, 2017b, Figure S22c). Excavated materials are ejected at much lower

velocities and higher ejection angles, so that a minimum amount of materials would be ejected beyond the crater interior. As solid foam is very weakly resistant to projectile penetration, craters tend to be much smaller in diameter and deeper than a similar impact into solid basalt or typical regolith (Figures S23a and S23b), as evidenced by numerous laboratory and numerical simulation impact experiments (e.g., Figure S23, Collins et al., 2011; Flynn et al., 2015; Hörz et al., 2000; Housen & Holsapple, 2003, 2011; Michikami et al., 2007; Schultz et al., 2002; Wünnemann et al., 2006, 2012, 2011) and spacecraft observations at highly porous asteroids (e.g., Housen et al., 1999). Such high aspect ratios will decrease rapidly due to filling with crushed materials, producing shallower depressions.

4.2.2. Space Weathering

When surface materials on an atmosphereless body, like the Moon, are exposed to the harsh space environment including interplanetary dust and micrometeorite bombardment, solar and cosmic ray irradiation, and solar wind implantation and sputtering, their physical and/or chemical properties are gradually modified; these complicated modifications are summarized as space weathering. From an optical perspective, typical lunar-style space weathering is characterized by the gradual darkening of surfaces (especially at visible and near-infrared wavelength), subduing of diagnostic absorption bands of minerals (especially iron bearing components), and reddening of spectral slopes (relatively elevated reflectance at longer wavelengths); these systematic optical alterations are collectively termed as optical maturation (Hapke, 2001; Pieters & Noble, 2016). The optical property difference between the newly exposed basaltic outcrops at small recently formed fresh craters (e.g., the NW and SW craters near Ina, Figure 19) and ancient mare deposits (e.g., those of the Ina shield volcano flank, Figure 19) is a visual demonstration of the space weathering effects (Figure 20). If the Ina interior is indeed emplaced contemporaneously with the adjacent ancient mare more than 3 Ga ago (section 4.1), could the unusual physical properties of the Ina floor and mounds also account for their observed obvious optical immaturity (Figure 19)? The extremely microvesicular Ina mounds and the popped surface magmatic foam layer are predicted to be very capable of absorbing impact-induced shock waves (Figure S22c; e.g., Housen & Holsapple, 2003). In this scenario, micrometeorite impact vaporization tends to be less efficient, and then the production of reduced submicroscopic metallic iron particles, the major optical maturation agent, is retarded; similarly, inefficient weathering processes are also observed at several asteroidal bodies with an inferred porous interior (e.g., Clark et al., 2002). In consequence, space weathering at the Ina mounds proceeds at a diminished rate, consistent with the observed relatively optical immaturity compared with the surrounding ancient shield volcano (Table S3). On the Ina lava lake crust, the continual infiltration and seismic sieving of the fine components of the developing surface weathered materials into the abundant void space below would continually expose underlying primitive, unweathered materials (Wilson & Head, 2017b, Figure S22b), thus maintaining the observed apparent optical immaturity of the floor substrate (Figure 19 and Table S3).

4.2.3. Regolith Development and Evolution

Lunar regolith development on ancient mare lava flow deposits (McKay et al., 1991) is commonly visualized as a dominantly mechanical weathering process of fragmentation and comminution of the emplaced basaltic bedrock by subsequent impactor populations and a steady stream of charged atomic particles, building up a fragmental and unconsolidated regolith layer of broken, melted, and otherwise altered debris that increases in thickness as a function of time. The formation of each successive impact crater brecciates the underlying solid basalt substrate, excavates regolith and rock materials, and spreads them laterally as ejecta, mixing with the growing regolith layer (Figure S22a). Surface regolith accumulated on ~3.5-Ga-old mare basalt flows is generally ~4–5 meters in thickness (Bart et al., 2011; McKay et al., 1991). The ongoing accumulation of surface regolith would cause the destruction and burial of surface blocky materials, leading to the very rare occurrence of boulders on a typical mature lunar surface (e.g., Bandfield et al., 2011; Basilevsky et al., 2013).

On the surrounding mare and on the flanks of the Ina shield volcano, regolith development proceeds normally so that the current regolith thickness is estimated as ~4.8 m (section 3.13). On the Ina mounds, due to the observed predominantly nonblocky impact craters and much less lateral ejecta, regolith development and maturation is highly subdued (Figure S22c), consistent with our estimated median regolith thickness of 2.1 m from blocky crater measurements (section 3.13 and Figure 18) and the interpreted 10–15 cm lower limit of regolith thickness from LRO Diviner radiometer data (Elder et al., 2016, 2017). In addition, the convex upward shape of the mounds would cause regolith to preferentially move down toward the steeper

mound flanks and then partly infiltrate into the marginal moats and underlying void space within the floor lava lake crust, becoming thinner at the margins, consistent with estimated regolith thickness at one of the largest Ina mounds (section 3.13 and Figure 18). On the regionally flat (but locally hummocky) deflated lava pond surface, regolith development is highly modified by the presence of significant volumes of shallow void space. As superposed impacts break up the meter-thick, draped, very vesicular lava lake crust surface and cause seismic shaking effects, finer materials preferentially sift and drain into the subsurface voids (Figure S22b). The ever-ongoing infiltration process would largely retard and inhibit the physical development and accumulation of the surface regolith soils, preferentially exposing the blockier substrate, consistent with the observed very thin, or near-absent regolith layer on the floor terrain (section 3.13), and block distributions (section 3.9).

The continuous preferential drainage of regolith into void spaces implies that eventually the void space will be filled, and the currently observed difference between the adjacent shield flanks and the hummocky/rocky floor in roughness and optical maturity will disappear. The current state of the hummocky/rocky floor thus provides clues as to the amount of original void space required to explain the difference in block distribution and maturity between the mounds and the floor. The estimated regolith thickness discrepancy between the Ina floor and surrounding mare indicates that, if the seismic sieving model is correct, a net total of 3–4 m of void space below the chilled lava lake crust is required to accommodate the difference in thickness. Assuming that the topographic difference between the wall ledge and the deepest part of the floor (~30 m) represents the minimum depth of the drained lava lake, then (3–4/30=) ~10–13% of this thickness/depth must have been retained as void space to account for the Ina observations. Applying simple beam theory to typical widths of floor units between mounds (~50–200 m) shows that a 1.5-m thick chilled lava crust could support a roof over a lava drainage channel up to ~30-m deep and ~150-m wide. If 20–25% of the floor unit was initially underlain by such drained lava channels, this volume of void space, with the addition of the abundant large macrovesicles and open void spaces formed during the complex lava lake process, would be more than sufficient to account for the *missing regolith*. Furthermore, any smaller drainage channels and pressure ridges, as well as open void space in vesicular lavas and foams (observed to be in the 10–40% range in the upper 10 m at Kīlauea Iki, Richter & Moore, 1966), would further contribute to available void space for particle drainage during regolith formation and seismic sieving.

Block distributions observed in the Ina interior also provide important insights into lava lake subsidence and substructure. Optical maturity data show that the least optically mature regions are collocated with the blockiest areas (Figure 19), and the blockiest areas in Ina correspond to the areas of steepest slopes (Figures 5b and 6c), consisting of the (1) scarps at the edge of the Ina interior, (2) boulder fields making up about 6% of the interior floor unit, and (3) moats frequently surrounding the mounds. The scarps, steep slopes, and blocks at the base of the Ina interior wall are readily explained by the lava lake margins chilling against the pit crater wall and then the chilled edge being exposed by the downward and inward movement of the lava lake crust during drainage. The preferred occurrence of blocks within the moats is consistent with the enhanced regolith drainage due to the steep slopes of the mound margins (Figure 6c) and excess void space (cracks) formed by magmatic foam extrusion. The hummocky and pitted floor units within Ina's interior (section 3.5 and Figure 13) are interpreted to represent different degrees of drainage during regolith development: the hummocky terrain represents relatively thicker regolith, where drainage is slowing, net accumulation of soil is occurring, and superposed craters are starting to be retained. The pitted terrain is interpreted to be thinner regolith, with efficient drainage producing the pitted texture, and crater retention being relatively less efficient. The boulder fields are interpreted to represent the regions with the most efficient and long-lasting regolith drainage, and thus to be underlain by areas of most significant void space. The distribution of boulder fields in the floor unit, consisting of multiple annuli preferentially around the center of Ina, and the central parts of the intermound floor unit (Figure 5b), supports this interpretation. In terrestrial pit crater lava lakes (e.g., the Alea lava lake during the August 1963 eruption; Peck & Kinoshita, 1976), cooling is more efficient in the shallower marginal parts of the lake and less efficient over the deeper part above the source vent; upon multistage, intermittent drainage toward the central part of the lake above the vent, a network of subchilled crust lava tubes are very likely to be developed preferentially in a circumferential pattern on the crust. Maximum void space in these annuli would then lead to preferential drainage and maximum block exposure, as we observe (Figure 5b). Taken together, lateral variations in the

distribution of void space could readily account for the observed complicated and variable surface textures on the Ina floor unit.

4.2.4. Landscape Evolution

Landscape evolution is the postemplacement, sequential modification of the initial landscape over geologic time driven by a wide range of exogenic and endogenic processes. As landforms are bounded by slopes, their evolution is best understood through the study of slope character and development, and the related controlling factors. On the Moon, during at least postmare periods, impact cratering is the dominant process responsible for altering the surface topography. Conventional lunar crater production functions (e.g., the one proposed by Neukum et al., 2001) suggest a steep cumulative SFD for craters smaller than a few kilometers. Under this impact crater flux, the very frequent formation of small craters will smooth the topography at longer length baselines in a *sand-blasting* fashion and topographically mute them over time (Soderblom, 1970). This progressive degradation through impact cratering can be treated as a continuum problem, and the net effect is diffusional (Fassett & Thomson, 2014). This typical diffusive landscape evolution model applies to standard regolith development on mare basalt materials. Together, these cumulative events operate to create a thick regolith and to cause diffusive degradation of crisp and sharp landforms and boundaries typical of initially formed pristine lava flows (Wilson & Head, 2017b, Figure S22a), as observed at ancient mare regions surrounding Ina (Figure 3).

On the basis of the very high likelihood that the initial Ina mounds and lower unit floor topography date from the last stages of shield volcano pit crater resurfacing more than 3 Ga ago, we infer that these late-stage pit crater evolution processes and the unique products can also account for the crisp appearance of the Ina interior geomorphology. In the case of Ina, floor units with extreme macroporosity, where seismic sifting and vertical regolith infiltration are the dominant factors, will not be characterized by the typical type of topographic diffusive process (Figure S22b); neither will the hypothesized magmatic foam mounds, where superposed craters tend not to spread ejecta laterally away from the mounds, and any ejecta that might be spread laterally tends to be lost to regolith infiltration (Figure S22c). Together, these unusual surface modification processes will change landscape evolution from typical diffusive process dominated (Fassett & Thomson, 2014) to one of predominantly vertical regolith infiltration, serving to maintain the visual crispness and steep slopes of the terrain, and its sharp boundaries with the mounds and the more typical surroundings cause the observed boulder exposure and perpetuation of the surface roughness and optical immaturity. Fassett and Thomson (2015) report maximum ages for Ina scarps and moats, based on their diffusional model, of 5–40 Ma, supporting our model of the ongoing seismic sifting and regolith infiltration. The presence of abundant 1- to 5-m blocks (Figures 5b and 5c) and the localized steep slopes (Figures 6c and S19) at the bases of moats both indicate that local regolith infiltration is most efficient there, and downward moat development and boulder exposure are ongoing processes, consistent with the extremely young diffusional model age (<1–2 Ma, Fassett & Thomson, 2015).

4.3. Crater Populations and Retention Ages

Focusing on the Ina hummocky/blocky floor materials, Schultz et al. (2006) interpreted their rough texture and optical immaturity to be due to removal of fine materials by outgassing of juvenile volatiles occurring within the past 10 Ma, while Braden et al. (2014) interpreted the Ina mounds to be formed by extrusive volcanism that occurred about 33 Ma ago on the basis of their superposed impact crater SFD. Our new crater population study also yields <100-Ma model ages for the Ina mounds and floor terrains (section 3.11). If the Ina shield volcano indeed formed ~3.5 Ga ago (Figure S1b), and the observed morphological crispness of Ina interior is consistent with the waning-stage evolution of lava lake processes within the summit pit crater, could the small area or the unusual physical properties of the mounds and floor also account for these observed anomalously young crater retention ages? Our previous work has provided a preliminary analysis of impact into the magmatic foam mounds and the resultant crater retention age (Qiao et al., 2017). We here present an updated and more detailed investigation of impact cratering in Ina mounds and a new analysis of impact cratering in Ina floor hummocky units.

To begin with, we focused on the Ina mounds, which are dated younger than 100 Ma via superposed impact crater populations (Braden et al., 2014 and section 3.11). In order to investigate the crater SFD and its discrepancy from the 3.5 Ga-old hosting shield volcano, we first recounted all impact craters larger than 10 m in diameter superposed on the Ina mounds using LROC NAC images with a wide range of illumination

geometries and found more than twice as many craters as reported by Braden et al. (2014), yielding a model age of 59 Ma (Figure 16c and Table 1); this indicates that craters formed on the Ina mounds are poorly preserved and easily degraded beyond recognition, consistent with our proposed cratering mechanism on the solid magmatic foams (section 4.2.1). Second, we investigated the distribution of superposed craters as a function of topographic slope on the mounds and found that there are many fewer small craters where slopes exceed 6° than on the flatter part of the mounds, leading us to conclude that the convex shape of the mounds could lead to the loss of superposed craters as a function of time. Third, we asked the question: Could the small total area and irregular shapes of the mounds contribute to an artificially younger crater retention age? We transferred a map of Ina interior to the upper flank of the shield volcano where we obtained the ~3.5 Ga age for the shield (Figure 16b) and found it has a relatively lower cumulative crater density at larger sizes than the much more extensive crater counting area on the shield (cf. Figures S1b and 16c). This exercise suggests that the counting area may be too small and that if a larger counting area is used, a greater number of larger craters would be detected, potentially resulting in an older model age, as suggested by previous works (e.g., van der Bogert et al., 2015).

Fourth, we addressed the question of whether the solid magmatic foam substrate could be responsible for altering the superposed impact crater SFD compared with what would be expected in normal basalt lava flows (as observed on the Ina shield volcano flanks; ~3.5 Ga). Target porosity, along with other substrate properties, has long been revealed to have significant effects on the impact process and final crater dimensions, particularly for smaller craters formed in the strength-dominated regime. On the Moon, the strength-controlled scaling applies to craters with diameters smaller than ~300–400 m (Melosh, 1989; Schultz & Spencer, 1979), so almost all craters superposed on both Ina mounds (Figure 16a) and the surrounding shield flank count area (Figures 16 and S1) are formed in the strength-scaling regime. The extreme microvesicular nature of the Ina mounds will introduce a distinct impact cratering mechanism characterized by more energy dissipation, permanent crushing and compaction of the target material, smaller crater diameters, and a minimum amount of ejected materials (section 4.2.1 and references therein; Figure S22c). Wünnemann et al. (2011) employed a porosity compaction model and conducted a suite of hundreds of numerical modeling experiments of impacts into targets of variable porosity (up to 35%) and found a negative linear relationship between target porosity and one of the crater scaling parameters when keeping other conditions constant; for instance, for a constant substrate friction coefficient of 0.8, dimensionless crater diameters formed within a 25%-porosity target are reduced by ~20% compared with those within a consolidated (zero porosity) target. Prieur et al. (2017) ran numerous numerical calculations and parameterized the effect of porosity on crater scaling coefficients, which suggests a change in porosity from 10% to 50% would result in a decrease of ~20–25% in crater diameter. Laboratory impact cratering experiments into various targets of a wider porosity (φ) range, including basaltic rocks ($\varphi \approx 0$), dry sandstone ($\varphi = \sim 23\%$), and sintered glass beads ($\varphi = \sim 5\%–84\%$), demonstrate that porosity, when observed as an isolated parameter, exponentially reduces crater volumes (V_N, Michikami et al., 2007; Moore et al., 1963; Poelchau et al., 2013). Mathematical fitting to all these experimental data parameterizes crater volume as a function of target porosity: $V_N = (1.10 \pm 0.10)\, e^{(-0.077 \pm 0.004)\varphi}$, where φ is given as a percentage. Given the hypothesized magmatic foam nature of Ina mounds and the popping of the surface layer during its extrusion process, a bulk porosity of ~75% can be conservatively assumed (Qiao et al., 2017). The porosity of the uppermost meters of typical mare regions (in which most regolith-building craters formed) is incompletely understood, though it can reasonably be assumed to be between ~12% (gravitational calculations for the lunar crust, Wieczorek et al., 2013) and ~30% (measurements of returned core samples, Carrier et al., 1991). Substituting these substrate porosity values into the empirical function implies that the volume of craters formed in the Ina mounds will be reduced by a factor of between ~30 and ~125 compared with those in the typical lunar mare regolith targets, which corresponds to a factor of ~3–5 decrease in crater diameter (specifically, a reduction to 19.8–31.5% of the original diameter value). This laboratory experiment-based estimation of the crater diameter diminishing effect is generally consistent with pi-group scaling calculations, which show that impacts into more porous targets tend to produce smaller craters than into less porous targets, and target property contrasts between porous mare rock and nonporous rock can lead to an up to ~250% difference in final crater diameters (van der Bogert et al., 2017). Target property variations have also been observed to result in an impact crater density difference of up to ~600–700% between comparably aged surface terrains on Mars (Dundas et al., 2010), more than sufficient

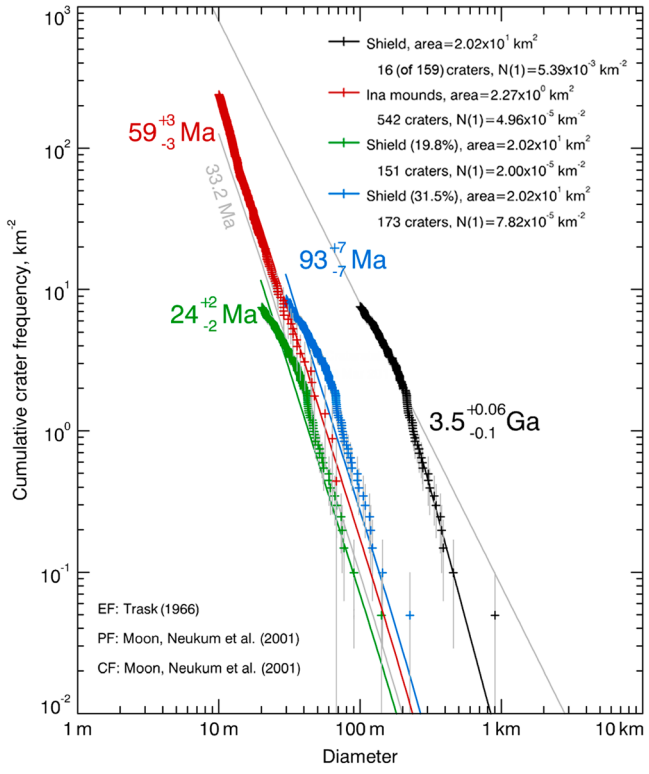


Figure 22. Investigation of the response of solid magmatic foam substrate to the formation and retention of superposed craters, and the estimated crater counting model ages. The cumulative SFD of craters identified on the shield flank (Figure S1) and Ina mounds (Figure 16) is replotted here as black and red crosses, respectively. All the counted shield craters are resized with their diameters reduced by factors of ~3 and ~5 (specifically, 19.8% and 31.5% of the original values) and cumulatively plotted as green and blue crosses, separately. The gray line on the right is the lunar equilibrium curve from Trask (1966), and the left gray line is the isochron for the 33.2 Ma age obtained by Braden et al. (2014). The model age fitting is based on the Neukum lunar PF and CF, using the CraterStats software package (Michael et al., 2016; Michael & Neukum, 2010).

to explain the crater density disparity between the Ina interior mounds and the exterior shield flanks (section 3.11).

Finally, this considerable crater scaling effect of the highly porous nature of Ina mounds provides an important insight in interpreting its anomalously young crater retention ages and their discrepancy from the surrounding shield flanks. We resized all the superposed impact craters identified in the count area on the Ina shield volcano (Figure S1a) with diameter reductions by factors of 3 and 5 as found above. The cumulative SFDs of the two diameter-scaled crater populations then plot very close to that of the Ina mounds, and, of particular interest, the SFD plot of the Ina mound craters lies between that of the two scaled crater populations (Figure 22). Fitting of the scaled craters using Neukum functions (Neukum et al., 2001) yields model ages of 24 and 93 Ma, respectively; both are younger than ~100 Ma. Most importantly, the crater retention age of Ina mounds either previously obtained by Braden et al. (2014; 33 Ma) or updated by our renewed crater counts (59 Ma; section 3.11) lies between the ages derived from the two scaled shield crater populations.

We now turn our focus to the impact populations on the Ina hummocky floor terrain. Characterized by an unusual substrate nature of multiple large void spaces (macrovesicularity) and abundant microvesicularity, impacts into the Ina floor terrain are predicted to be dominated by continued vertical infiltration and seismic sieving of the surface regolith and impact breccia, resulting in craters being poorly developed, difficult to identify, and degrading very rapidly (section 4.2.1 and Figure S22b). Large impacts will tend to not form ejecta but instead crush the targets and leave very shallow craters filled with crushed rubble; these are not very obvious to start with and degrade rapidly, producing a deficit of larger craters. This unusual impact cratering behavior (decrease in diameter) and rapid loss of superposed craters will inhibit intensely the construction of a crater record typical of normal lunar terrains elsewhere and its preservation on the lunar surface and push the impact crater SFD to extreme younger ages. The observed elevated optically immaturity of the floor terrains suggests that this crater *loss* process probably operates more intensely on the floor units than on the Ina mounds, consistent with the estimated comparable or younger crater retentions ages of the Ina floor units (Figure 16c).

Based on the suite of analyses above, we conclude that the unusually low impact crater density on the Ina mounds and floor terrains and the resultant anomalously young crater retention ages can be well understood in terms of the role of the unique substrate characteristics (chilled lava lake crust floor and solid magmatic foam extrusions) in the formation and retention of superposed impact craters, along with other factors including the relatively smaller crater count area, and the rapid loss of craters due to the slope effect and continuous regolith infiltration process. Nevertheless, we should note that the detailed impact cratering mechanism in highly porous targets (e.g., Ina foamy mounds) and the resultant effects on crater retention age are currently not completely understood. Additional future laboratory and numerical investigations would further contribute to our understanding of these processes.

4.4. Implications for the Origin of Other IMPs and Duration of Mare Volcanism

Our comprehensive geological characterization and observation-based analysis convincingly supports the two-component scenario of waning-stage lava lake processes and magmatic foam extrusion for the formation of the Ina interior (Qiao et al., 2017; Wilson & Head, 2017b). These processes produce volcanic deposits with very unusual physical properties, thus exerting an influence on the nature of regolith development, and crater formation and retention processes, resulting in anomalously young interpreted ages for the Ina summit pit crater floor that more plausibly formed contemporaneously with the underlying shield

volcano about 3.5 Ga ago. The two other lunar IMP occurrences dated as younger than 100 Ma by Braden et al. (2014, i.e., Sosigenes, ~18 Ma and Cauchy 5, ~58 Ma; Figure S24) also lie at the top of dikes (Qiao et al., 2018; Qiao, Head, Xiao, Wilson, & Dufek, 2018) and hence could be reinterpreted to be emplaced in a similar manner billions of years ago. Our interpreted ancient formation ages, in contrast to the geologically very recent lava extrusion hypothesis (Braden et al., 2014), also coincide with the climax of global volcanism between circa 3.3–3.8 Ga ago (e.g., Pasckert et al., 2018 and references therein). The current lunar thermal regime and magmatic evolution models suggest that the Moon, as a one-plate planetary body, progressively lost its primordial and internally generated heat effectively by conduction, leading to volcanism having waned in middle lunar history and ceased sometime in the last ~1 Ga (e.g., Head & Wilson, 1992, 2017; Hiesinger et al., 2011; Morota et al., 2011; Solomon & Head, 1980). Our new model of contemporaneous late-stage shield-building volcanism ~3.5 Ga ago thus makes a major reevaluation of the conventional theory unnecessary. Our progressive observational and numerical investigations of Ina (Qiao et al., 2017, 2016; Qiao, Head, Wilson, & Ling, 2018; Qiao, Head, Xiao, Wilson, & Dufek, 2018; Wilson & Head, 2017b, 2018) make it a prime target candidate for future landers, rovers, and sample return missions, which show enormous potential for strengthening our knowledge of the magmatism and thermal evolution of the Moon and other terrestrial bodies (e.g., Draper et al., 2018; Qiao et al., 2018; Wagner et al., 2018).

5. Conclusions

On the basis of the comprehensive geological characterization and analysis of the origin of the Ina pit crater presented above, we draw the following conclusions:

1. *Location, Context, and Age*. Ina is located in the middle of Lacus Felicitatis, a small Imbrian-aged mare occurrence on the lunar nearside. The Lacus Felicitatis basalts are superposed on the areally extensive ejecta deposits from the Imbrium and Serenitatis basins emplaced circa 3.85 Ga ago and on the extensive and topographically prominent linear ejecta scour radial to the two basins. The mare basalts emplaced within central Lacus Felicitatis (within which Ina is located) exhibit apparent compositional changes as a function of time, with underlying (relatively old) basalts more titanium rich than the surface (most recently emplaced) basalts. The central part of Lacus Felicitatis lies on a plateau up to ~800 m above the adjacent maria on topography most likely related to the radial Imbrium ejecta sculpture.
2. *Superposition of Ina on an Ancient Shield Volcano*. Locally, Ina occurs as a ~2 × 3-km summit pit crater atop a broad dome ~22-km wide at its base, ~320-m high and ~0.6 km^3 in volume, which is interpreted as a small shield volcano built up through accumulating low-effusion rate, cooling-limited flows during eruptions from a single dike source ~3.5 Ga ago. The Ina shield volcano is at the upper end of the height and diameter range of over 300 small mare shields identified on the Moon, consistent with its formation by relatively longer flows (up to ~12 km) through lengthy eruptions (estimated at ~3–6 months). Theories of the origin of the Ina structure and its unusual features must account for the fact that Ina is the summit pit crater on an ancient ~3.5-Ga shield volcano built on associated mare deposits.
3. *Similarity of Ina Summit Pit Crater to Those on Hawai'i*. The Ina summit pit crater interior is defined by an inward facing wall and a relatively flat basal terrace/ledge with a steep inward facing scarp up to ~12-m high, and the pit crater is externally bordered by a low raised *collar* structure. On the basis of our documentation and the similarities to small Hawaiian volcano pit craters, we interpret Ina's external narrow collar to be the remnant of lava lake filling and overflow, together with deposited pyroclastic debris, and the interior basal terrace and steep inward-facing scarp to be the chilled margin of a lava lake remaining after lava lake cooling and/or recession, embayed by subsequent magmatic foam extrusions near the floor edge.
4. *Major Ina Interior Units*. The Ina interior is made up of three major morphologic units also typical of other major lunar IMPs: (a) topographically higher, bulbous-shaped mound units (50% by area) surrounded by (b) topographically lower, hummocky units (44%) with ridged and pitted textures, and (c) topographically lower, blocky units (6%) consisting of 1- to 5-m size boulders.
5. *Theoretical Assessment of the Ascent and Eruption of Magma in Late-Stage Summit Pit Craters on the Moon*. On the basis of (a) our latest theoretical treatment of late-stage shield-building magmatic activity and volatile exsolution physics, (b) documentation of magmatic-volcanic processes from terrestrial small shield volcano summit pit craters in Hawai'i, and (c) comprehensive geological characterization of the context and interior of Ina pit crater, we interpret the wide range of characteristics associated

with the Ina feature to be consistent with a two-component model of origin during the waning stages of shield volcano summit pit crater eruption activities characterized by the extrusion and solidification of magmatic foams (mound foam model) on a subsided lava lake crust (hummocky floor model), occurring ~3.5 Ga ago, contemporaneous with the underlying shield volcano and the major global phase of lunar mare volcanism.

6. *Nature and Origin of the Ina Summit Pit Crater Interior Mounds*. Over 80 individual mounds are arrayed across the interior of Ina and a few form coalescing patterns. The tops of Ina mounds are typically ~20–50 m below the pit crater rim crest, and rise up to ~20 m above the adjacent floor terrains. Topographic moats, several meters wide and up to ~1-m deep, are often observed at the mound margins. The summit elevation of mounds decreases toward the center of Ina, and the majority of mounds show area-averaged slopes toward the pit crater center. Several bleb-like mounds are observed to be located in small topographic depressions in a manner similar to *ring-moat dome structures* recently documented elsewhere in the lunar maria. The bleb-like mounds are interpreted to be magmatic foam extruded through cracks in the solidified lava lake crust. Extrusion of the foam causes subsidence and flexure of the lava lake crust in the immediate vicinity of the foam, enhancing the meniscus-like borders of the mounds, the scarp-like contacts with the floor terrains, and the creation of moats at the margins. The popping of the outermost layer of extruded foam gas bubbles will produce a surface layer with smaller particle sizes than typical mature regolith. Rheological modeling shows that magmatic foam extrusion is likely to proceed at a very low effusion rate (<1 m^3/s), and that the majority of the Ina mounds are predicted to be emplaced over a period of several hours to several days (Wilson & Head, 2017b).
7. *Nature and Origin of the Ina Summit Pit Crater Floor Unit*. The Ina summit pit crater interior floor, including both hummocky and blocky units, mainly lies about 20–50 m below the pit crater rim, and is generally flat, while sloping gently (<2°) toward the center (Figure 7). The pit crater floor can be categorized as three annular terraces, with ~10-m elevation decrements toward the interior. The interior mounds appear to preferentially present at the contacts between the annular terraces, suggesting an association between lava lake subsidence, lava lake crust flexure and cracking, and the extrusion of the foam mounds. The floor hummocky/blocky units are characterized by a wide range of very complex morphologies. We interpret the floor terrains as solidified lava lake crust, and each of their complex topographic and morphologic characteristics corresponds to the various processes operating during the lava lake formation, evolution, and solidification process: (1) the three-stage annular, inwardly lower floor topography is interpreted to be formed through lava lake inflation, drainage, and ultimate solidification; (2) the hummocky textures could be analogous to lava lake inflation, lava lake crust flexure, bending, fracturing, and ridge formation, with hornitos and other features partly buried by subsequent flows; (3) the abundant pits are interpreted to be due to regolith infiltration and sifting into the porous and macrovesicular lava lake crust and void space below; (4) the linear depressions/fractures are interpreted to be modified cracks in the lava lake surface formed by flexure, cooling, and shrinkage during lava lake deflation and deformation; (5) the polygonal patterns are analogous to highly deformed and cracked lava lake crust; (6) the vermicular patterns are analogous to tilted lava lake crust plates; (7) the ridged textures are interpreted to be locally deformed lava surface crust; (8) the floor blocky units are analogous to blocks of the solidified lava lake crust exposed by impact and drainage of regolith fines into the subsurface; and (9) the preferential occurrences of mounds at the contacts between floor annular terraces are interpreted to be due to the extrusion of magmatic foam through the lava lake crust fractures caused by its inward subsidence.
8. *Effects of Unusual Summit Pit Crater Floor Features on Their Subsequent Evolution*. The unusual physical characteristics of the Ina interior, solidified magmatic foam mounds with bulk porosity up to ~95% and chilled lava lake crust floor with abundant microvesicularity and large void spaces, introduce remarkable differences in the processes that characterize postemplacement geological modification of lunar features, including impact cratering, optical maturation, regolith development, and topographic degradation.
9. *Characteristics of Impact Cratering in the Lunar Summit Pit Crater Floor Environment*. On the Ina floor terrains, due to the highly vesicular nature of the substrate, impact cratering will be dominated by permanent crushing and compaction of the target materials, disruption of vesicle walls, excavation of the blocky portions of the crust substrate, and a negligible amount of lateral ejecta transfer beyond

the crater rim. The resultant craters are predicted to be poorly developed (much deeper penetration relative to lateral crater growth), filled with crushed rubble, abnormally shaped, difficult to identify and to degrade rapidly and to show a deficit of larger craters due to the decreased diameter-depth relationship. The continuous infiltration of the finer components of surface regolith into the significantly macroporous substrate, assisted by subsequent impact-induced seismic shaking and sieving, is predicted to change the typical laterally diffusive topographic degradation into a vertical infiltration-dominated style, serving to largely inhibit the physical development and accumulation of regolith, maintain the morphological crispness and optical immaturity, and expose underlying fresh and unweathered blocks and boulders.

10. *Impact Cratering on the Summit Pit Crater Floor Foam Mounds*. On the Ina floor mounds, interpreted to be formed by extrusion of magmatic foam, subsequent impact cratering will operate in a style dominated by permanent compressing, crushing, shattering, and penetrating of the foam vesicles (the aerogel effect), and rapid decay of impact-induced shock waves, leading to a significant reduction of cratering efficiency. Under these circumstances, the mound craters tend to be much smaller in diameter and deeper, nonblocky, poorly preserved, and easily degraded than those formed by a similar impact into typical solid basalt or regolith. The effective absorption of impact-induced shock waves decreases the production of reduced submicroscopic metallic iron particles, retarding the typical optical maturing of the mound materials. Regolith development on Ina mounds is inhibited due to the predominantly nonblocky impact craters, much lower amount of lateral ejecta, and the preferential downslope movement of surface regolith toward the steeper mound margins. Landscape evolution on the mounds will also operate in a vertical compressing and crushing style, rather than a lateral ejecta dispersal dominated style, thus helping to maintain sharp mound boundaries with the floor terrains.
11. *Effect of the High-Porosity Substrate Characteristics on the Retention Ages of Superposed Impact Craters*. The impact craters superposed on both mounds and floor terrains of the Ina summit pit crater interior exhibit a range of morphological peculiarities, significantly different from their counterparts on typical mare regolith regions. The Ina floor has an areal density of superposed impact craters comparable to, or slightly lower than, the Ina mounds, and both Ina interior units yield crater retention ages less than 100 Ma, significantly younger than the ~3.5 Ga old age estimated for the adjacent and underlying shield volcano flanks. The apparent discrepancy in impact crater populations and the resultant crater retention ages can be understood in the context of the role of the unique substrate characteristics (chilled lava lake crust floor and solidified magmatic foam extrusions) in the formation and retention of superposed impact craters. Accounting for the effects of the reduced size of craters (smaller by factors of ~3–5) formed in the highly porous magmatic foam mounds results in a shift of the crater SFD model ages from <100 Ma to ~3.5 Ga, contemporaneous with the age of the underlying ancient shield volcano and the major global phase of lunar mare volcanism. We conclude that extremely young mare basalt eruptions to account for the Ina summit pit crater floor formation are not required, and that the presented scenario is in accord with lunar thermal evolution models.
12. *Implications for Future Exploration*. Future robotic and human exploration of Ina and related IMP deposits could resolve many of the outstanding questions remaining about these enigmatic features. Sample return missions could provide radiometric dates for the Ina deposits, readily distinguishing between a 3.5 Ga and a < 0.1 Ga crystallization age, as well as determining the physical properties of the mounds and hummocky materials. Seismometers and other geophysical instruments could test hypotheses for the density structure of the lava lake floor and underlying solidified lava lake. Penetrometer missions could also assist in the analysis of physical properties of the substrate materials. Such future missions could help resolve the several hypotheses for the enigmatic Ina feature and contribute critical information on the total duration of mare basalt volcanism and the thermal evolution of the Moon.

Acknowledgments
This study is a multilateral effort involving scientists from the United States, the United Kingdom, and China. This study is supported by the Key Research Program of the Chinese Academy of Sciences (grant XDPB11), the National Natural Science Foundation of China (41703063 and 41373066), the China Postdoctoral Science Foundation (2017M610421 and 2018T110682), and Open Fund of State Key Laboratory of Information Engineering in Surveying, Mapping and Remote Sensing, Wuhan University (grant 18P03). L. Q. was partially supported by the State Scholarship Fund from Chinese Scholarship Council as a visiting student at Brown University (201406410040). L. W. thanks the Leverhulme Trust for support via an Emeritus Fellowship. We gratefully acknowledge financial support from the NASA Solar System Exploration Research Virtual Institute (SSERVI) grant for Evolution and Environment of Exploration Destinations under cooperative agreement NNA14AB01A at Brown University. This work was partly funded as part of J. W. H.'s membership on the Lunar Reconnaissance Orbiter Lunar Orbiter Laser Altimeter (LOLA) team, under NASA grant NNX09AM54G. We gratefully acknowledge W. Brent Garry, an anonymous reviewer, and the Editor David Baratoux for their helpful comments. All original LRO data can be found in the NASA's Planetary Data System (http://pds.nasa.gov/) and all original Kaguya/SELENE data are archived at SELENE Data Archive (https://darts.isas.jaxa.jp/planet/pdap/selene/).

References

Bandfield, J. L., Ghent, R. R., Vasavada, A. R., Paige, D. A., Lawrence, S. J., & Robinson, M. S. (2011). Lunar surface rock abundance and regolith fines temperatures derived from LRO Diviner Radiometer data. *Journal of Geophysical Research*, *116*, E00H02. https://doi.org/10.1029/2011JE003866

Barker, M. K., Mazarico, E., Neumann, G. A., Zuber, M. T., Haruyama, J., & Smith, D. E. (2016). A new lunar digital elevation model from the Lunar Orbiter Laser Altimeter and SELENE Terrain Camera. *Icarus*, *273*, 346–355. https://doi.org/10.1016/j.icarus.2015.07.039

Bart, G. D. (2014). The quantitative relationship between small impact crater morphology and regolith depth. *Icarus*, *235*, 130–135. https://doi.org/10.1016/j.icarus.2014.03.020

Bart, G. D., Nickerson, R. D., Lawder, M. T., & Melosh, H. J. (2011). Global survey of lunar regolith depths from LROC images. *Icarus*, *215*(2), 485–490. https://doi.org/10.1016/j.icarus.2011.07.017

Basilevsky, A. T., Head, J. W., & Horz, F. (2013). Survival times of meter-sized boulders on the surface of the Moon. *Planetary and Space Science*, *89*, 118–126. https://doi.org/10.1016/j.pss.2013.07.011

Bennett, K. A., Horgan, B. H. N., Bell, J. F., III, Meyer, H. M., & Robinson, M. S. (2015). Moon Mineralogy Mapper investigation of the Ina irregular mare patch. 46th Lunar and Planetary Science Conference, Lunar and Planetary Institute, The Woodlands, Texas, abstract #2646.

Braden, S. E. (2013). *Analysis of spacecraft data for the study of diverse lunar volcanism and regolith maturation rates (Doctoral dissertation). Retrieved from ASU Library*. Tempe, AZ: Arizona State University. http://repository.asu.edu/items/20943

Braden, S. E., Stopar, J. D., Robinson, M. S., Lawrence, S. J., van der Bogert, C. H., & Hiesinger, H. (2014). Evidence for basaltic volcanism on the Moon within the past 100 million years. *Nature Geoscience*, *7*(11), 787–791. https://doi.org/10.1038/ngeo2252

Carrier, W. S., Olhoeft, G. R., & Mendell, W. (1991). Physical properties of the lunar surface. In G. H. Heiken, D. T. Vaniman, & B. M. French (Eds.), *Lunar sourcebook*, (pp. 475–594). Cambridge: Cambridge University Press.

Carter, L. M., Hawke, B. R., Garry, W. B., Campbell, B. A., Giguere, T. A., & Bussey, D. B. J. (2013). Radar observations of lunar hollow terrain. 44th Lunar and Planetary Science Conference, Lunar and Planetary Institute, The Woodlands, Texas, abstract #2146.

Clark, B. E., Hapke, B., Pieters, C., & Britt, D. (2002). Asteroid space weathering and regolith evolution. In W. F. Bottke, A. Cellino, P. Paolicchi, & R. P. Binzel (Eds.), *Asteroids III*, (pp. 585–599). Tuscon, AZ: University of Arizona Press.

Collins, G. S., Melosh, H. J., & Wünnemann, K. (2011). Improvements to the ε-α porous compaction model for simulating impacts into high-porosity solar system objects. *International Journal of Impact Engineering*, *38*(6), 434–439. https://doi.org/10.1016/j.ijimpeng.2010.10.013

Crater Analysis Techniques Working Group (1979). Standard techniques for presentation and analysis of crater size-frequency data. *Icarus*, *37*(2), 467–474. https://doi.org/10.1016/0019-1035(79)90009-5

Daubar, I. J., Atwood-Stone, C., Byrne, S., McEwen, A. S., & Russell, P. S. (2014). The morphology of small fresh craters on Mars and the Moon. *Journal of Geophysical Research: Planets*, *119*, 2620–2639. https://doi.org/10.1002/2014JE004671

Draper, D. S., Stopar, J. D., Lawrence, S. J., Denevi, B., John, K., Graham, L., et al. (2018), The Irregular Mare Patch Exploration Lander (IMPEL) SmallSat mission concept. 49th Lunar and Planetary Science Conference, Lunar and Planetary Institute, The Woodlands, Texas, abstract #1617.

Dundas, C. M., Keszthelyi, L. P., Bray, V. J., & McEwen, A. S. (2010). Role of material properties in the cratering record of young platy-ridged lava on Mars. *Geophysical Research Letters*, *37*, L12203. https://doi.org/10.1029/2010GL042869

Dzurisin, D., Koyanagi, R. Y., & English, T. T. (1984). Magma supply and storage at Kilauea volcano, Hawaii, 1956–1983. *Journal of Volcanology and Geothermal Research*, *21*(3-4), 177–206. https://doi.org/10.1016/0377-0273(84)90022-2

El-Baz, F. (1972). New geological findings in Apollo 15 lunar orbital photography. *Proceedings of 3rd Lunar and Planetary Science*, 39–61.

El-Baz, F. (1973). D-caldera: New photographs of a unique feature. In *Apollo 17 preliminary science report* (NASA SP-330, (pp. 30-13–30-17). Washington, DC: United States government printing office.

Elder, C. M., Hayne, P. O., Bandfield, J. L., Ghent, R. R., Williams, J. P., Donaldson Hanna, K. L., & Paige, D. A. (2017). Young lunar volcanic features: Thermophysical properties and formation. *Icarus*, *290*, 224–237. https://doi.org/10.1016/j.icarus.2017.03.004

Elder, C. M., Hayne, P. O., Ghent, R. R., Bandfield, J. L., Williams, J. P., & Paige, D. A. (2016). Regolith formation on young lunar volcanic features, 47th Lunar and Planetary Science Conference, Lunar and Planetary Institute, The Woodlands, Texas, abstract #2785.

Fassett, C. I., & Thomson, B. J. (2014). Crater degradation on the lunar maria: Topographic diffusion and the rate of erosion on the Moon. *Journal of Geophysical Research: Planets*, *119*, 2255–2271. https://doi.org/10.1002/2014je004698

Fassett, C. I., & Thomson, B. J. (2015). A landscape evolution perspective on how young is young on the lunar surface. 46th Lunar and Planetary Science Conference, Lunar and Planetary Institute, The Woodlands, Texas, abstract #1120.

Flynn, G. J., Durda, D. D., Patmore, E. B., Clayton, A. N., Jack, S. J., Lipman, M. D., & Strait, M. M. (2015). Hypervelocity cratering and disruption of porous pumice targets: Implications for crater production, catastrophic disruption, and momentum transfer on porous asteroids. *Planetary and Space Science*, *107*, 64–76. https://doi.org/10.1016/j.pss.2014.10.007

Garry, W. B., Hawke, B. R., Crites, S., Giguere, T., & Lucey, P. G. (2013). Optical maturity (OMAT) of Ina 'D-Caldera', the Moon. 44th Lunar and Planetary Science Conference, Lunar and Planetary Institute, The Woodlands, Texas, abstract #3058.

Garry, W. B., Robinson, M. S., Zimbelman, J. R., Bleacher, J. E., Hawke, B. R., Crumpler, L. S., et al. (2012). The origin of Ina: Evidence for inflated lava flows on the Moon. *Journal of Geophysical Research*, *117*, E00H31. https://doi.org/10.1029/2011JE003981

Hapke, B. (2001). Space weathering from Mercury to the asteroid belt. *Journal of Geophysical Research*, *106*(E5), 10,039–10,073. https://doi.org/10.1029/2000JE001338

Hardee, H. C. (1980). Solidification in Kilauea Iki lava lake. *Journal of Volcanology and Geothermal Research*, *7*(3–4), 211–223. https://doi.org/10.1016/0377-0273(80)90030-X

Hauri, E. H., Saal, A. E., Rutherford, M. J., & Van Orman, J. A. (2015). Water in the Moon's interior: Truth and consequences. *Earth and Planetary Science Letters*, *409*, 252–264. https://doi.org/10.1016/j.epsl.2014.10.053

Hauri, E. H., Weinreich, T., Saal, A. E., Rutherford, M. C., & Van Orman, J. A. (2011). High pre-eruptive water contents preserved in lunar melt inclusions. *Science*, *333*(6039), 213–215. https://doi.org/10.1126/science.1204626

Head, J., & Gifford, A. (1980). Lunar mare domes: Classification and modes of origin. *The Moon and the Planets*, *22*(2), 235–258. https://doi.org/doi:10.1007/BF00898434

Head, J. W. (1976). Evidence for the sedimentary origin of Imbrium sculpture and lunar basin radial texture. *The Moon*, *15*(3-4), 445–462. https://doi.org/10.1007/BF00562252

Head, J. W. (1979). Serenitatis multi-ringed basin: Regional geology and basin ring interpretation. *The Moon and the Planets*, *21*(4), 439–462. https://doi.org/10.1007/BF00897836

Head, J. W., & Wilson, L. (1992). Lunar mare volcanism: Stratigraphy, eruption conditions, and the evolution of secondary crusts. *Geochimica et Cosmochimica Acta*, *56*(6), 2155–2175. https://doi.org/10.1016/0016-7037(92)90183-J

Head, J. W., & Wilson, L. (2017). Generation, ascent and eruption of magma on the Moon: New insights into source depths, magma supply, intrusions and effusive/explosive eruptions (Part 2: Predicted emplacement processes and observations). *Icarus*, *283*, 176–223. https://doi.org/10.1016/j.icarus.2016.05.031

Hiesinger, H., Head, J. W., Wolf, U., Jaumann, R., & Neukum, G. (2011). Ages and stratigraphy of lunar mare basalts: A synthesis. *Geological Society of America Special Papers*, *477*, 1–51. https://doi.org/10.1130/2011.2477(01)

Hörz, F., Zolensky, M. E., Bernhard, R. P., See, T. H., & Warren, J. L. (2000). Impact features and projectile residues in aerogel exposed on Mir. *Icarus*, *147*(2), 559–579. https://doi.org/10.1006/icar.2000.6450

Housen, K. R., & Holsapple, K. A. (2003). Impact cratering on porous asteroids. *Icarus*, *163*(1), 102–119. https://dx.doi.org/10.1016/S0019-1035(03)00024-1

Housen, K. R., & Holsapple, K. A. (2011). Ejecta from impact craters. *Icarus*, *211*(1), 856–875. https://doi.org/10.1016/j.icarus.2010.09.017

Housen, K. R., Holsapple, K. A., & Voss, M. E. (1999). Compaction as the origin of the unusual craters on the asteroid Mathilde. *Nature*, *402*(6758), 155–157. https://doi.org/10.1038/45985

Lucey, P. G., Blewett, D. T., & Jolliff, B. L. (2000). Lunar iron and titanium abundance algorithms based on final processing of Clementine ultraviolet-visible images. *Journal of Geophysical Research*, *105*(E8), 20,297–20,305. https://doi.org/10.1029/1999JE001117

Mangan, M.T., & Helz, R. T. (1986). The distribution of vesicles and olivine phenocrysts in samples from drill hole KI 79–3, Kilauea Iki lava lake, Hawaii (U. S. Geological Survey Open-File Report, 86–424).

McKay, D. S., Heiken, G., Basu, A., Blanford, G., Simon, S., Reedy, R., et al. (1991). The lunar regolith. In G. H. Heiken, D. T. Vaniman, & B. M. French (Eds.), *Lunar sourcebook*, (pp. 285–356). Cambridge: Cambridge University Press.

Melosh, H. J. (1989). *Impact cratering: A geologic process*. London: Oxford University Press.

Michael, G. G., Kneissl, T., & Neesemann, A. (2016). Planetary surface dating from crater size-frequency distribution measurements: Poisson timing analysis. *Icarus*, *277*, 279–285. https://dx.doi.org/10.1016/j.icarus.2016.05.019

Michael, G. G., & Neukum, G. (2010). Planetary surface dating from crater size-frequency distribution measurements: Partial resurfacing events and statistical age uncertainty. *Earth and Planetary Science Letters*, *294*(3–4), 223–229. https://doi.org/10.1016/j.epsl.2009.12.041

Michikami, T., Moriguchi, K., Hasegawa, S., & Fujiwara, A. (2007). Ejecta velocity distribution for impact cratering experiments on porous and low strength targets. *Planetary and Space Science*, *55*(1–2), 70–88. https://doi.org/10.1016/j.pss.2006.05.002

Moore, H. J., MacCormack, R. W., & Gault, D. E. (1963). Fluid impact craters and hypervelocity-high velocity impact experiments in metals and rocks. Proceedings of 6th Hypervelocity Impact Symposium, pp. 367–400.

Morota, T., Haruyama, J., Ohtake, M., Matsunaga, T., Honda, C., Yokota, Y., et al. (2011). Timing and characteristics of the latest mare eruption on the Moon. *Earth and Planetary Science Letters*, *302*(3–4), 255–266. https://doi.org/10.1016/j.epsl.2010.12.028

Neish, C. D., Hamilton, C. W., Hughes, S. S., Nawotniak, S. K., Garry, W. B., Skok, J. R., et al. (2017). Terrestrial analogues for lunar impact melt flows. *Icarus*, *281*, 73–89. https://doi.org/10.1016/j.icarus.2016.08.008

Neish, C. D., Madden, J., Carter, L. M., Hawke, B. R., Giguere, T., Bray, V. J., et al. (2014). Global distribution of lunar impact melt flows. *Icarus*, *239*, 105–117. https://doi.org/10.1016/j.icarus.2014.05.049

Neukum, G., Ivanov, B. A., & Hartmann, W. K. (2001). Cratering records in the inner solar system in relation to the lunar reference system. *Space Science Reviews*, *96*(1/4), 55–86. https://doi.org/10.1023/A:1011989004263

Oberbeck, V., & Morrison, R. (1974). Laboratory simulation of the herringbone pattern associated with lunar secondary crater chains. *The Moon*, *9*(3–4), 415–455. https://doi.org/10.1007/BF00562581

Oberbeck, V. R., & Quaide, W. L. (1967). Estimated thickness of a fragmental surface layer of Oceanus Procellarum. *Journal of Geophysical Research*, *72*(18), 4697–4704. https://doi.org/10.1029/JZ072i018p04697, https://doi.org/10.1029/JZ072i018p04697

Papike, J. J., Hodges, F. N., Bence, A. E., Cameron, M., & Rhodes, J. M. (1976). Mare basalts: Crystal chemistry, mineralogy, and petrology. *Reviews of Geophysics*, *14*(4), 475–540. https://doi.org/10.1029/RG014i004p00475

Pasckert, J. H., Hiesinger, H., & van der Bogert, C. H. (2018). Lunar farside volcanism in and around the South Pole–Aitken basin. *Icarus*, *299*, 538–562. https://doi.org/10.1016/j.icarus.2017.07.023

Peck, D. L., & Kinoshita, W. T. (1976). *The eruption of August 1963 and the formation of Alae lava lake, Hawaii* (U.S. Geological Survey Professional Paper 935-A, (pp. A1–B33). Washington: United States Government Printing Office.

Pieters, C. M., & Noble, S. K. (2016). Space weathering on airless bodies. *Journal of Geophysical Research: Planets*, *121*, 1865–1884. https://doi.org/10.1002/2016JE005128

Pike, R. J. (1974). Depth/diameter relations of fresh lunar craters: Revision from spacecraft data. *Geophysical Research Letters*, *1*(7), 291–294. https://doi.org/10.1029/GL001i007p00291

Pike, R. J., & Spudis, P. D. (1987). Basin-ring spacing on the Moon, Mercury, and Mars. *Earth, Moon, and Planets*, *39*(2), 129–194. https://doi.org/10.1007/BF00054060

Poelchau, M. H., Kenkmann, T., Thoma, K., Hoerth, T., Dufresne, A., & Schäfer, F. (2013). The MEMIN research unit: Scaling impact cratering experiments in porous sandstones. *Meteoritics & Planetary Science*, *48*(1), 8–22. https://doi.org/10.1111/maps.12016

Prieur, N. C., Rolf, T., Luther, R., Wünnemann, K., Xiao, Z., & Werner, S. C. (2017). The effect of target properties on transient crater scaling for simple craters. *Journal of Geophysical Research: Planets*, *122*, 1704–1726. https://doi.org/10.1002/2017JE005283

Qiao, L., Head, J., Wilson, L., Xiao, L., Kreslavsky, M., & Dufek, J. (2017). Ina pit crater on the Moon: Extrusion of waning-stage lava lake magmatic foam results in extremely young crater retention ages. *Geology*, *45*(5), 455–458. https://doi.org/10.1130/G38594.1

Qiao, L., Head, J. W., Wilson, L., & Ling, Z. (2018). Lunar irregular mare patch (IMP) sub-types: Linking their origin through hybrid relationships displayed at Cauchy 5 small shield volcano. *49th Lunar and Planetary Science Conference*. Lunar and Planetary Institute, The Woodlands, Texas, abstract #1392.

Qiao, L., Head, J. W., Xiao, L. & Wilson, L. (2018). Exploration of lunar irregular mare patches (IMPs): Testing models for their formation. *Lunar Science Targets for Landed Missions*, NASA Ames Research Center, Moffett Field, California, abstract # LLW2018-55.

Qiao, L., Head, J. W., Xiao, L., Wilson, L., & Dufek, J. (2016). Sosigenes lunar irregular mare patch (IMP): Morphology, topography, sub-resolution roughness and implications for origin. 47th Lunar and Planetary Science Conference, Lunar and Planetary Institute, The Woodlands, Texas, abstract #2002.

Qiao, L., Head, J. W., Xiao, L., Wilson, L., & Dufek, J. D. (2018). The role of substrate characteristics in producing anomalously young crater retention ages in volcanic deposits on the Moon: Morphology, topography, sub-resolution roughness and mode of emplacement of the Sosigenes Lunar Irregular Mare Patch (IMP). *Meteoritics & Planetary Science*, *53*(4), 778–812. https://doi.org/10.1111/maps.13003

Ravi, S., Mahanti, P., Meyer, H., & Robinson, M. S. (2016). On the usefulness of optical maturity for relative age classification of fresh craters. *American Geophysical Union Fall Meeting*, San Francisco, California, abstract #P53A-2166.

Richter, D. H., Ault, W. U., Eaton, J. P., & Moore, J. G. (1964). *The 1961 eruption of Kilauea volcano, Hawaii* (U.S. Geological Survey Professional Paper 474-D, (pp. D1–B34). Washington: United States Government Printing Office.

Richter, D. H., & Moore, J. G. (1966). *Petrology of the Kilauea Iki lava lake, Hawaii U.S. Geological Survey Professional Paper 537-B*, (pp. B1–B26). Washington: United States Government Printing Office.

Robinson, M. S., Thomas, P. C., Braden, S. E., Lawrence, S. J., Garry, W. B., & LROC Team. (2010). High resolution imaging of Ina: Morphology, relative ages, formation. *41st Lunar and Planetary Science Conference*, Lunar and Planetary Institute, The Woodlands, Texas, abstract #2592.

Rutherford, M. J., Head, J. W., Saal, A. E., Hauri, E., & Wilson, L. (2017). Model for the origin, ascent, and eruption of lunar picritic magmas. *American Mineralogist*, *102*(10), 2045–2053. https://dx.doi.org/10.2138/am-2017-5994ccbyncnd

Saal, A. E., Hauri, E. H., Cascio, M. L., Van Orman, J. A., Rutherford, M. C., & Cooper, R. F. (2008). Volatile content of lunar volcanic glasses and the presence of water in the Moon's interior. *Nature*, *454*(7201), 192–195. https://doi.org/10.1038/nature07047

Schaber, G. G., Boyce, J. M., & Moore, H. J. (1976). The scarcity of mappable flow lobes on the lunar maria: The unique morphology of the Imbrium flows. Proceedings of 7th Lunar and Planetary Science, 2783–2800.

Schultz, P., & Spudis, P. (1983). Beginning and end of lunar mare volcanism. *Nature*, *302*(5905), 233–236. https://doi.org/10.1038/302233a0

Schultz, P. H., Anderson, J. L. B., & Heineck, J. T. (2002). Impact crater size and evolution: Expectations for Deep Impact. 33rd Lunar and Planetary Science Conference, Lunar and Planetary Institute, League City, Texas, abstract #1875.

Schultz, P. H., & Crawford, D. A. (2016). Origin and implications of non-radial Imbrium Sculpture on the Moon. *Nature*, *535*(7612), 391–394. https://doi.org/10.1038/nature18278

Schultz, P. H., & Spencer J. (1979). Effects of substrate strength on crater statistics: Implications for surface ages and gravity scaling. Tenth Lunar and Planetary Science Conference, Lunar and Planetary Institute, Houston, Texas, Abstract #1380.

Schultz, P. H., Staid, M. I., & Pieters, C. M. (2006). Lunar activity from recent gas release. *Nature*, *444*(7116), 184–186. https://doi.org/10.1038/nature05303

Shoemaker, E. M. (1962). Interpretation of lunar craters. In Z. Kopal (Ed.), *Physics and astronomy of the Moon* (pp. 283–360). New York: Academic Press.

Soderblom, L. A. (1970). A model for small-impact erosion applied to the lunar surface. *Journal of Geophysical Research*, *75*(14), 2655–2661. https://dx.doi.org/10.1029/JB075i014p02655

Solomon, S. C., & Head, J. W. (1980). Lunar mascon basins: Lava filling, tectonics, and evolution of the lithosphere. *Reviews of Geophysics*, *18*(1), 107–141. https://dx.doi.org/10.1029/RG018i001p00107

Spudis, P. D. (1993). *The geology of multi-ring impact basins*. Cambridge: Cambridge University Press. https://doi.org/10.1017/CBO9780511564581

Staid, M., Isaacson, P., Petro, N., Boardman, J., Pieters, C. M., Head, J. W., et al. (2011). The spectral properties of Ina: New observations from the Moon Mineralogy Mapper. 42nd Lunar and Planetary Science Conference, Lunar and Planetary Institute, The Woodlands, Texas, abstract #2499.

Stöffler, D., & Ryder, G. (2001). Stratigraphy and isotope ages of lunar geologic units: Chronological standard for the inner solar system. *Space Science Reviews*, *96*(1/4), 9–54. https://dx.doi.org/10.1023/a:1011937020193

Stooke, P. J. (2012). Lunar meniscus hollows. 43rd Lunar and Planetary Science Conference, Lunar and Planetary Institute, The Woodlands, Texas, abstract #1011.

Strain, P. L., & El-Baz, F. (1980). The geology and morphology of Ina. In *Proceedings of the 11th Lunar Science Conference* (pp. 2437–2446).

Trask, N. J. (1966). Size and spatial distribution of craters estimated from the Ranger photographs. In *Ranger VIII and IX, Part II. Experimenters' analyses and interpretations* (JPL Technical Reports 32-800, (pp. 252–264). Pasadena, CA: Jet Propulsion Lab.

Tye, A. R., & Head, J. W. (2013). Mare Tranquillitatis: Distribution of mare domes, relation to broad mare rise, and evidence of a previously unrecognized basin from LOLA altimetric data. 44th Lunar and Planetary Science Conference, Lunar and Planetary Institute, The Woodlands, Texas, abstract #1319.

van der Bogert, C. H., Hiesinger, H., Dundas, C. M., Krüger, T., McEwen, A. S., Zanetti, M., & Robinson, M. S. (2017). Origin of discrepancies between crater size-frequency distributions of coeval lunar geologic units via target property contrasts. *Icarus*, *298*, 49–63. https://doi.org/10.1016/j.icarus.2016.11.040

van der Bogert, C. H., Michael G., Kneissl T., Hiesinger H., & Pasckert J. H. (2015). Effects of count area size on absolute model ages derived from random crater size-frequency distributions. 46th Lunar and Planetary Science Conference, Lunar and Planetary Institute, The Woodlands, Texas, abstract #1742.

Valantinas, A., Kinch, K. M., & Bridžius, A. (2018). Low crater frequencies and low model ages in lunar maria: Recent endogenic activity or degradation effects? *Meteoritics & Planetary Science*, *53*(4), 826–838. https://doi.org/10.1111/maps.13033

Vaughan, W. M., & Head, J. W. (2012). *Ina: Lunar sublimation terrain? 5th annual NASA lunar science forum*. Moffett Field, California: NASA Lunar Science Institute.

Wagner, R., Denevi, B. W., Stopar, J. D., van der Bogert, C. H. & Robinson, M. S. (2018). The age of Ina and the thermal history of the Moon. Lunar Science Targets for Landed Missions, NASA Ames Research Center, Moffett Field, California, abstract #LLW2018-15.

Whitaker, E. A. (1972). An unusual mare feature. In *Apollo 15 preliminary science report* (NASA SP-289, (pp. 25-84–25-85).

Wieczorek, M. A., Neumann, G. A., Nimmo, F., Kiefer, W. S., Taylor, G. J., Melosh, H. J., et al. (2013). The crust of the Moon as seen by GRAIL. *Science*, *339*(6120), 671–675. https://doi.org/10.1126/science.1231530

Wilson, L., & Head, J. W. (1981). Ascent and eruption of basaltic magma on the Earth and Moon.*Journal of Geophysical Research*, *86*(B4), 2971–3001. https://doi.org/10.1029/JB086iB04p02971

Wilson, L., & Head, J. W. (2003). Lunar Gruithuisen and Mairan domes: Rheology and mode of emplacement. *Journal of Geophysical Research*, *108*(E2), 5012. https://doi.org/10.1029/2002je001909

Wilson, L., & Head, J. W. (2017a). Generation, ascent and eruption of magma on the Moon: New insights into source depths, magma supply, intrusions and effusive/explosive eruptions (Part 1: Theory). *Icarus*, *283*, 146–175. https://doi.org/10.1016/j.icarus.2015.12.039

Wilson, L., & Head, J. W. (2017b). Eruption of magmatic foams on the Moon: Formation in the waning stages of dike emplacement events as an explanation of "irregular mare patches". *Journal of Volcanology and Geothermal Research*, *335*, 113–127. https://doi.org/10.1016/j.jvolgeores.2017.02.009

Wilson, L., & Head, J. W. (2018). Controls on lunar basaltic volcanic eruption structure and morphology: Gas release patterns in sequential eruption phases. *Geophysical Research Letters*, *45*, 5852–5859. https://doi.org/10.1029/2018GL078327

Wright, T. L., Peck, D. L., & Shaw, H. R. (1976). Kilauea lava lakes: Natural laboratories for study of cooling, crystallization and differentiation of basaltic magma. In G. H. Sutton, M. H. Manghnani, R. Moberly, & E U Mcafee (Eds.), *The geophysics of the Pacific Ocean basin and its margin* (pp. 975–390). Washington, DC: American Geophysical Union. https://doi.org/10.1029/GM019p0375

Wünnemann, K., Collins, G. S., & Melosh, H. J. (2006). A strain-based porosity model for use in hydrocode simulations of impacts and implications for transient crater growth in porous targets. *Icarus*, *180*(2), 514–527. https://dx.doi.org/10.1016/j.icarus.2005.10.013

Wünnemann, K., Marchi S., Nowka D., and Michel P. (2012). The effect of target properties on impact crater scaling and the lunar crater chronology. 43rdt Lunar and Planetary Science Conference, Lunar and Planetary Institute, The Woodlands, Texas, abstract #1805.

Wünnemann, K., Nowka, D., Collins, G. S., Elbeshausen, D., & Bierhaus, M. (2011). Scaling of impact crater formation on planetary surfaces—Insights from numerical modeling. In *Proceedings of the 11th hypervelocity impact symposium* (pp. 1–16). Freiburg, Germany: Fraunhofer.

Xiao, Z., & Werner, S. C. (2015). Size-frequency distribution of crater populations in equilibrium on the Moon. *Journal of Geophysical Research: Planets*, *120*, 2277–2292. https://doi.org/10.1002/2015JE004860

Xiao, Z., Zeng, Z., Ding, N., & Molaro, J. (2013). Mass wasting features on the Moon—How active is the lunar surface? *Earth and Planetary Science Letters*, *376*, 1–11. https://doi.org/10.1016/j.epsl.2013.06.015

Zhang, F., Head, J. W., Basilevsky, A. T., Bugiolacchi, R., Komatsu, G., Wilson, L., et al. (2017). Newly discovered ring-moat dome structures in the lunar maria: Possible origins and implications. *Geophysical Research Letters*, *44*, 9216–9224. https://doi.org/10.1002/2017GL074416

References from the supporting information

Anderson, J. A., Sides, S. C., Soltesz, D. L., Sucharski, T. L., & Becker K. J. (2004). Modernization of the integrated software for imagers and spectrometers. 35th Lunar and Planetary Science Conference, Lunar and Planetary Institute, League City, Texas, abstract #2039.

Bowman-Cisneros, E. (2010). LROC EDR/CDR data product software interface specification. Retrieved from http://lroc.sese.asu.edu/data/LRO-L-LROC-2-EDR-V1.0/LROLRC_0001/DOCUMENT/LROCSIS.PDF

Haruyama, J., Hara, S., Hioki, K., Iwasaki, A., Morota, T., Ohtake, M., et al. (2012). Lunar global digital terrain model dataset produced from SELENE (Kaguya) terrain camera stereo observations. 43rd Lunar and Planetary Science Conference, Lunar and Planetary Institute, The Woodlands, Texas, abstract #1200.

Haruyama, J., Matsunaga, T., Ohtake, M., Morota, T., Honda, C., Yokota, Y., et al. (2008). Global lunar-surface mapping experiment using the Lunar Imager/Spectrometer on SELENE. *Earth, Planets and Space*, *60*(4), 243–255. https://doi.org/10.1186/BF03352788

Henriksen, M. R., Manheim, M. R., Burns, K. N., Seymour, P., Speyerer, E. J., Deran, A., et al. (2017). Extracting accurate and precise topography from LROC narrow angle camera stereo observations. *Icarus*, *283*, 122–137. https://doi.org/10.1016/j.icarus.2016.05.012

Kneissl, T., van Gasselt, S., & Neukum, G. (2011). Map-projection-independent crater size-frequency determination in GIS environments—New software tool for ArcGIS. *Planetary and Space Science*, *59*(11–12), 1243–1254. https://doi.org/10.1016/j.pss.2010.03.015

Kreslavsky, M. A., & Head, J. W. (2016). The steepest slopes on the Moon from Lunar Orbiter Laser Altimeter (LOLA) data: Spatial distribution and correlation with geologic features. *Icarus*, *273*, 329–336. https://doi.org/10.1016/j.icarus.2016.02.036

Lemelin, M., Lucey, P. G., Song, E., & Taylor, G. J. (2015). Lunar central peak mineralogy and iron content using the Kaguya Multiband Imager: Reassessment of the compositional structure of the lunar crust. *Journal of Geophysical Research: Planets*, *120*, 869–887. https://doi.org/10.1002/2014JE004778

Lucey, P. G., Blewett, D. T., Taylor, G. J., & Hawke, B. R. (2000). Imaging of lunar surface maturity. *Journal of Geophysical Research*, *105*(E8), 20,377–20,386. https://doi.org/10.1029/1999JE001110

Robinson, M. S., Brylow, S. M., Tschimmel, M., Humm, D., Lawrence, S. J., Thomas, P. C., et al. (2010). Lunar Reconnaissance Orbiter Camera (LROC) instrument overview. *Space Science Reviews*, *150*(1–4), 81–124. https://doi.org/10.1007/s11214-010-9634-2

Smith, D. E., Zuber, M. T., Jackson, G. B., Cavanaugh, J. F., Neumann, G. A., Riris, H., et al. (2010). The Lunar Orbiter Laser Altimeter investigation on the Lunar Reconnaissance Orbiter mission. *Space Science Reviews*, *150*(1-4), 209–241. https://dx.doi.org/10.1007/s11214-009-9512-y